University of Alberta

Control-Oriented Modeling and System Identification for Nonlinear Trajectory Tracking Control of a Small-Scale Unmanned Helicopter

by

Sepehr Pourrezaei Khaligh

A thesis submitted to the Faculty of Graduate Studies and Research in partial fulfillment of the requirements for the degree of

Doctor of Philosophy

Department of Mechanical Engineering

Spring 2014
Edmonton, Alberta

To my supportive and affectionate parents, Fariba and Bahman;
devoted and compassionate wife, Elnaz;
and precious sister, Solmaz.

Abstract

Model-based control design of small-scale helicopters involves considerable challenges due to their nonlinear and underactuated dynamics with strong couplings between the different degrees-of-freedom (DOFs). Most nonlinear model-based multi-input multi-output (MIMO) control approaches require the dynamic model of the system to be affine-in-control and fully actuated. Since the existing formulations for helicopter nonlinear dynamic model do not meet these requirements, these MIMO approaches cannot be applied for control of helicopters and control designs in the literature mostly use the linearized model of the helicopter dynamics around different trim conditions instead of directly using the nonlinear model. The purpose of this thesis is to derive the 6-DOF nonlinear model of the helicopter in an affine-in-control, non-iterative and square input-output formulation to enable many nonlinear control approaches, that require a control-affine and square model such as the sliding mode control (SMC), to be used for control design of small-scale helicopters. A combination of the first-principles approach and system identification is used to derive this model. To complete the nonlinear model of the helicopter required for the control design, the inverse kinematics of the actuating mechanisms of the main and tail rotors are also derived using an approach suitable for the real-time control applications. The parameters of the new control-oriented formulation are identified using a time-domain system identification strategy and the model is validated using flight test data. A robust sliding mode control (SMC) is then designed using the new formulation of the helicopter dynamics and its robustness to parameter uncertainties and wind disturbances is tested in simulations. Next, a hardware-in-the-loop (HIL) testbed is designed to allow for the control implementation and gain tuning as well as testing the robustness of the controller to external disturbances in a controlled environment on the ground. The controller is also tested in real flights.

Acknowledgements

This work would not have been possible without the support of many people. I would like to express my special appreciation and thanks to my supervisor, Dr. Bob Koch, for his constant support and for allowing me to grow as a research scientist. He also provided me with the opportunity to teach an undergraduate course during my Ph.D. and his advice on both research as well as on my teaching skills have been priceless. I would also like to extend my sincere gratitude to my co-supervisor, Dr. Farbod Fahimi, who introduced me to this research and provided me with his precious and supportive comments during the past six years.

Also many thanks to my examining committee members, Dr. Donald Raboud, Dr. Saeed Behzadipour, Dr. Michael Lipsett, Dr. Reinhard Vehring, Dr. Alan Lynch and Dr. Jeff K. Pieper who offered their thorough feedback and valuable guidance and support.

I would specifically like to thank my colleague, Alejandro Martinez, for his hardworking, knowledge and dedication to our common endeavor. I would like to extend my thanks to our pilots, Travis Albert and John Sison, who generously dedicated their time and effort to the accomplishment of flight tests as an indispensable part of this work. I would also like to thank the members of the mechanical engineering machine shop for their help and support during the past six years, especially the specialist technician, Bernie Faulkner, who provided us with his brilliant ideas on preparing the testbeds and on the accomplishment of ground tests.

Many thanks to my friends in the controls and advanced robotics laboratories, Khashayar Ebrahimi, Masoud Mashkournia and Mehdi Saffarian and all of my friends who supported me to strive towards my goal.

Finally, my deepest appreciation to my precious father, Bahman, whose thoughtfulness and support throughout my life has made me who I am; my compassionate and self-sacrificed mother, Fariba, whose endless dedication and encouragement has always given me purpose in life; my dear wife, Elnaz, who endured this long process with me with her constant support and love without whom this work would not have been possible; and my precious sister, Solmaz, who faithfully supported me throughout my life to fulfil my dreams.

Table of Contents

1 Introduction **1**

1.1 Control Design Challenges and Proposed Solutions 1

1.2 Thesis Overview 7

1.3 Thesis Contributions 9

2 Experimental Setup **12**

2.1 Helicopter Airframe, Avionics and Electronic Hardware 12

2.2 Ground Station and Communications 15

2.3 Autopilot Software and Control Implementation 16

2.4 GPS Latency 18

2.5 Summary 20

3 Control-Oriented Helicopter Modeling **21**

3.1 Fuselage Rigid-Body Dynamics 22

3.2 Main Rotor 23

3.3 Tail Rotor 34

3.4 Empennage 37

3.5 Combined Forces and Moments on Helicopter Fuselage 38

3.6 Affine-In-Control Model 39

3.7 Square Affine-In-Control Formulation 43

3.8 Rotational Dynamics Using First-Principles 46

3.8.1 Gyroscopic Effect of Main Rotor 49

3.8.2 Roll and Pitch Moments using First-Principles 51

3.9 Summary 56

4 Kinematic Modeling **57**

4.1 Main Rotor Mechanism 58

4.1.1 Swashplate Mechanism 59

4.1.2 Bell-Hiller Mixer 64

4.1.3 Collective Pitch to Swashplate Displacement 65
4.1.4 Cyclic Pitch to Swashplate Orientations 73
4.2 Tail Rotor Mechanism 79
4.3 Experimental Validation 84
4.4 Summary 87

5 System Identification and Model Validation 89
5.1 Identification using Ground Test Data 91
5.2 Identification using Flight Test Data 96
5.2.1 Roll and Pitch Identification 99
5.2.2 Yaw Identification 102
5.2.3 Heave Identification 103
5.2.4 Longitudinal and Lateral Velocity Identification 104
5.3 Model Validation 105
5.3.1 Roll and Pitch Validation 105
5.3.2 Yaw Validation 106
5.3.3 Heave Validation 107
5.3.4 Lon. and Lat. Velocity Validation 108
5.4 Comparison of the Rotational Dynamic Models 109
5.5 Summary 112

6 Nonlinear Control Design 117
6.1 Control Design 117
6.2 Simulations 120
6.2.1 Figure-8 Trajectory Tracking 121
6.2.2 Wind Disturbance Rejection 126
6.3 Summary 131

7 HIL Testbed Design 133
7.1 Introduction 134
7.2 HIL Simulation 137
7.3 Testbed Modeling 141
7.3.1 Tuning the Control Gains 144
7.4 Summary 145

8 Experimental Results 148
8.1 HIL Test Results 148

8.1.1 HIL Longitudinal Control Experiment 149
8.1.2 HIL Lateral Control Experiment 154
8.1.3 HIL Heading Control Experiment 157
8.2 Flight Test Results 159
8.2.1 Heading-Hold Control 159
8.2.2 Hover Control 161
8.3 Summary 163

9 Conclusions & Future Work **168**
9.1 Conclusions 168
9.2 Future Work 172

Bibliography **172**

A Kalman Observer for GPS Latency **184**

List of Tables

4.1 Parameters of the Bell-Hiller mixer. 67
4.2 Parameters of the Bell-Hiller mixer's linear approximation. 77
4.3 Parameters of the tail mechanism's linear approximation. 84

5.1 Identified parameters of the Evolution-EX helicopter. 110

6.1 Control gains obtained from the simulations. 122

8.1 Control gains obtained from the HIL experiments. 149

List of Figures

1.1 Schematic of the thesis organization. 10

2.1 Evolution-EX helicopter with Avionics. 13
2.2 Avionics of the helicopter. 14
2.3 Microbotics Servo Switch Card (SSC) module. 14
2.4 Ground station. 16
2.5 Ground station interface. 17
2.6 GUI for the online updating of the Control Gain. 17
2.7 Implementation diagram of the autopilot software. 19

3.1 Schematic of the helicopter with the control point CP. 24
3.2 Longitudinal and lateral flapping schematics of the main rotor. . . 25
3.3 Rotor disk and blade strip schematic viewed from above. 27
3.4 Blade section flow conditions in a general flight. 29
3.5 Induced velocity profile in the axial flight. 31
3.6 Gyroscopic effect on the attitude response to a 15 Nm roll disturbance moment ($\Omega = 1100$ rpm). 50
3.7 Gyroscopic effect on the attitude response to a 15 Nm pitch disturbance moment ($\Omega = 1100$ rpm). 51

4.1 Helicopter Swashplate mechanism. 60
4.2 Helicopter Bell-Hiller Mixer mechanism. 66
4.3 Fero arm machine used to measure the dimensions of the actuating mechanisms. 78
4.4 Helicopter tail mechanism. 80
4.5 The measurement setup for the tail rotor mechanism. 85
4.6 The measurement setup for the main rotor mechanism. 85
4.7 Experimental results of the collective pitch versus swashplate displacement and comparison to the nonlinear model and linear approximation. 86

4.8 Experimental results of the lateral cyclic pitch versus swashplate orientation and comparison to the nonlinear model and linear approximation. 87
4.9 Experimental results of the longitudinal cyclic pitch versus swashplate orientation and comparison to the nonlinear model and linear approximation. 88
4.10 Experimental results of the tail blade pitch versus tail servo arm input and comparison to the nonlinear model and linear approximation. 88

5.1 Aerodynamic force measurement testbed around hover. 92
5.2 Schematic of the testbed interface assembly. 93
5.3 Main rotor thrust and drag torque vs. collective input under these conditions: $\Omega = 1100$ rpm; $R_{mr} = 0.95$ m; $\rho = 1.107$ kg/m^3; $\sigma_{mr} = 0.06$. 94
5.4 Main rotor drag torque vs. thrust under these conditions: $\Omega = 1100$ rpm; $R_{mr} = 0.95$ m; $\rho = 1.107$ kg/m^3; $\sigma_{mr} = 0.06$. 96
5.5 Tail rotor thrust and drag torque vs. pedal input under these conditions: $\Omega_{tr} = 6600$ rpm; $R_{tr} = 0.15$ m; $\sigma_{tr} = 0.11$. 97
5.6 Actual and predicted roll and pitch responses and input excitations under these conditions: $\Omega = 1100$ rpm; $\rho = 1.107$ kg/m^3 (identification). 100
5.7 Frequency response comparison between the simulation and real flight test of the normalized pitch and roll rate responses at the sample rate of 20 Hz. 101
5.8 Actual and predicted yaw response under these conditions: $\Omega = 1100$ rpm; $\rho = 1.107$ kg/m^3 (identification). 103
5.9 Actual and predicted heave response under these conditions: $\Omega = 1100$ rpm; $\rho = 1.107$ kg/m^3 (Identification). 104
5.10 Flight paths used for the longitudinal and lateral velocity identification and validation. 105
5.11 Actual and predicted longitudinal and lateral velocity responses on the circular path A under these conditions: $\Omega = 1100$ rpm; $\rho = 1.107$ kg/m^3 (Identification). 106
5.12 Actual and predicted roll response (Validation). 107
5.13 Actual and predicted pitch response (Validation). 108

5.14 Actual and predicted yaw response (Validation). 109
5.15 Actual and predicted yaw response (Validation). 111
5.16 Actual and simulated heave response in a low-speed vertical descent (Validation). 112
5.17 Actual and simulated heave response in a low-speed vertical climb (Validation). 113
5.18 Actual and simulated heave response in a high-speed vertical climb (Validation). 114
5.19 Actual and predicted longitudinal and lateral velocity responses on the circular flight path B (Validation). 114
5.20 Actual and predicted roll and pitch responses and input excitations (identification). 115
5.21 Actual and predicted roll response(Validation). 116
5.22 Actual and predicted pitch response (Validation). 116

6.1 The trajectory of the CG and control point (figure-8 trajectory). . 122
6.2 The position components of the control point and yaw angle (figure-8 trajectory). 124
6.3 The error components of the control point position (figure-8 trajectory). 124
6.4 The control inputs: collective, longitudinal/latitude cyclic and pedal (figure-8 trajectory). 125
6.5 The attitude of the helicopter: roll, pitch and yaw Euler angles (figure-8 trajectory). 126
6.6 The position components of the helicopter CG (figure-8 trajectory). 127
6.7 The trajectory of the CG and control point (circular trajectory). . 128
6.8 The position components of the control point and yaw angle subject to a wind disturbance of 4 m/s from 110-160 s (circular trajectory). 129
6.9 The error components of the control point position subject to a wind disturbance of 4 m/s from 110-160 s (circular trajectory). . . 129
6.10 The attitude of the helicopter: roll, pitch and yaw Euler angles subject to a wind disturbance of 4 m/s from 110-160 s (circular trajectory). 130

6.11 The control inputs: collective, longitudinal/latitude cyclic and pedal subject to a wind disturbance of 4 m/s from 110-160 s (circular trajectory). 131

7.1 Front and side views of the HIL testbed. 137
7.2 HIL Testbed schematics, front and side views. 138
7.3 Block diagram of the HIL simulation. 140
7.4 Testbed mechanism. 141
7.5 HIL testbed setup for the longitudinal control in hover. 145
7.6 HIL testbed setup for the roll control in hover. 146
7.7 HIL testbed setup for the yaw control. 146

8.1 Position and velocity of the control point in the longitudinal control - the two overshoots at 8.5 and 21 s are due to the intentional external disturbances. 150
8.2 Closed-loop pitch response and longitudinal cyclic input in the presence of intentional external disturbances. 151
8.3 Position and velocity of the control point and error in the forward flight trajectory tracking control. 152
8.4 Closed-loop pitch response and longitudinal cyclic input in the forward flight trajectory tracking control. 153
8.5 Figure-8 desired trajectory. 154
8.6 Position and velocity of the control point and error in the figure-8 trajectory tracking control. 155
8.7 Closed-loop pitch response and longitudinal cyclic input in the figure-8 trajectory tracking control. 156
8.8 Position and velocity of the control point in the lateral control - the three overshoots at 7, 13 and 19 s are due to the external disturbances. 157
8.9 Closed-loop roll response and lateral cyclic input in the presence of external disturbances. 158
8.10 Position and velocity of the control point and error in the sideways flight trajectory tracking control. 159
8.11 Closed-loop roll response and longitudinal cyclic input in the sideways flight trajectory tracking control. 160
8.12 Position and velocity of the control point in the figure-8 trajectory tracking control. 161

8.13 Closed-loop roll response and longitudinal cyclic input in the figure-8 trajectory tracking control. 162
8.14 HIL Testbed schematic for the heading experiment. 163
8.15 Closed-loop yaw response to the step trajectory. 164
8.16 Closed-loop yaw response to the figure-8 trajectory - the overshoot at about 60 s is due to the external disturbance applied to the helicopter fuselage at 60 s. 165
8.17 Heading-hold control in real flight. The reference yaw angle is zero. 165
8.18 Position trajectory of the control point. 166
8.19 Velocity trajectory of the control point. 166
8.20 Attitude response (roll and pitch angles). 167
8.21 Lateral and longitudinal cyclic and collective control inputs. . . . 167

A.1 GPS latency from the flight data. 185
A.2 Measured and predicted position data from GPS. 187
A.3 Zoomed measured and predicted position data from 125 to 130 s. 187

Nomenclature

Acronyms

CG	Centre of Gravity
CP	Control Point
DOF	Degree Of Freedom
F-R	Fuselage-Rotor
GPS	Global Position System
HIL	Hardware-In-the-Loop
IMU	Inertial Measurement Unit
MIMO	Multi-Input Multi-Output
PID	Proportional-Integral-Derivative
PWM	Pulse Width Modulation
SISO	Single-Input Single-Output
SMC	Sliding Mode Control
SSC	Servo Switch Card
TPP	Tip Path Plane
UAV	Unmanned Aerial Vehicle
VTOL	Vertical Take-Off and Landing
VAF	Variance Accounted For

Symbols

a_1, b_1	Longitudinal and Lateral flapping angles of the main rotor [rad]
A_b, B_a	Flapping cross-coupling derivatives [-]
c_1, d_1	Longitudinal and Lateral flapping angles of the stabilizer bar [rad]
c_{mr}, c_{tr}	Main and tail rotor cord [m]
$C_{D_0}, C_{D0_{tr}}$	Main and tail rotor blade zero lift drag coefficient [-]
$C_{L_\alpha}, C_{L_{tr}}$	Main and tail rotor blade lift curve slope [rad^{-1}]
$C^{vt}_{L_\alpha}, C^{ht}_{L_{tr}}$	Vertical and horizontal tail lift curve slope [rad^{-1}]
C_{L_0}	Zero lift curve slope [rad^{-1}]
$C_{L\alpha}, C_{Ltr}$	Main and tail rotor blade lift curve slope [rad^{-1}]
C_{lon}, D_{lat}	Longitudinal and lateral stabilizer bar input derivatives [-]
d	Control point height from the main rotor hub [m]
I_{xx}, I_{yy}, I_{zz}	Main moments of inertia [kg m^2]
K_λ	Main rotor downwash factor at fuselage [-]
K_β	Hub torsional stiffness [Nm]
K_{lon}	Longitudinal cyclic controls to flap gains [-]
K_{lat}	Lateral cyclic controls to flap gains [-]
K_μ	Speed to flap coefficient [-]
m	Helicopter mass [kg]
n_{tr}	Gear ratio of the tail to main rotor [-]
p, q, r	Angular rates in the body coordinates [rad/s]
PW	Pulse width [s]

R_{mr}	Main rotor radius [m]
R_{tr}	Tail rotor radius [m]
S_x^{fus}	Frontal fuselage area [m^2]
S_y^{fus}	Side fuselage area [m^2]
S_z^{fus}	Vertical fuselage area [m^2]
S_{ht}, S_{vt}	Horizontal and vertical tail area [m^2]
u, v, w	Velocity components of the CG in the body coordinates [m/s]
$u_{_{wind}}$	Wind velocity along x-axis in the body coordinates [m/s]
$v_{_{wind}}$	Wind velocity along y-axis in the body coordinates [m/s]
$w_{_{wind}}$	Wind velocity along z-axis in the body coordinates [m/s]
u_r, u_p, u_n	Air relative velocity comp. in the main rotor {rpn} coord. [m/s]
$u_{r_{tr}}$	Air relative velocity along r-axis in the tail rotor {rpn} coord. [m/s]
$u_{p_{tr}}$	Air relative velocity along p-axis in the tail rotor {rpn} coord. [m/s]
$u_{n_{tr}}$	Air relative velocity along n-axis in the tail rotor {rpn} coord. [m/s]
$V_i, V_{i_{tr}}$	Main and tail rotor induced velocity [m/s]
V_h	Main rotor induced velocity in hover [m/s]
x, y, z	Position of CG in the inertial coordinates [m]
x_{fus}	Tail rotor hub offset from CG along x-axis [m]
x_{ht}	Horizontal tail offset from CG along x-axis [m]
x_{vt}	Vertical tail offset from CG along x-axis [m]
z_{cg}	Main rotor hub height from CG [m]
z_{vt}	Vertical tail offset from CG along z-axis [m]

z_c	Vertical displacement of the swashplate [m]
α_{tail}	Slope of the tail servo angle to the PW of the signal [rad/s]
δ_{col}	Main rotor collective pitch input [rad]
δ_{ped}	Tail rotor blade pitch input [rad]
$\delta_{lon}, \delta_{lat}$	Longitudinal and lateral cyclic pitch input [rad]
δ_x, δ_y	Euler rotation angles of the swashplate [rad]
$\delta_{0_{tail}}$	Y-intercept of the tail servo angle to the PW of the signal [rad]
θ_{mr}	Pitch angle of the main rotor [rad]
θ_{tail}	Pitch angle of the tail rotor [rad]
$\theta_{0_{tail}}$	Zero pitch angle of the tail blade [rad]
λ_0	Main rotor inflow ratio [-]
μ	Advance ratio [-]
$\bar{\mu}$	Advance ratio normalized by $V_h/(\Omega R_{mr})$ [-]
μ_x, μ_y, μ_z	Non-dimensional airflow components [-]
ρ	Air density [kg/m^2]
σ_{mr}, σ_{tr}	Main and tail rotor solidity factor [-]
τ_f	Time-constant of the rotor flapping [sec]
τ_{mr}, τ_{tr}	Main and tail rotor blade element radial distance ratio [-]
τ_s	Time-constant of the stabilizer bar [sec]
υ_a	Axial inflow ratio [-]
ϕ, θ, ψ	Euler angles [rad]
Ψ	Blade azimuth angle [rad]

Ω	Main rotor speed [rad/s]

Subscripts

fus	Fuselage
ht	Horizontal tail
mr	Main rotor
tr	Tail rotor
vt	Vertical tail

Chapter 1

Introduction

Autonomous control design for small-scale unmanned helicopters has received growing attention in recent years. The advent of lightweight and low-cost avionics and onboard computers, combined with excellent maneuverability, ability for vertical take-off and landing (VTOL), hovering and low-speed flight capability have made them an ideal choice for a variety of applications. Some applications are search and rescue, powerline inspection, gas leak detection, border and coastal patrolling, police enforcement, reconnaissance and aerial mapping.

In the following, the control design challenges for small-scale helicopters and the proposed solutions in literature are introduced. The thesis overview and organization is then outlined in this chapter.

1.1 Control Design Challenges and Proposed Solutions

A small-scale helicopter is a 6-degree of freedom (6-DOF) multibody system which is composed of a main rotor to control the vertical motion, a tail rotor to control the heading angle and a rigid fuselage between the main and tail rotors. The longitudinal and lateral motion are resulted from tilting of the main rotor disk towards the longitudinal and lateral directions. The collective pitch of the main blades controls the amount of the thrust generated by the main rotor while cyclic

pitch of the blades controls the tilting of the rotor disk. The collective pitch of the tail blades controls the moment generated around the vertical axis of the vehicle.

There are considerable challenges in the control of small-scale helicopters due to their high-dimensional, nonlinear, non-minimum phase and underactuated dynamics as well as inherent instability and strong couplings between the different DOFs.

In non-model-based control approaches such as fuzzy logic [1], reinforcement learning [2] and neural network [3], the dynamic model of the helicopter is either completely neglected or a very rudimentary model is used. Therefore, any deviations from the flight conditions in which they are trained could result in instability of the closed-loop system. Model-based control approaches are better suited for the control of small-scale helicopters as they capture a more accurate model of the system dynamics and its parameter variations due to the changes in the flight conditions.

Both linear and nonlinear approaches have been studied in the literature for the model-based control of small unmanned helicopters. A multi-loop control approach is commonly used in most linear control designs due to the time-scale difference between the translational and attitude subsystems of the helicopter [4, 5, 6, 7, 8, 9]. In this approach, each input controls one helicopter output in a single-input single-output (SISO) feedback loop and the attitude dynamics of the helicopter is decoupled from the translational motion using two main control loops. The slower outer-loop, controls the heave, longitudinal and lateral motion by calculating the desired collective command and attitude angles required to fly the helicopter towards its desired path. These desired attitude angles are then used as the reference inputs to the inner feedback loop. The inner-loop is used to control the attitude of the helicopter which has a much faster time-constant

than the translational motion.

A linearized model of the helicopter dynamics is used in the multi-loop approach and the cross couplings between different DOFs are neglected. Since the cross coupling dynamics is important, this often results in a poor performance of the controller. To account for the cross couplings that exist between different DOFs of the helicopter, a multi-input multi-output (MIMO) control approach has been used in recent years [10, 11, 12].

A MIMO approach for the control of small-scale helicopters is presented in [10] using the input-output feedback linearization technique. The exact input-output linearization fails to linearize the helicopter dynamics and results in having unstable zero dynamics. Then, the zero dynamics are stabilized by neglecting the couplings between moments and forces and using approximate input-output linearization and bounded tracking is achieved in simulation. To present the system in an input-affine form, unrealistic control inputs including the derivatives of the main and tail rotor thrust and the flapping angles are used instead of the physically-controllable inputs such as the collective, cyclic and pedal inputs.

Another MIMO approach is described in [11] to control small-scale helicopters in hover using a backstepping technique. To do this, the flapping dynamics and small body forces are neglected and a simplified model of the helicopter dynamics around hover is used for the control design. In [12], a MIMO control design for a small-scale helicopter using a discrete-time backstepping technique is presented. To obtain the dynamic model of the helicopter in a cascade form suitable for the backstepping control design, simplifying assumptions are used. For example, the induced velocity is assumed constant in all flight regimes and the effects of the vehicle velocities in the thrust calculations are neglected to obtain the thrust of the main and tail rotors proportional to the collective and pedal inputs, respectively. Also, the drag torque of the main and tail rotors are neglected.

Another nonlinear control design using a cascade approach is presented in [13]. An inner-outer loop control structure is used to decouple the attitude and translational dynamics. Simplifying assumptions are used for the control design. For example, the contribution of the roll and pitch moments due to the stiffness of the main rotor hub to the attitude dynamics of the fuselage is neglected. Also, the contribution of the small body forces due to the rotor flapping to the translational dynamics is neglected. Then, a nonlinear control method is used to compensate for the contribution of the tail rotor to the small body forces.

Control design using H_∞ loop-shaping technique for a Yamaha R-50 helicopter is presented in [14, 15]. The control design is based on an inner-loop outer-loop technique in which a 30-state nonlinear model of the helicopter dynamics is linearized around several operating points on the desired flight envelope. Then, based on the obtained linear models a gain-scheduled H_∞ loop-shaping controller is designed to cover this desired flight envelope.

A nonlinear model predictive tracking control (NMPTC) algorithm is presented in [16] for a Yamaha R-50 helicopter. The nonlinear model of the helicopter dynamics is discretized, then the tracking control problem is formulated as a cost minimization problem which is solved by a fast-converging gradient-descent method. Tuning of the cost weight matrices and constants in the potential function are found to be the major implementation issues.

A state-dependent Riccati equation (SDRE) design is presented for the XCell-90 and Yamaha R-Max helicopter platforms in [17]. The nonlinear helicopter dynamics are manipulated into a pseudolinear state-dependent coefficient (SDC) form and then an optimal feedback gain matrix is calculated at every time step by solving the standard linear quadratic regulator (LQR) problem. Due to the existence of various non-parameterizable terms into SDC form and the fact that the helicopter model is not linear with respect to the controls (non affine-in-

control), some nonlinearities of the model are neglected to obtain a control-affine SDC formulation of the helicopter dynamics required for the SDRE control design. A nonlinear compensator is then designed to augment the control input so that the neglected nonlinearities are approximately cancelled.

Due to its robustness to the bounded uncertainties and external disturbances, sliding mode control (SMC), [18], is another nonlinear MIMO approach suitable for the control of small-scale unmanned helicopters. A robust nonlinear flight control using SMC for a small-size autonomous helicopter in hover is presented in [19]. The nonlinear helicopter dynamic is first simplified by neglecting the drag torque of the main and tail rotors as well as the couplings between the aerodynamic forces and moments and then linearized using the feedback linearization technique. Then the linearized model is converted into a canonical form to obtain a square model. To present the system in an input-affine form, unrealistic control inputs including the roll, pitch and yaw moments and the second derivative of the main rotor thrust are used instead of the physically-controllable inputs.

Another SMC approach is described in [20] for the translational rate command (TRC) control of a Bell 205 helicopter in hover. A linearized model of the helicopter around hover in a canonical form is used and a SMC is designed to meet the handling quality specifications for the TRC control in hover.

Other SMC control of small-scale helicopters with a linearized helicopter dynamics around hover for the control design are presented in [21, 22, 23, 24]. A model reference SMC design for the hover control of a small indoor helicopter is described in [21] and a multi-loop control approach is used. The nonlinear model of the helicopter is linearized around hover and the coupled motion of the helicopter is disregarded so that each DOF is treated as an independent SISO system. Then, a SMC is designed for each of the longitudinal and lateral control loops and the proportional-integral-derivative (PID) method is used for the heave

and yaw control loops.

Another SMC approach to control a small-size helicopter is described in [22]. A multi-loop control structure is used in this approach to decouple the DOFs of the helicopter motion using these three main control loops: position, velocity and attitude loops. Equations of each loop are simplified to obtain a suitable form for the SMC algorithm. For example, the small angle assumption is used for the Euler angles in the velocity loop to linearized the equations and obtain an input-affine form. Then, a SMC is designed for each loop.

Formation control of a group of small-size autonomous helicopters using SMC approach is proposed in [25]. Two leader-follower control schemes are introduced to obtain arbitrary three-dimensional formations and for each scheme a sliding mode controller is designed to maintain the formation. The flapping dynamics of the rotor is neglected and unrealistic control inputs including the main and tail rotor thrust and roll and pitch moments are used instead of the physically-controllable inputs to represent the system in an input-affine form. A control-point approach is then used to obtain the square form for the control design.

The helicopter dynamics is divided into three time-scale subsystems with slow, middle and fast modes and a multi-timescale control based on SMC algorithm is used in [26]. The nonlinearities regarding the main and tail rotor inflow are eliminated and the induced velocity is assumed to be constant in all flight regimes. For each mode a nonlinear controller is designed using SMC and simulation results are presented. However, the slow-mode controller requires iteration to solve for the control inputs which can result in a non-unique solution.

Most control designs in the literature including both the multi-loop and MIMO control approaches use the linearized model of the helicopter around different trim conditions instead of directly using the nonlinear model. This restricts the validity of the linear model to the vicinity of the trim conditions around which

it is linearized. So multiple linear models are required to cover a wide range of flight regimes and multiple gain-scheduled controllers are needed to control the helicopter in all these regimes [27]. The complex aerodynamic nature of the thrust generation in helicopters cause the aerodynamic forces and moments to change significantly between different flight conditions. These simplifications by linearization and/or cancellation of the nonlinear terms or by neglecting couplings between the aerodynamic forces and moments are not desirable when controlling an unmanned helicopter for a wide range of flight regimes [28].

1.2 Thesis Overview

Most MIMO model-based nonlinear control approaches require the dynamic model of the system to be: (1) affine-in-control, i.e. linear with respect to the control inputs, and (2) fully actuated i.e. having equal number of DOFs and control inputs. Since the existing formulations for helicopter nonlinear dynamic model do not meet these requirements, these MIMO approaches cannot be applied for control of helicopters.

The purpose of this work is to derive the 6-DOF nonlinear model of the helicopter that is affine-in-control, non-iterative and has a square input-output form. This will allow for many nonlinear control approaches that require a control-affine and square model such as the sliding mode control (SMC), feedback linearization, etc. to be used for control design of small-scale helicopters. A 6-DOF nonlinear model must be sufficiently accurate to represent the behaviour of the actual helicopter. This requires a detailed model of the aerodynamic forces and moments generated by the main and tail rotors, fuselage-rotor couplings and the inverse kinematics of the actuating mechanisms of the main and tail rotors. Also, this model must be identified to obtain its unknown parameters and validated to be used for control design.

This thesis is organized into nine chapters with the chapter content shown schematically in Figure 1.1. Chapter 1 contains the introduction, control design challenges, literature review and thesis goals. In Chapter 2, the experimental setup is described. This includes a small-scale helicopter airframe, custom avionics, ground station and autopilot software, used for the identification and validation of the mathematical model of the helicopter and control implementation. The GPS latency problem and the proposed solution is also discussed. For the 6-DOF nonlinear dynamics of a small-scale helicopter, a new control-oriented model in a square and affine-in-control formulation is developed in Chapter 3. The new model is non-iterative and is derived using a combination of first-principles and system identification. The control point approach is then used to obtain the square input-output formulation. The rotational dynamics of the helicopter is modeled using two methods: (1) a hybrid model, and (2) using first-principles which are compared. In addition, the influence of the gyroscopic effect of the rotor on the roll and pitch responses is examined in Chapter 3. The inverse kinematics of the main rotor actuating mechanism including a 4-point swashplate mechanism and the Bell-Hiller mixer as well as the tail rotor kinematics are derived in Chapter 4. The nonlinear kinematic model is validated using experiments and compared with the linear approximations in Chapter 4.

In Chapter 5, a time-domain identification strategy is developed to identify the unknown parameters of the nonlinear model of the helicopter derived in Chapter 3, using a combination of ground and flight test data. The ground tests are performed using an aerodynamic force measurement testbed to identify the lift and drag coefficients of the main and tail rotors. Flight tests are conducted to identify the unknown parameters of the coupled fuselage-rotor (f-r) dynamic model and empennage drag in a sequential identification process. The identified model is then cross validated in Chapter 5 using flight test data. A robust

sliding mode control (SMC) is designed in Chapter 6 using a combination of the 6-DOF nonlinear square control-affine model of the helicopter and inverse kinematics of the actuating mechanisms derived in Chapters 3 and 4. Simulations are performed to test the performance of the controller in the tracking of complex trajectories in the presence of parameter uncertainties and wind disturbances.

In Chapter 7, a hardware-in-the-loop (HIL) testbed is designed for small unmanned helicopters to provide an intermediate step between simulation and real flight test and allow for implementation issues on the real hardware to be tested. The testbed provides a safe and low-cost platform to implement control algorithms and tune the control gains. It also allows for testing the robustness of the controller to external disturbances in a controlled environment. The experimental results of the SMC implementation on the actual helicopter using the HIL testbed are presented in Chapter 8. The HIL testbed experiments include hover, forward, sideways and figure-8 trajectories for the longitudinal and lateral control, and step and figure-8 trajectories for the heading control. The experimental results from the real flight tests are presented for the heading-hold and hover maneuvers in Chapter 8. Major results and recommendations for future research are presented in Chapter 9.

1.3 Thesis Contributions

The major contributions of this thesis are outlined in the following:

1. A new control-oriented model in an affine-in-control, non-iterative and square input-output formulation for the 6-DOF nonlinear dynamics of a small-scale helicopter is derived. The hybrid model and first-principles approaches for modeling the rotational dynamics of the helicopter are compared. The influence of the gyroscopic effect of the rotor on the roll and

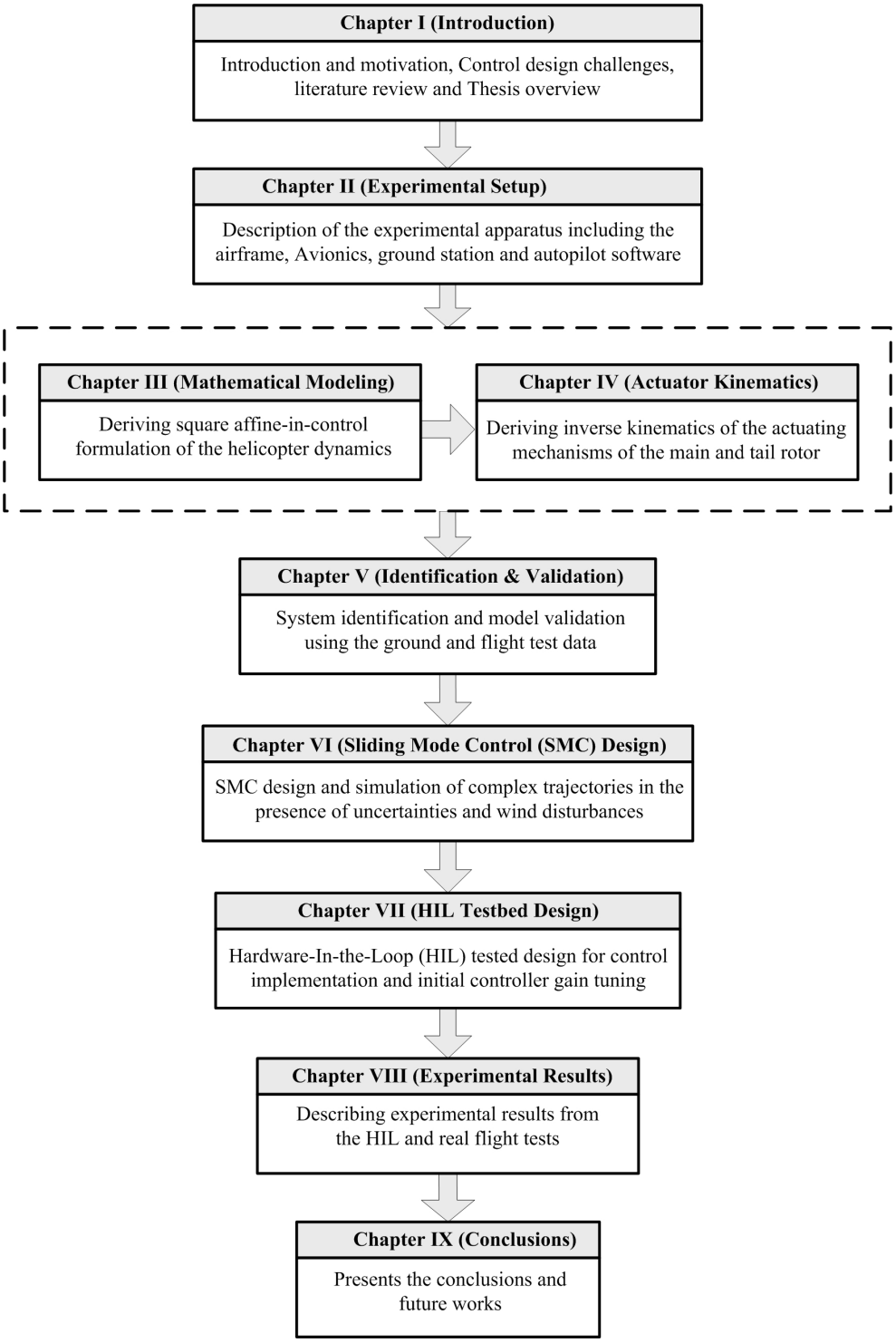

Figure 1.1: Schematic of the thesis organization.

pitch dynamics of the helicopter is studied [29, 31].

2. The inverse kinematics of the actuating mechanism of the main rotor including a 4-point swashplate mechanism and the Bell-Hiller mixer as well as the kinematics of the tail rotor are derived using a fast approach suitable for the real-time control applications. The inverse kinematics is validated using experiments and compared to the linear approximations [32].

3. A time-domain system identification strategy using a combination of ground and flight test data to identify the unknown parameters of the nonlinear model of the helicopter is developed. The identified model is validated using flight test data in the time-domain [33].

4. A robust SMC is designed using the new formulation of the helicopter dynamics. Three-dimensional complex trajectory tracking simulations are performed and the robustness of the controller to the parameter uncertainties and wind disturbances is examined [31].

5. A HIL testbed for small unmanned helicopters for the control implementation, initial controller gain tuning and testing the robustness of the controller to external disturbances in a controlled environment is designed and tested [30, 34]. A SMC, designed based on the new formulation of the helicopter dynamics, is implemented on an Evolution-Ex helicopter using the HIL testbed and the robustness of the controller to external disturbances is verified [34].

Chapter 2

Experimental Setup

The complete experimental apparatus used in this work is composed of: a small-scale helicopter airframe, avionics and electronic hardware, ground station, communications and autopilot software subsystems. The experimental apparatus is designed for the identification and validation of the mathematical model of the helicopter as well as control implementation hardware and software.

2.1 Helicopter Airframe, Avionics and Electronic Hardware

The helicopter airframe is an Evolution-Ex helicopter shown in Figure 2.1, which is an electric powered R/C helicopter weighing 8 kg with a blade span of 1.9 m and capable of carrying a payload of about 8 kg. The rotor hub is hingeless, equipped with a Bell-Hiller stabilizer bar (flybar) and the main and tail rotor blades have symmetrical airfoils.

Custom helicopter avionics is shown in Figure 2.2. The avionics weighs 3.5 kg and consists of: a Crossbow NAV440 inertial measurement unit (IMU), a pair of Xstream RF modems for wireless communications between the helicopter and the ground station, a servo switch card (SSC), a laser range sensor for precise landing, a 3-cell Lithium-Polymer (LiPo) battery, a microcontroller for the battery voltage and current monitoring and an onboard PC/104 computer.

Figure 2.1: Evolution-EX helicopter with Avionics.

The Crossbow NAV440 inertial measurement unit (IMU) shown in Figure 2.2 is a GPS-aided inertial navigation system, which includes three rate gyros, accelerometers, a 3-axis magnetometer and a 4 Hz global positioning system (GPS) receiver with a rugged enclosure to protect the module from the environment. The NAV440 IMU module provides inertial data including the Euler angles, roll, pitch and yaw rates, velocity and accelerations as well as the position of the vehicle at a rate of 20 Hz. The NAV440 module does not directly measure the velocity of the vehicle, but obtains the velocity through integration of the data from the accelerometers and the integration drift is corrected using the GPS data through a built-in Kalman filter. The data communication to the PC/104 is through the serial port RS-232.

A Microbotics servo switch card (SSC) is a multiplexing switch for servo command signals used for switching between the manual radio and automatic control during the control implementation and is shown in Figure 2.3. Recording the pilot commands to the servos during the identification and validation tests is also done on the SSC. The data communication to the PC/104 is through the serial port RS-232.

The PC/104 onboard computer module is an embedded computer with a

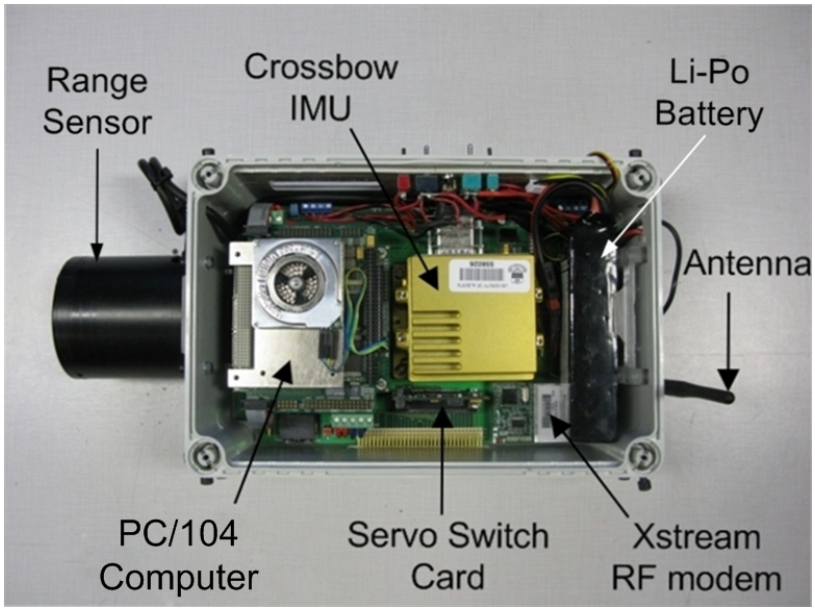

Figure 2.2: Avionics of the helicopter.

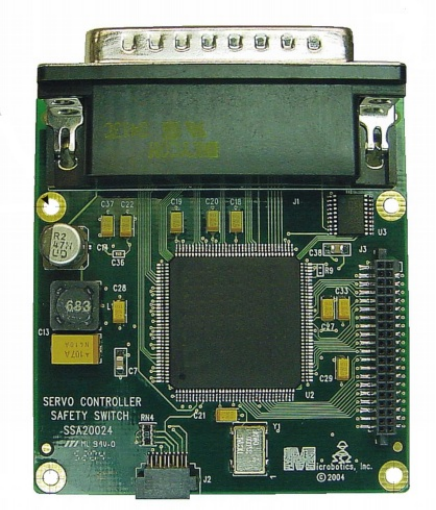

Figure 2.3: Microbotics Servo Switch Card (SSC) module.

Pentium M 1.4 GHz CPU, 512 MB RAM and a 8 GB compact flash (CF) memory composed of multiple modules above each other including the CPU, power supply and data acquisition modules. Since PC/104 has only two serial ports and the data communication of the RF communication, IMU, SSC and Range sensor modules are through the serial port RS-232, a Diamond Emerald MM-8 serial multiplexer stack is used to extend the serial ports of the PC/104 computer.

To accurately measure the speed of the main rotor, an Allegro ATS616 hall-effect sensor attached underneath of the main gear of the rotor is used. The data from the hall-effect sensor is recorded by the SSC module.

All the modules are connected via a custom motherboard to allow for reliable communications between the modules. More details on the avionics and the electronic hardware of this work can be found in [35].

2.2 Ground Station and Communications

To monitor the status of the helicopter during the flight, a ground station system including a ground station laptop, communication modules and a high-gain omnidirectional antenna is used as shown in Figure 2.4. The ground station is also used to update the control gains during the flight to allow the control gain tuning.

A pair of Xstream RF modules are used to communicate between the ground station and the helicopter. The RF module on the ground sends a request for data signal which is amplified by a high-gain omnidirectional antenna and transmitted to the onboard RF module. The onboard RF module obtains the required helicopter data including the altitude, attitude and heading information, rotor speed, voltage and current of the main rotor, avionics and servo batteries from the IMU and other sensors. This data is transmitted by the RF module on the helicopter back to the ground station.

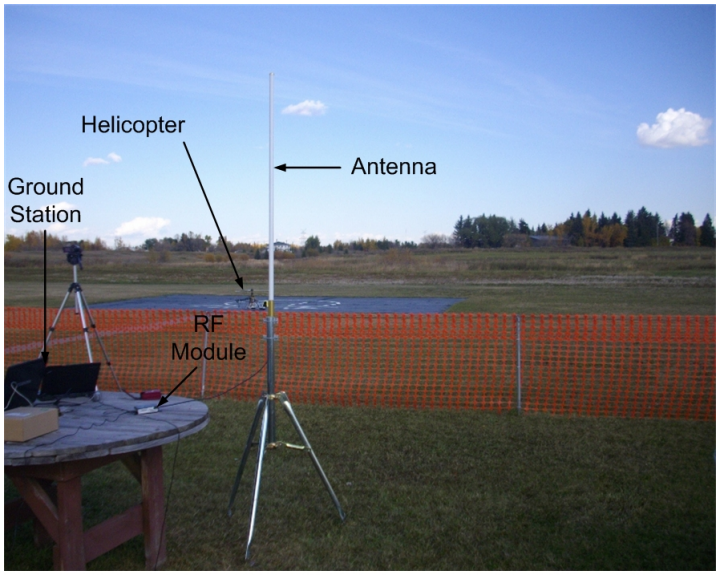

Figure 2.4: Ground station.

A graphical user interface (GUI), shown in Figure 2.5, on the ground station computer is used to monitor the helicopter states. The GUI allows for an efficient monitoring of all the status data received from the helicopter during the flight including the altitude, attitude and heading information, rotor speed, and voltage and current of the main rotor, avionics and servo batteries.

The GUI, shown in Figure 2.6, also allows updating all the control gains during the flight.

2.3 Autopilot Software and Control Implementation

A real-time operating system is critically important for the implementation of the control algorithms on a helicopter platform and to implement the control algorithm designed in this work in real-time. Here the xPC Target software is used.

The real-time software environment xPC Target from the Mathworks, gen-

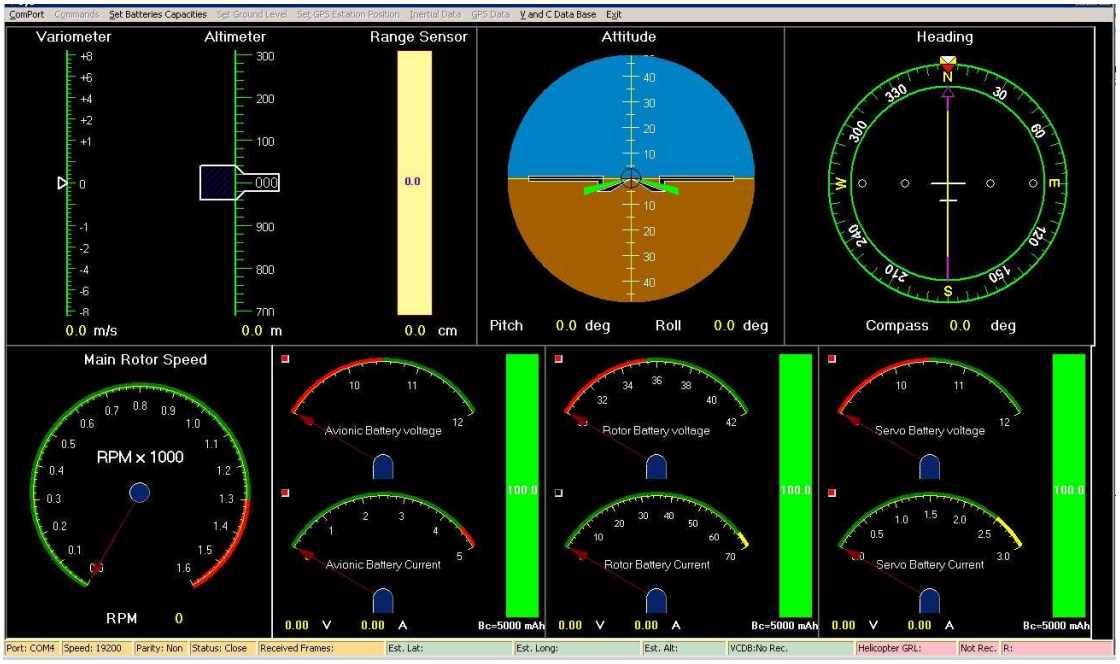

Figure 2.5: Ground station interface.

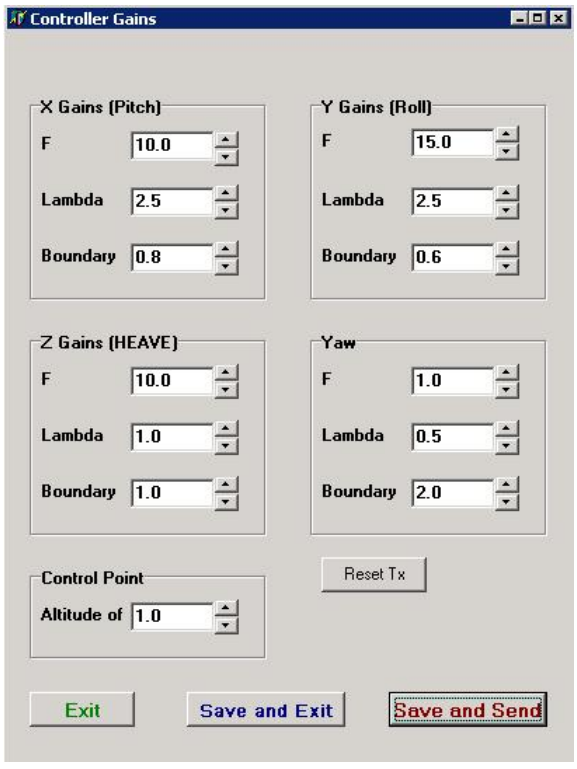

Figure 2.6: GUI for the online updating of the Control Gain.

erates C-code from a Simulink^{TM}model and allows for a rapid controller development and real-time implementation. The xPC Target software supports the PC/104 computer, serial multiplexer board and data communications through serial ports, and has an embedded option allowing for the stand-alone implementation of the controller onboard. It also facilitates all the linear algebra operations used in the model-based controller designed in this work.

To facilitate controller modifications and code debugging, the autopilot software is designed in a module-based architecture. The implementation diagram of the autopilot software is shown in Figure 2.7, in which the PC/104 computer receives the data from the IMU, SSC, RF modem, voltage and current microcontroller and range sensor modules through the serial ports. Then, the PC/104 runs the xPC Target real-time kernel at the sampling frequency of 40 Hz and calculates the servo inputs. The servo inputs are then implemented on the helicopter through the SSC module.

2.4 GPS Latency

One of the challenges in the implementation of the controller is dealing with a phenomenon called GPS latency. GPS data is used in the inertial navigation system to compute the position of the helicopter with respect to the inertial frame. The GPS receiver often uses the time and position data from four satellites to calculate the position of the vehicle. Due to the variety of reasons such as the number of visible satellites and position data computation and transmission delays, GPS data is typically processed at a lower rate than the other IMU data, which results in a delay in the position determination. This phenomenon is called GPS latency. To solve this problem, a 9^{th}-order Kalman filter observer is designed with details in Appendix A.

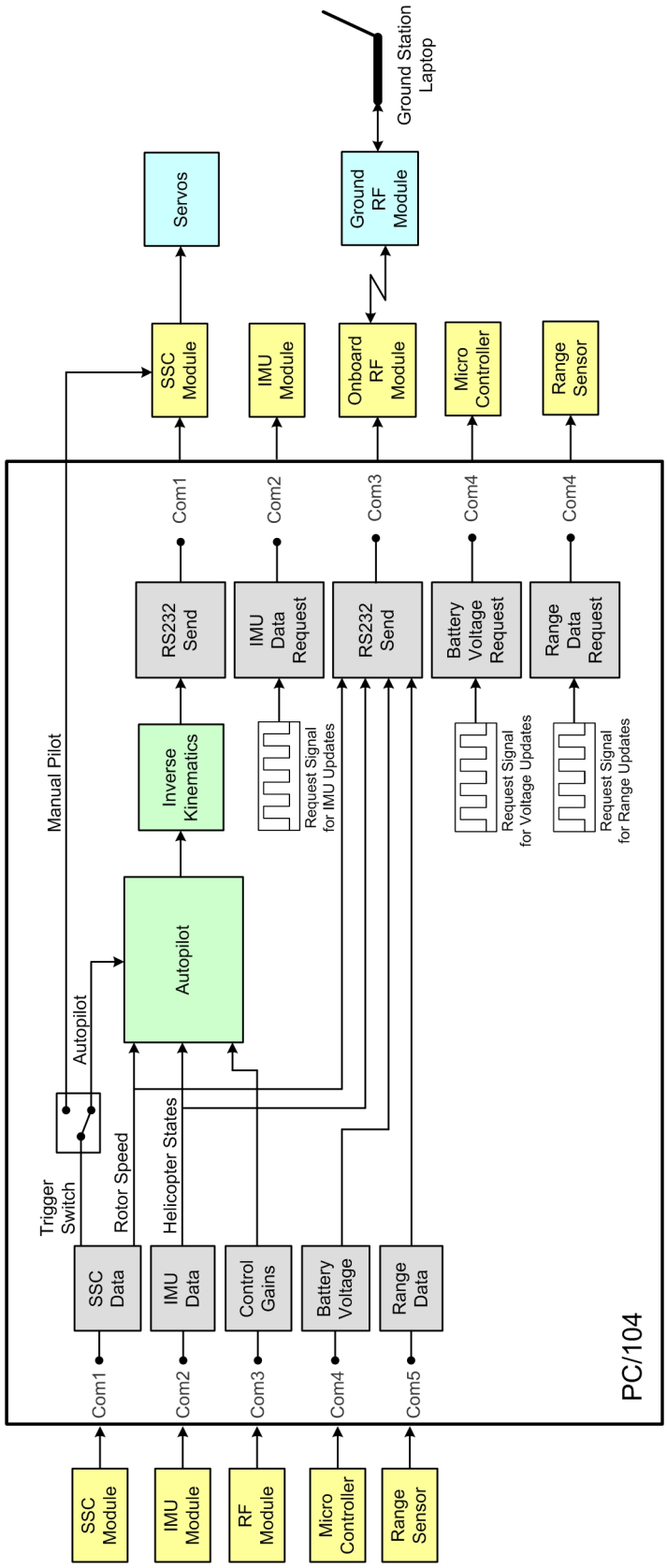

Figure 2.7: Implementation diagram of the autopilot software.

2.5 Summary

An experimental platform composed of a small-scale helicopter airframe, avionics, ground station and autopilot software has been developed for the identification and validation of the mathematical model of the helicopter and control implementation purposes. A ground station is developed to allow for monitoring the status of the helicopter during the flight. That also allows control gain tuning during helicopter operation. Autopilot software is developed using the xPC Target solution to allow for the real-time implementation of the control algorithm. The autopilot software is designed in a module-based architecture to facilitate controller modifications and code debugging. A Kalman observer is designed to deal with the GPS latency overcoming one of the important challenges in the implementation of the controller.

Control-oriented mathematical modeling of the helicopter and subsequent model identification, validation and real-time control implementation on the experimental platform are described in the following chapters.

Chapter 3

Square Affine-In-Control Modeling of the 6-DOF Helicopter Dynamics[1]

Small-scale helicopters have a high-dimensional, highly nonlinear and coupled dynamics with complex rotor aerodynamics. A detailed rotor wake analysis may require advanced experimental and numerical techniques to accurately address the rotor behaviour in various flight regimes [36, 37]. A mathematical model of the helicopter dynamics is needed to design a model-based controller. This model should include the 6-DOF rigid-body dynamics of the helicopter fuselage and the rotor dynamics. Detailed mathematical models of the helicopter dynamics and the aerodynamic forces and moments generated by the subsystems are described in [38, 39, 40]. For example, a 30-state model for a Yamaha R-50 small-scale helicopter that includes fuselage rigid-body dynamics, main rotor, tail rotor, stabilizer bar, dynamic inflow, and actuator dynamics is described in [40]. However, such models are currently impractical for the control design purposes as the number of states is too large and require excessive computation for real-time implementation.

To obtain a simpler control-oriented helicopter dynamic model, a combination of first-principles and system identification is used to derive an affine-in-control

[1] A version of this chapter has been submitted for publication in [31].

and square model of the helicopter nonlinear dynamics. To model the rotational dynamics of the helicopter, two approaches are used: (1) using a "hybrid model approach" as described in section 3.2, and (2) using a "first-principles approach" as described in section 3.8. After being parameterized, both these models are validated and compared to flight test data from an Evolution-EX helicopter (shown in Figure 2.1) in Chapter 5.

3.1 Fuselage Rigid-Body Dynamics

The dynamic response of the Evolution-EX helicopter is modeled as the combination of these four main subsystems: the fuselage rigid-body dynamics, the main rotor, the tail rotor and the empennage. To determine the 6-DOF motion of the helicopter fuselage with respect to the ground, two frames of reference are used as shown in Figure 3.1. Frame {B} is the body coordinate system attached to the helicopter at the center of gravity (CG), and frame {I} is a reference attached to the ground that is assumed inertial.

The states of the helicopter are the linear velocity $\mathbf{v} = [u\ v\ w]^T$, angular velocity $\boldsymbol{\omega} = [p\ q\ r]^T$ in the body coordinates (shown in Figure 3.1), the Euler angles $\boldsymbol{\theta} = [\phi\ \theta\ \psi]^T$, and the position of the helicopter CG with respect to the inertial frame $\mathbf{p} = [x\ y\ z]^T$. The mass and moment of inertia tensor are denoted by m and $\mathbf{I} = \text{diag}_{3\times3}(I_{xx}, I_{yy}, I_{zz})$, in which the off-diagonal terms are neglected. The Newton-Euler equations of motion are used to determine the 6-DOF rigid-

body dynamics of the helicopter fuselage as:

$$\dot{\mathbf{v}} = \frac{1}{m}\mathbf{F} - \boldsymbol{\omega} \times \mathbf{v} \tag{3.1}$$

$$\dot{\boldsymbol{\omega}} = \mathbf{I}^{-1}\mathbf{M} - \mathbf{I}^{-1}(\boldsymbol{\omega} \times \mathbf{I}\,\boldsymbol{\omega}) \tag{3.2}$$

$$\dot{\boldsymbol{\theta}} = \boldsymbol{\Phi}(\boldsymbol{\theta})\,\boldsymbol{\omega} \tag{3.3}$$

$$\dot{\mathbf{p}} = \mathbf{R}_b^I(\boldsymbol{\theta})\,\mathbf{v} \tag{3.4}$$

where $\mathbf{F}$ and $\mathbf{M}$ are the vectors of external forces and moments applied to the helicopter fuselage in the body coordinates, respectively, and $\mathbf{R}_b^I$ and $\boldsymbol{\Phi}$ are the linear and angular velocity transformation matrices from the body to inertial coordinates [17], as follows:

$$\mathbf{R}_b^I = \begin{bmatrix} \mathrm{c}\theta\mathrm{c}\psi & -\mathrm{c}\phi\mathrm{s}\psi + \mathrm{s}\phi\mathrm{s}\theta\mathrm{c}\psi & \mathrm{s}\phi\mathrm{s}\psi + \mathrm{c}\phi\mathrm{s}\theta\mathrm{c}\psi \\ \mathrm{c}\theta\mathrm{s}\psi & \mathrm{c}\phi\mathrm{c}\psi + \mathrm{s}\phi\mathrm{s}\theta\mathrm{s}\psi & -\mathrm{s}\phi\mathrm{c}\psi + \mathrm{c}\phi\mathrm{s}\theta\mathrm{s}\psi \\ -\mathrm{s}\theta & \mathrm{s}\phi\mathrm{c}\theta & \mathrm{c}\phi\mathrm{c}\theta \end{bmatrix}, \quad \boldsymbol{\Phi} = \begin{bmatrix} 1 & \mathrm{s}\phi\mathrm{t}\theta & \mathrm{c}\phi\mathrm{t}\theta \\ 0 & \mathrm{c}\phi & -\mathrm{s}\phi \\ 0 & \frac{\mathrm{s}\phi}{\mathrm{c}\theta} & \frac{\mathrm{c}\phi}{\mathrm{c}\theta} \end{bmatrix}$$

with "s", "c", and "t" corresponding to "sin", "cos", and "tan", respectively. Next, a non-iterative simplified model is derived for the aerodynamic forces and moments generated by the main and tail rotors and the empennage of a small-scale helicopter.

3.2 Main Rotor

This section outlines the forces and moments generated by the main rotor and their control-affine representation.

The pitch angle of the rotor blades can change both collectively and cyclically during rotation around the hub. The main rotor pitch angle can be represented using the first harmonic components of the Fourier series expansion in terms of

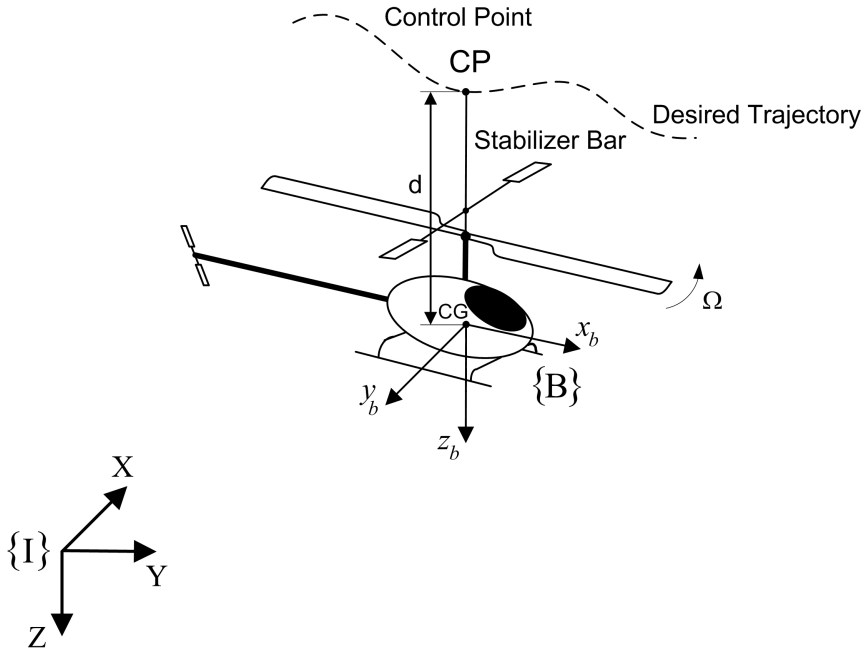

Figure 3.1: Schematic of the helicopter with the control point CP.

the blade azimuth angle Ψ, shown in Figure 3.3, as:

$$\theta_{mr} = \delta_{col} + \delta_{lat}\cos(\Psi) + \delta_{lon}\sin(\Psi) \tag{3.5}$$

The collective pitch angle δ_{col} controls the thrust to give helicopter the lift required for the vertical motion. The longitudinal δ_{lon} and lateral δ_{lat} cyclic pitch angles control the pitch and roll motion, by generating more lift on one side of the main rotor than the other.

To calculate the induced forces and moments on the helicopter fuselage, a model of the rotor flapping dynamics is required since the main rotor is coupled to the fuselage angular and translational dynamics through the rotor flapping dynamics. The coupled fuselage-rotor-stabilizer bar (f-r) dynamics is commonly represented by the "hybrid model approach" [41]. In this approach, the rotor flapping dynamics is approximated by the tip-path-plane (TPP) flapping with

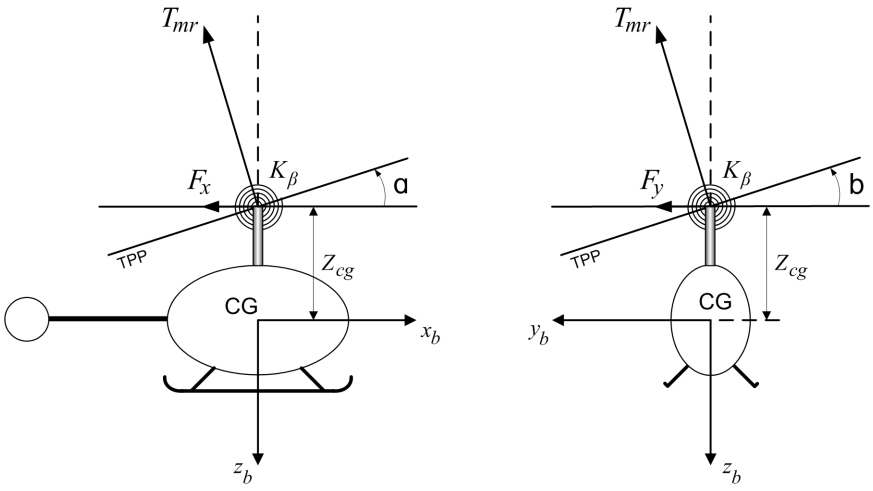

Figure 3.2: Longitudinal and lateral flapping schematics of the main rotor.

two states a_1 and b_1 which are the longitudinal and lateral flapping angles, respectively. The states a_1 and b_1 are the coefficients of the first harmonic approximation in the Fourier series representation of the rotor flapping equations. The flapping dynamics of the main rotor is represented by two first-order differential equations:

$$\dot{a}_1 = -q - \frac{a_1}{\tau_f} + \frac{A_b}{\tau_f} b_1 + \frac{1}{\tau_f}\Big(\frac{\partial a_1}{\partial \mu}\mu_x + \frac{\partial a_1}{\partial \mu_z}\mu_z\Big) + \frac{K_{lon}}{\tau_f}(\delta_{lon} + K_s c_1) \tag{3.6}$$

$$\dot{b}_1 = -p - \frac{b_1}{\tau_f} + \frac{B_a}{\tau_f} a_1 + \frac{1}{\tau_f}\frac{\partial b_1}{\partial \mu_v}\mu_y + \frac{K_{lat}}{\tau_f}(\delta_{lat} + K_s d_1) \tag{3.7}$$

where the non-dimensional airflow components are:

$$\mu_x = \frac{u - u_{_{wind}}}{\Omega R_{mr}}, \quad \mu_y = \frac{v - v_{_{wind}}}{\Omega R_{mr}}, \quad \mu_z = \frac{w - w_{_{wind}}}{\Omega R_{mr}}$$

and K_{lon} and K_{lat} are the corresponding input cyclic controls to flap gains, τ_f is the time-constant of the rotor flapping, A_b and B_a are the flapping cross-coupling derivatives and K_s is the stabilizer bar to rotor flap gain. Also, $u_{_{wind}}$, $v_{_{wind}}$ and $w_{_{wind}}$ are the wind velocity components in the body coordinates and the longitudinal, $\frac{\partial a_1}{\partial \mu}$, and lateral, $\frac{\partial b_1}{\partial \mu_v}$, dihedral stability derivatives represent the

flapping effects due to the translational velocities and are described in [38].

Small-scale helicopters are very agile and responsive vehicles and usually equipped with a stabilizer bar (flybar) to help facilitate their control by a pilot. The stabilizer bar can be considered as a secondary rotor attached to the rotor shaft above the main rotor as shown in Figure 3.1. The stabilizer bar acts as a lagged rate feedback to the f-r dynamics to stabilize the helicopter against rapid changes in the roll and pitch angles (high roll and pitch rates) caused by either the pilot commands or external moments due to wind gusts and can be represented by the following equations [41]:

$$\dot{c_1} = -q - \frac{c_1}{\tau_s} + \frac{C_{lon}}{\tau_s}\delta_{lon} \tag{3.8}$$

$$\dot{d_1} = -p - \frac{d_1}{\tau_s} + \frac{D_{lat}}{\tau_s}\delta_{lat} \tag{3.9}$$

where τ_s is the time-constant of the stabilizer bar and C_{lon} and D_{lat} are the input derivatives.

The roll and pitch moments on the fuselage are generated as a result of the longitudinal and lateral flapping of the TPP, respectively. The coupling of the main rotor to the angular dynamics of the fuselage can be approximated by a linear torsional spring between the rotor and the fuselage with a constant stiffness coefficient K_β, as shown in Figure 3.2. Tilting of the TPP induces rolling and pitching moments on the fuselage. The offset of the TPP from the CG, z_{cg}, also contributes to the generated moments through tilting of the thrust vector. Assuming the small flapping angles, the total moments generated by the main rotor are calculated as:

$$M_{roll} = (K_\beta - T_{mr} z_{cg}) b_1 \tag{3.10}$$

$$M_{pitch} = (K_\beta - T_{mr} z_{cg}) a_1 \tag{3.11}$$

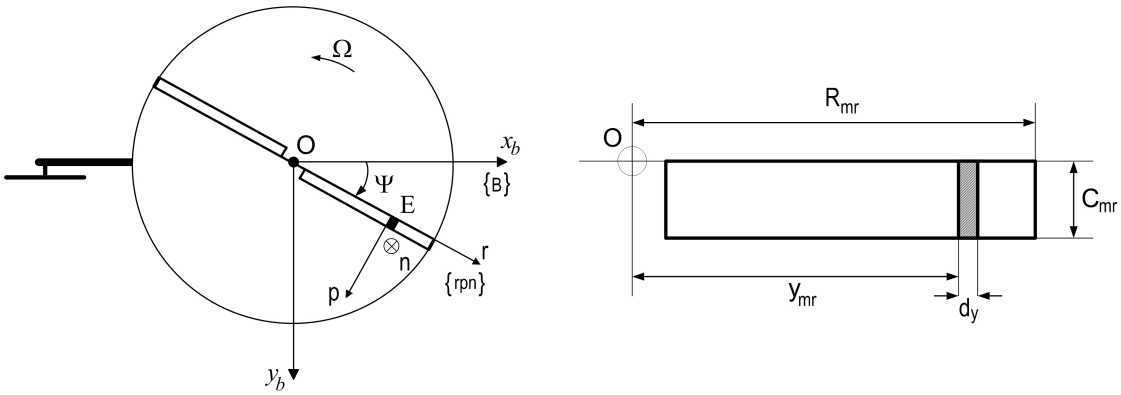

Figure 3.3: Rotor disk and blade strip schematic viewed from above.

The coupling of the main rotor to the translational dynamics of the fuselage is through tilting the rotor TPP towards longitudinal and lateral directions as shown in Figure 3.2. Assuming the small flapping angles, the total forces generated by the main rotor along the longitudinal and lateral axes of the fuselage are:

$$F_x = -T_{mr} a_1 \tag{3.12}$$

$$F_y = T_{mr} b_1 \tag{3.13}$$

The total force and moment contribution of the main rotor are:

$$\begin{aligned} X_{mr} &= F_x + H_{x_{mr}} \\ Y_{mr} &= F_y + H_{y_{mr}} \\ Z_{mr} &= -T_{mr} \\ L_{mr} &= M_{roll} - H_{y_{mr}} z_{cg} \\ M_{mr} &= M_{pitch} + H_{x_{mr}} z_{cg} \\ N_{mr} &= Q_{mr} \end{aligned} \tag{3.14}$$

where $H_{x_{mr}}$ and $H_{y_{mr}}$ are the in-plane forces generated due to the uneven distribu-

tion of the drag on the Tip-Path-Plane (TPP) in forward or sideways maneuvers.

A combination of the blade element theory and momentum theory is used to derive the thrust T_{mr}, drag torque Q_{mr} and in-plane forces $H_{x_{mr}}$ and $H_{y_{mr}}$. The helicopter's velocity vector $\mathbf{v}$ is incorporated into the model to obtain the thrust and drag torque for the main and tail rotors. The helicopter's translational velocity vector in body coordinates $\{B\}$ is resolved into the $\{rpn\}$ coordinates attached to the blade element shown in Figure 3.3. Then, all the elementary aerodynamic forces and moments are averaged around the azimuth angle Ψ and integrated along the blade span.

This provides an analytical representation of the thrust and drag torque as a function of the vehicle's translational and angular velocities which can be used for different flight regimes. The relative air velocity vector of the element E in Figure 3.3 in $\{rpn\}$ frame is:

$$\boldsymbol{V}_E^{rpn} = \mathbf{R}_b^{rpn}(\boldsymbol{V_{rel}} + \boldsymbol{\Omega} \times \boldsymbol{y_{mr}}) \tag{3.15}$$

where $\mathbf{R}_b^{rpn}$ is the rotation matrix from $\{B\}$ to $\{rpn\}$ coordinates as:

$$\mathbf{R}_b^{rpn} = \begin{bmatrix} \mathrm{c}\Psi & \mathrm{s}\Psi & 0 \\ -\mathrm{s}\Psi & \mathrm{c}\Psi & 0 \\ 0 & 0 & 1 \end{bmatrix} \tag{3.16}$$

and $\boldsymbol{y_{mr}} = [y_{mr}\cos\Psi \; y_{mr}\sin\Psi \; 0]^T$ is the vector of the blade element, $\boldsymbol{\Omega} = [0\;0\;\Omega]^T$ is the main rotor angular velocity vector, $\boldsymbol{V_{rel}} = \boldsymbol{v_i} - (\boldsymbol{v} - \boldsymbol{v}_{wind})$ is the vector of relative air velocity, $\boldsymbol{v_i} = [0\;0\;V_i]^T$ is the main rotor inflow vector and $\boldsymbol{v}_{wind} = [u_{wind}\; v_{wind}\; w_{wind}]^T$ is the wind velocity vector - all in the body coordinates. The induced velocity of the main rotor (V_i) will be described later in this section. The non-dimensional velocity components u_r, u_p, and u_n are the normalized air

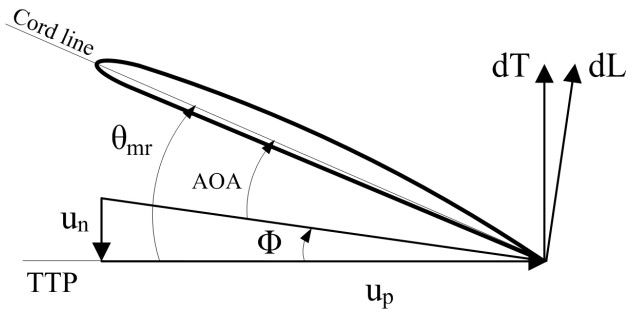

Figure 3.4: Blade section flow conditions in a general flight.

relative velocity components in $\{rpn\}$ coordinates.

The relative air velocity components on the blade section "E" (shown in Figure 3.3) is shown in Figure 3.4. First taking the average from the elementary lift force on the blade section around the azimuth angle Ψ and then integrating along the blade span and considering small inflow angle Φ, the main rotor thrust is calculated as:

$$T_{mr} = \rho\pi R_{mr}^4 \Omega^2 C_T \tag{3.17}$$

where,

$$C_T = \frac{\sigma_{mr}}{4\pi} \int_0^1 \int_0^{2\pi} C_L {u_p}^2 \, \mathrm{d}\Psi \mathrm{d}\tau_{mr}$$

and $C_L = C_{L_0} + C_{L_\alpha}\left(\theta_{mr} - \frac{u_n}{u_p}\right)$ is the lift coefficient, C_{L_α} is the lift curve slope, C_{L_0} is the zero lift curve slope, $\sigma_{mr} = 2c_{mr}/(\pi R_{mr})$ is the solidity factor and $\tau_{mr} = y_{mr}/R_{mr}$.

Defining the input vector $\mathbf{u} = [\delta_{col}, \delta_{lat}, \delta_{lon}, \delta_{ped}]^T$, the main rotor thrust can

be written in the affine-form as:

$$T_{mr} = \mathrm{f}_{_T} + \mathbf{b_T u} \tag{3.18}$$

where,

$$\mathrm{f}_{_T} = \frac{1}{4}\rho\pi R_{mr}^4 \Omega^2 \sigma_{mr}\left(C_{L_0}\left(\frac{2}{3} + \mu_x^2 + \mu_y^2\right) + C_{L_\alpha}(\mu_z - \lambda_0)\right) \tag{3.19}$$

$$\mathbf{b_T} = \frac{1}{4}\rho\pi R_{mr}^4 \Omega^2 \sigma_{mr} C_{L_\alpha} \begin{bmatrix} \mu_x^2 + \mu_y^2 + \frac{2}{3} \\ -\mu_y \\ \mu_x \\ 0 \end{bmatrix}^T$$

and λ_0 is the inflow ratio of the main rotor defined as $\lambda_0 = V_i/(\Omega R_{mr})$.

Note that for symmetrical blades, such as the one used on the Evolution-EX helicopter, the zero lift curve slope coefficient C_{L_0} in Eq. (3.19) is zero, so it is not needed in subsequent calculations.

The thrust in Eqs. (3.18) and (3.19) varies significantly with induced velocity, so it must be accurately determined for the nonlinear model of the helicopter dynamics to be valid over a wide range of flight regimes. Since the induced velocity depends on the thrust and the thrust depends on the induced velocity, an iterative solution is typically used to calculate the induced velocity of the main rotor [38]. This requires excessive computation for real-time implementation.

To find a closed-form solution suitable for real-time control applications and avoid iterative methods, a continuous empirical model, the modified Glauert equation [42], is used to calculate the induced velocity. This method can predict the inflow at all flight regimes through an explicit and continuous solution.

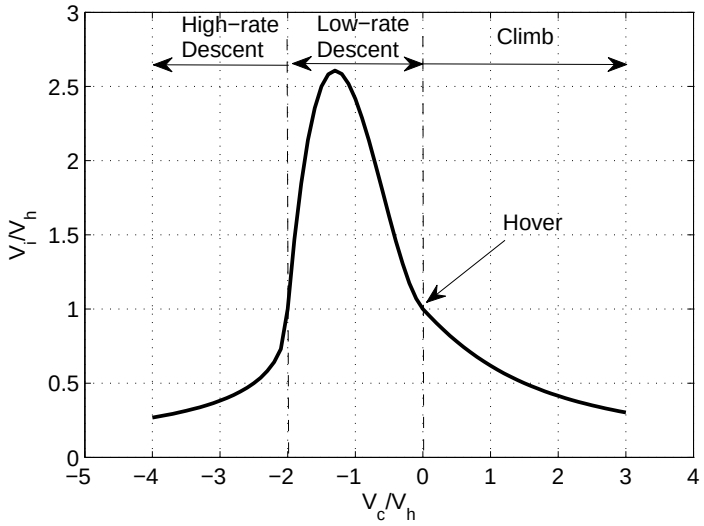

Figure 3.5: Induced velocity profile in the axial flight.

The induced velocity of the main rotor is:

$$V_i = \frac{\upsilon_a V_h}{\sqrt{1+\bar{\mu}^2}} \tag{3.20}$$

where $V_h = \sqrt{mg/(2\rho\pi R_{mr}^2)}$ is the induced velocity in hover, $\mu = \sqrt{\mu_x^2 + \mu_y^2}$ is the advance ratio and $\bar{\mu}$ is the advance ratio normalized by $V_h/(\Omega R_{mr})$.

The axial inflow ratio υ_a is expressed by three continuous piecewise functions as:

$$\upsilon_a = \begin{cases} -\frac{1}{2}V_a - \sqrt{\frac{V_a^2}{4} - 1} & \text{if} \quad V_a \leq -2 \\ 1 - \frac{1}{2}V_a + \frac{25}{12}V_a^2 + \frac{7}{6}V_a^3 & \text{if} \quad -2 < V_a < 0 \\ -\frac{1}{2}V_a + \sqrt{\frac{V_a^2}{4} + 1} & \text{if} \quad V_a \geq 0 \end{cases} \tag{3.21}$$

where V_a is the normal-to-the-disk component of the free stream velocity normalized by V_h. The first and third equations of Eq. (6.6) are equivalent to the momentum theory for the high rate descent and climb regimes respectively. The second equation represents a rational curve-fitting of experimental results to ac-

count for the condition between the vertical climb and windmill brake state, which corresponds to the low-rate descent regimes [42]. Unlike most control-oriented helicopter models which use numerical and iterative methods to calculate the induced velocity, this formulation above provides a non-iterative empirical model of the induced velocity. For example, the induced velocity calculated in the axial flight using Eq. (6.6) is shown in Figure 3.5.

The drag torque of the main rotor due to the profile drag in a similar affine-form is:

$$Q_{mr} = \rho\pi R_{mr}^5 \Omega^2 C_Q \tag{3.22}$$

where,

$$C_Q = \frac{\sigma_{mr}}{4\pi}\int_0^1\int_0^{2\pi}\left(C_L u_p u_n + C_{D_0}{u_p}^2\right)\tau_{mr}\,\mathrm{d}\Psi\mathrm{d}\tau_{mr}$$

and C_{D_0} is the zero lift drag coefficient. Main rotor drag torque in the control-affine form is:

$$Q_{mr} = \mathrm{f}_{_Q} + \mathbf{b_Q}\mathbf{u} \tag{3.23}$$

where,

$$\mathrm{f}_{_Q} = \frac{1}{8}\rho\pi R_{mr}^5\Omega^2\sigma_{mr}C_{L_\alpha}\left(\frac{C_{D_0}}{C_{L_\alpha}}\left(1+\mu_x^2+\mu_y^2\right) - 2(\mu_z-\lambda_0)^2\right)$$

$$\mathbf{b_Q} = \frac{1}{8}\rho\pi R_{mr}^5\Omega^2\sigma_{mr}C_{L_\alpha}(\lambda_0-\mu_z)\begin{bmatrix}\frac{4}{3}\\ -\mu_y\\ \mu_x\\ 0\end{bmatrix}^T$$

The in-plane forces due to the difference in the drag forces generated on the advancing and retreating sides of the main rotor are:

$$H_{x_{mr}} = \rho\pi R_{mr}^4 \Omega^2 C_{H_{x_{mr}}} = \mathrm{f}_{_{H_x}} + \mathbf{b}_{_{H_x}} \mathbf{u} \tag{3.24}$$

$$H_{y_{mr}} = \rho\pi R_{mr}^4 \Omega^2 C_{H_{y_{mr}}} = \mathrm{f}_{_{H_y}} + \mathbf{b}_{_{H_y}} \mathbf{u} \tag{3.25}$$

where,

$$C_{H_{x_{mr}}} = -\frac{\sigma_{mr}}{4\pi} \int_0^1 \int_0^{2\pi} \left(C_L u_p u_n + C_{D_0} {u_p}^2 \right) \sin(\Psi) \, \mathrm{d}\Psi \mathrm{d}\tau_{mr}$$

$$C_{H_{y_{mr}}} = \frac{\sigma_{mr}}{4\pi} \int_0^1 \int_0^{2\pi} \left(C_L u_p u_n + C_{D_0} {u_p}^2 \right) \cos(\Psi) \, \mathrm{d}\Psi \mathrm{d}\tau_{mr}$$

and,

$$\mathrm{f}_{_{H_x}} = -\frac{1}{4} \rho\pi R_{mr}^4 \Omega^2 \sigma_{mr} C_{D_0} \mu_x$$

$$\mathbf{b}_{_{H_x}} = \frac{1}{8} \rho\pi R_{mr}^4 \Omega^2 \sigma_{mr} C_{L_\alpha} (\mu_z - \lambda_0) \begin{bmatrix} 2\mu_x \\ 0 \\ 1 \\ 0 \end{bmatrix}^T$$

$$\mathrm{f}_{_{H_y}} = -\frac{1}{4} \rho\pi R_{mr}^4 \Omega^2 \sigma_{mr} C_{D_0} \mu_y$$

$$\mathbf{b}_{_{H_y}} = \frac{1}{8} \rho\pi R_{mr}^4 \Omega^2 \sigma_{mr} C_{L_\alpha} (\mu_z - \lambda_0) \begin{bmatrix} 2\mu_y \\ -1 \\ 0 \\ 0 \end{bmatrix}^T$$

3.3 Tail Rotor

The force and moment contribution of the tail rotor are:

$$
\begin{aligned}
X_{tr} &= H_{x_{tr}} \\
Y_{tr} &= T_{tr} \\
Z_{tr} &= H_{z_{tr}} \\
L_{tr} &= -T_{tr} z_{_{fus}} \\
M_{tr} &= Q_{tr} + H_{x_{tr}} z_{_{fus}} \\
N_{tr} &= T_{tr} x_{_{fus}}
\end{aligned} \tag{3.26}
$$

The aerodynamic forces and moments generated by the tail rotor are obtained in a similar manner to the main rotor. Tail rotor thrust is:

$$T_{tr} = \rho \pi R_{tr}^4 n_{tr}^2 \Omega^2 C_{T_{tr}} \tag{3.27}$$

where n_{tr} is the gear ratio of the tail to main rotor and $C_{T_{tr}}$ is:

$$C_{T_{tr}} = \frac{\sigma_{tr}}{4\pi} \int_0^1 \int_0^{2\pi} C_{L_{tr}} u_{r_{tr}}^2 \, \mathrm{d}\Psi \mathrm{d}\tau_{tr}$$

where $C_{L_{tr}} = C_{L\alpha_{tr}} \left(\theta_{tr} - \frac{u_{n_{tr}}}{u_{r_{tr}}} \right)$ is the tail rotor lift coefficient and $C_{L\alpha_{tr}}$ is the tail rotor lift curve slope, $\sigma_{tr} = 2c_{tr}/(\pi R_{tr})$ is the tail rotor solidity factor, $u_{r_{tr}}$ and $u_{n_{tr}}$ are the normalized tangential and vertical air relative velocity components in the tail blade coordinates and $\tau_{tr} = y_{tr}/R_{tr}$.

The tail rotor thrust in the control-affine form is:

$$T_{tr} = \mathrm{f}_{_{T_{tr}}} + \mathbf{b}_{\mathbf{T_{tr}}} \mathbf{u} \tag{3.28}$$

where,

$$\mathrm{f}_{_{T_{tr}}} = -\frac{1}{4}\rho\pi R_{tr}^4 n_{tr}^2 \Omega^2 \sigma_{tr} C_{L_{tr}} v_{_{tail}}$$

$$\mathbf{b_{T_{tr}}} = \frac{1}{4}\rho\pi R_{tr}^4 n_{tr}^2 \Omega^2 \sigma_{tr} C_{L_{tr}} \begin{bmatrix} 0 \\ 0 \\ 0 \\ u_{_{tail}}^2 + w_{_{tail}}^2 + \frac{2}{3} \end{bmatrix}^T$$

The non-dimensional variables of the tail rotor are defined as:

$$u_{_{tail}} = \frac{u - u_{_{wind}}}{n_{tr}\Omega R_{tr}}, \quad v_{_{tail}} = \frac{v - v_{_{wind}} - V_{i_{tr}} + x_{_{fus}} r}{n_{tr}\Omega R_{tr}}, \quad w_{_{tail}} = \frac{w - K_\lambda V_i - w_{_{wind}}}{n_{tr}\Omega R_{tr}}$$

where $V_{i_{tr}}$ is the induced velocity of the tail rotor obtained similar to the main rotor in Eq. (6.6) and K_λ is the main rotor downwash on the empennage.

The drag torque of the tail rotor is:

$$Q_{tr} = \rho\pi R_{tr}^5 n_{tr}^2 \Omega^2 C_{Q_{tr}} \tag{3.29}$$

where,

$$C_{Q_{tr}} = \frac{\sigma_{tr}}{4\pi} \int_0^1 \int_0^{2\pi} \left(C_{L_{tr}} u_{r_{tr}} u_{n_{tr}} + C_{D0_{tr}} u_{r_{tr}}^2 \right) \tau_{tr} \, \mathrm{d}\Psi \mathrm{d}\tau$$

The tail rotor drag torque in the control-affine form is:

$$Q_{tr} = \mathrm{f}_{_{Q_{tr}}} + \mathbf{b_{Q_{tr}}} \mathbf{u} \tag{3.30}$$

where,

$$\mathrm{f}_{Q_{tr}} = \frac{1}{8}\rho\pi R_{tr}^5 n_{tr}^2 \Omega^2 \sigma_{tr} C_{L_{tr}} \left(\frac{C_{D0_{tr}}}{C_{L_{tr}}} \left(u_{tail}^2 + w_{tail}^2 + 1 \right) - 2v_{tail}^2 \right)$$

$$\mathbf{b_{Q_{tr}}} = \frac{1}{6}\rho\pi R_{tr}^5 n_{tr}^2 \Omega^2 \sigma_{tr} C_{L_{tr}} \begin{bmatrix} 0 \\ 0 \\ 0 \\ v_{tail} \end{bmatrix}^T$$

The in-plane forces of the tail rotor can be calculated as:

$$H_{x_{tr}} = \rho\pi R_{tr}^4 n_{tr}^2 \Omega^2 C_{H_{x_{tr}}} = \mathrm{f}_{Hx_{tr}} + \mathbf{b}_{Hx_{tr}} \mathrm{u} \tag{3.31}$$

$$H_{z_{tr}} = \rho\pi R_{tr}^4 n_{tr}^2 \Omega^2 C_{H_{z_{tr}}} = \mathrm{f}_{Hz_{tr}} + \mathbf{b}_{Hz_{tr}} \mathrm{u} \tag{3.32}$$

where,

$$C_{H_{x_{tr}}} = -\frac{\sigma_{tr}}{4\pi} \int_0^1 \int_0^{2\pi} \left(C_{L_{tr}} u_{r_{tr}} u_{n_{tr}} + C_{D0_{tr}} u_{t_{tr}}^2 \right) \sin(\Psi) \, \mathrm{d}\Psi \mathrm{d}\tau$$

$$C_{H_{z_{tr}}} = \frac{\sigma_{tr}}{4\pi} \int_0^1 \int_0^{2\pi} \left(C_{L_{tr}} u_{r_{tr}} u_{n_{tr}} + C_{D0_{tr}} u_{t_{tr}}^2 \right) \cos(\Psi) \, \mathrm{d}\Psi \mathrm{d}\tau$$

$$
\begin{aligned}
\mathrm{f}_{Hx_{tr}} &= -\frac{1}{4}\rho\pi R_{tr}^4 n_{tr}^2 \Omega^2 \sigma_{tr} C_{D0_{tr}} u_{tail} \\
\mathbf{b}_{Hx_{tr}} &= -\frac{1}{4}\rho\pi R^4 n_{tr}^2 \Omega^2 \sigma_{tr} C_{L_{tr}} v_{tail} \begin{bmatrix} 0 \\ 0 \\ 0 \\ u_{tail} \end{bmatrix}^T \\
\mathrm{f}_{Hz_{tr}} &= -\frac{1}{4}\rho\pi R_{tr}^4 n_{tr}^2 \Omega^2 \sigma_{tr} C_{D0_{tr}} w_{tail} \\
\mathbf{b}_{Hz_{tr}} &= -\frac{1}{4}\rho\pi R_{tr}^4 n_{tr}^2 \Omega^2 \sigma_{tr} C_{L_{tr}} v_{tail} \begin{bmatrix} 0 \\ 0 \\ 0 \\ w_{tail} \end{bmatrix}^T
\end{aligned}
$$

In the next section, the forces and moments generated by the helicopter empennage are derived.

3.4 Empennage

The force and moment contribution of the empennage is due to the aerodynamic lift and drag generated by the vertical and horizontal tails, and the fuselage drag. The aerodynamic forces and moments of the vertical tail [17] are:

$$
\begin{aligned}
Y_{vt} &= \frac{1}{2}\rho S_{vt}\Big(C_{L_\alpha}^{vt} V_{vt}(v - v_{wind}) + v_{vt}^2\Big) \\
L_{vt} &= -Y_{vt} z_{vt} \\
N_{vt} &= Y_{vt} x_{vt}
\end{aligned}
\tag{3.33}
$$

where, $V_{vt} = \sqrt{(u - u_{wind})^2 + (w - w_{wind} + x_{vt}q - K_\lambda V_i)^2}$ and $v_{vt} = v - v_{wind} + x_{vt}r - V_{i_{tr}}$ are the axial and normal velocities of the vertical tail respectively.

The aerodynamic forces and moments of the horizontal tail are:

$$\begin{aligned} Z_{ht} &= \frac{1}{2}\rho S_{ht}\Big(C_{L_\alpha}^{ht}|u-u_{_{wind}}|w_{ht}+w_{ht}^2\Big) \\ M_{ht} &= -Z_{ht}x_{ht} \end{aligned} \tag{3.34}$$

where, $w_{ht} = w_{_{wind}} - x_{ht}q - K_\lambda V_i$ is the normal velocity of the horizontal tail.

The fuselage drag is:

$$\begin{aligned} X_{fus} &= -\frac{1}{2}\rho S_x^{fus} V_{fus}(u-u_{_{wind}}) \\ Y_{fus} &= -\frac{1}{2}\rho S_y^{fus} V_{fus}(v-v_{_{wind}}) \\ Z_{fus} &= -\frac{1}{2}\rho S_z^{fus} V_{fus}(w-w_{_{wind}}+V_i) \end{aligned} \tag{3.35}$$

where, $V_{fus} = \sqrt{(u-u_{_{wind}})^2+(v-v_{_{wind}})^2+(w-w_{_{wind}}+V_i)^2}$ is the dynamic pressure of the fuselage.

3.5 Combined Forces and Moments on Helicopter Fuselage

Combining the individual forces and moments of the main rotor, tail rotor and empennage results in the equations of the total forces and moments applied to the helicopter fuselage:

$$\mathbf{F} = \begin{bmatrix} X_{mr}+X_{fus} \\ Y_{mr}+Y_{tr}+Y_{vt}+Y_{fus} \\ Z_{mr}+Z_{ht}+Z_{fus} \end{bmatrix} + \mathbf{R}_b^{I^{-1}} \begin{bmatrix} 0 \\ 0 \\ mg \end{bmatrix} \tag{3.36}$$

$$\mathbf{M} = \begin{bmatrix} L_{mr}+L_{tr}+L_{vt} \\ M_{mr}+M_{tr}+M_{ht} \\ N_{mr}+N_{tr}+N_{vt} \end{bmatrix} \tag{3.37}$$

By substituting Eqs. (3.36) and (3.37) into (3.1) and (3.2), the nonlinear helicopter dynamics are:

$$\begin{aligned}
\dot{\mathbf{x}}_{10\times1} &= \mathbf{h(x,u)}_{10\times1} \\
\dot{\boldsymbol{\theta}} &= \boldsymbol{\Phi}(\boldsymbol{\theta})\ \boldsymbol{\omega} \\
\dot{\mathbf{p}} &= \mathbf{R}_b^I(\boldsymbol{\theta})\ \boldsymbol{\upsilon}
\end{aligned} \tag{3.38}$$

where $\mathbf{x} = [u\ v\ w\ p\ q\ r\ a_1\ b_1\ c_1\ d_1]^T$ are the states and $\mathbf{h(x,u)}$ is a nonlinear function of the states and inputs. This represents the non-affine-in-control 6-DOF dynamic model of the helicopter.

The helicopter dynamics represented by Eq. (3.38) are not suitable for most MIMO control approaches. To overcome this, a new formulation to represent the helicopter dynamics in an affine-in-control form is derived in the next section.

3.6 Affine-In-Control Model

To obtain a control-affine model of the helicopter dynamics, each term in Eqs. (3.36) and (3.37) must be decomposed into: an input-dependant component and an input-independent component. To do this, the algebraic equations of the longitudinal and lateral flapping angles are required.

The flapping dynamics of the main rotor is represented by two first-order differential Eqs. (3.6) and (3.7). To design a robust controller based on the nonlinear model of the helicopter dynamics, all the states, including the flapping angles must be observable. However, the direct measurement of the flapping angles is not available. To avoid the need for the state estimation of these states and since the time-constant of the main rotor, τ_f, is very small (Table 5.1), Eqs. (3.6) and (3.7) are approximated by calculating the rotor flapping in steady-state. In addition, the cross-coupling flapping derivatives A_b and B_a, which are

relatively small, are neglected to obtain a simpler control-oriented model. The simplified flapping dynamics of the rotor is:

$$a_1 = -\tau_f q + a_v + K_{lon}\delta_{lon} \tag{3.39}$$

$$b_1 = -\tau_f p + b_v + K_{lat}\delta_{lat} \tag{3.40}$$

where, $a_v = \frac{\partial a_1}{\partial \mu}\mu_x + \frac{\partial a_1}{\partial \mu_z}\mu_z$ and $b_v = \frac{\partial b_1}{\partial \mu_v}\mu_y$ are the longitudinal and lateral translational velocity contributions to the flapping of the main rotor. Note that the stabilizer bar acts as a lagged rate feedback which makes the zero-dynamics of the helicopter stable so its effect should not be cancelled by the controller. Similarly, a human pilot stabilizes the helicopter without compensating for the interactions of the stabilizer bar as it is designed to help a pilot to stabilize the helicopter. Thus, the stabilizer bar dynamics are eliminated in Eqs. (3.39) and (3.40), for later use in the control design in Chapter 6. By using Eqs. (3.39) and (3.40) when designing the controller, the controller will not compensate for the stabilizing effect of the flybar inputs.

Using the algebraic equations of the flapping angles, Eqs. (3.39) and (3.40), a control-affine model of the helicopter dynamics can be obtained. By substituting Eqs. (3.18) and (3.39) into (3.12) and assuming small flapping angles due to the stiff rotor hub assembly, the force of the main rotor along the longitudinal axis is:

$$\begin{aligned} X_{mr} &= -(\mathrm{f}_{_T} + \mathbf{b_T}\mathbf{u})a_1 \\ &= \overbrace{(\tau_f q - a_v)\mathrm{f}_{_T}}^{\mathrm{f}_{X_{mr}}} + K_{lon}\delta_{lon}\mathbf{b_T}\mathbf{u} + \underbrace{\Big((\tau_f q - a_v)\mathbf{b_T} - [0\ 0\ K_{lon}\mathrm{f}_{_T}\ 0]\Big)}_{\mathbf{b_{X_{mr}}}}\ \mathbf{u} \\ &= \mathrm{f}_{_{X_{mr}}} + \mathbf{b_{X_{mr}}}\mathbf{u} \end{aligned} \tag{3.41}$$

The term $K_{lon}\delta_{lon}\mathbf{b_T}\mathbf{u}$ in Eq. (3.41) is relatively small and is neglected. Also, the in-plane forces of the main and tail rotor, $H_{x_{mr}}$, $H_{y_{mr}}$, $H_{x_{tr}}$ and $H_{z_{tr}}$, are relatively small for small-scale helicopters and are therefore neglected in subsequent calculations.

Substituting Eqs. (3.18), (3.39) and (3.40) into (3.14), all components of the main rotor can be found in a control-affine form as:

$$
\begin{aligned}
X_{mr} &= (\tau_f q - a_v)\mathrm{f}_T + \Big((\tau_f q - a_v)\mathbf{b_T} - [0\ 0\ K_{lon}\mathrm{f}_T\ 0]\Big)\mathbf{u} \\
Y_{mr} &= (-\tau_f p + b_v)\mathrm{f}_T + \Big((-\tau_f p + b_v)\mathbf{b_T} + [0\ K_{lat}\mathrm{f}_T\ 0\ 0]\Big)\mathbf{u} \\
Z_{mr} &= -\mathrm{f}_T - \mathbf{b_T}\mathbf{u} \\
L_{mr} &= (-\tau_f p + b_v)(K_\beta - \mathrm{f}_T z_{cg}) + \Big(z_{cg}(\tau_f p - b_v)\mathbf{b_T} + \big[0\ K_{lat}(K_\beta - \mathrm{f}_T z_{cg})\ 0\ 0\big]\Big)\mathbf{u} \\
M_{mr} &= (-\tau_f q + a_v)(K_\beta - \mathrm{f}_T z_{cg}) + \Big(z_{cg}(\tau_f q - a_v)\mathbf{b_T} + \big[0\ 0\ K_{lon}(K_\beta - \mathrm{f}_T z_{cg})\ 0\big]\Big)\mathbf{u} \\
N_{mr} &= \mathrm{f}_Q + \mathbf{b_Q}\mathbf{u}
\end{aligned}
\tag{3.42}
$$

Similarly, components of the tail rotor are:

$$
\begin{aligned}
Y_{tr} &= \mathrm{f}_{T_{tr}} + \mathbf{b_{T_{tr}}}\mathbf{u} \\
L_{tr} &= -z_{fus}\mathrm{f}_{T_{tr}} - z_{fus}\mathbf{b_{T_{tr}}}\mathbf{u} \\
M_{tr} &= \mathrm{f}_{Q_{tr}} + \mathbf{b_{Q_{tr}}}\mathbf{u} \\
N_{tr} &= x_{fus}\mathrm{f}_{T_{tr}} + x_{fus}\mathbf{b_{T_{tr}}}\mathbf{u}
\end{aligned}
\tag{3.43}
$$

Substituting Eqs. (3.42) and (3.43) into (3.36) and (3.37) and rearranging results in:

$$\mathbf{F} = \mathbf{F_0} + \mathbf{F_u}\mathbf{u} \tag{3.44}$$

$$\mathbf{M} = \mathbf{M_0} + \mathbf{M_u}\mathbf{u} \tag{3.45}$$

where $\mathbf{F_0}$ and $\mathbf{M_0}$ are the input-independent force and moment vectors as:

$$\mathbf{F_0} = \begin{bmatrix} \mathrm{f}_{X_{mr}} + X_{fus} \\ \mathrm{f}_{Y_{mr}} + \mathrm{f}_{Y_{tr}} + Y_{vt} + Y_{fus} \\ \mathrm{f}_{Z_{mr}} + Z_{ht} + Z_{fus} \end{bmatrix} + \mathbf{R}_b^{I^{-1}} \begin{bmatrix} 0 \\ 0 \\ mg \end{bmatrix}$$
$$\mathbf{M_0} = \begin{bmatrix} \mathrm{f}_{L_{mr}} + \mathrm{f}_{L_{tr}} + L_{vt} \\ \mathrm{f}_{M_{mr}} + \mathrm{f}_{M_{tr}} + M_{ht} \\ \mathrm{f}_{N_{mr}} + \mathrm{f}_{N_{tr}} + N_{vt} \end{bmatrix} \tag{3.46}$$

and $\mathbf{M_u}$ and $\mathbf{F_u}$ are the input-dependent matrices given by:

$$\mathbf{F_u} = \begin{bmatrix} \mathbf{b_{X_{mr}}} \\ \mathbf{b_{Y_{mr}}} + \mathbf{b_{Y_{tr}}} \\ \mathbf{b_{Z_{mr}}} \end{bmatrix}, \quad \mathbf{M_u} = \begin{bmatrix} \mathbf{b_{L_{mr}}} + \mathbf{b_{L_{tr}}} \\ \mathbf{b_{M_{mr}}} + \mathbf{b_{M_{tr}}} \\ \mathbf{b_{N_{mr}}} + \mathbf{b_{N_{tr}}} \end{bmatrix} \tag{3.47}$$

where, $\mathrm{f}_{(.)}$ are the input-independent, and $\mathbf{b}_{(.)}$ are the input-dependent components in Eqs. (3.46) and (3.47).

Substituting Eqs. (3.44) to (3.47) into (3.1) and (3.2) results in:

$$\underbrace{\begin{bmatrix} \dot{\mathbf{v}} \\ \hline \dot{\boldsymbol{\omega}} \end{bmatrix}}_{\dot{\mathbf{x}}_{6\times1}} = \underbrace{\begin{bmatrix} \frac{\mathbf{F_0}}{m} - \boldsymbol{\omega} \times \mathbf{v} \\ \hline \mathbf{I}^{-1}(\mathbf{M_0} - \boldsymbol{\omega} \times \mathbf{I}\,\boldsymbol{\omega}) \end{bmatrix}}_{\mathbf{f(x)}_{6\times1}} + \underbrace{\begin{bmatrix} \frac{\mathbf{F_u}}{m} \\ \hline \mathbf{I}^{-1}\mathbf{M_u} \end{bmatrix}}_{\mathbf{b(x)}_{6\times4}} \mathbf{u} \tag{3.48}$$

The helicopter dynamics are written in the control-affine form by rewriting Eq. (3.48) as:

$$\begin{aligned} \dot{\mathbf{x}}_{6\times1} &= \mathbf{f(x)}_{6\times1} + \mathbf{b(x)}_{6\times4}\mathbf{u}_{4\times1} \\ \dot{\boldsymbol{\theta}} &= \boldsymbol{\Phi}(\boldsymbol{\theta})\,\boldsymbol{\omega} \\ \dot{\mathbf{p}} &= \boldsymbol{R}_b^I(\boldsymbol{\theta})\,\boldsymbol{\upsilon} \end{aligned} \tag{3.49}$$

where $\mathbf{x} = [u\ v\ w\ p\ q\ r]^T$, $\mathbf{f(x)}$ is the state function and includes the nonlinear centrifugal and coriolis terms and $\mathbf{b(x)}$ is the control gain matrix. The augmented vector $\boldsymbol{q} = [\mathbf{x}\ \boldsymbol{\theta}\ \mathbf{p}]^T$ is defined as the observable state vector of the system.

Equation (3.49) represents the affine-in-control (linear with respect to the control inputs) and non-iterative 6-DOF dynamic model of the helicopter such that the system matrices are only state-dependent.

3.7 Square Affine-In-Control Formulation using the Control Point Approach

The control-affine model of the helicopter obtained in Eq. (3.49) is not in square form as it has four inputs and six outputs. This is due to the underactuated nature of helicopters, which also makes the control design very challenging.

In order to solve this problem, the control point approach is used [43]. The control point CP, is an imaginary point on the main rotor axis at a fixed distance d, above the CG as shown in Figure 3.1. Controlling the position of this point and the yaw angle of the helicopter still results in the stabilized motion of the helicopter. This is due to the fact that the underactuated DOFs of the helicopter are inherently stable when a stabilizer bar is used and in the presence of a feedback controller for the position tracking of the CP [43]. In fact, the attitude rate feedback characteristics of the stabilizer bar results in the stable zero-dynamics of the system. Only four control outputs: x_{cp}, y_{cp}, z_{cp} and ψ are now needed (instead of six variables, i.e. the position of the CG and Euler angles of the helicopter).

Using the three-dimensional position of a point at a fixed distance d, above the CG in the control output, enables the controller to react to the disturbances in the roll and pitch DOFs which provides better stability for the closed-loop system.

To transform Eq. (3.49) into a square form with equal number of inputs and outputs, the acceleration of the control point in the inertial frame is calculated as,

$$\ddot{\boldsymbol{x}}_{\boldsymbol{cp}} = \mathbf{R}_b^I \Big(\dot{\boldsymbol{v}} + \boldsymbol{\omega} \times \boldsymbol{v} + \boldsymbol{\omega} \times (\boldsymbol{\omega} \times \boldsymbol{d}_{\boldsymbol{cp}}) + \dot{\boldsymbol{\omega}} \times \boldsymbol{d}_{\boldsymbol{cp}} \Big) \tag{3.50}$$

where $\boldsymbol{x}_{\boldsymbol{cp}} = [x_{cp}\ y_{cp}\ z_{cp}]^T$ and $\boldsymbol{d}_{\boldsymbol{cp}} = [0\ 0\ \text{-d}]^T$. By substituting Eq. (3.48) into (3.50), the control point acceleration is:

$$\ddot{\boldsymbol{x}}_{\boldsymbol{cp}} = \boldsymbol{f_1} + \boldsymbol{b_1}\mathbf{u} \tag{3.51}$$

where,

$$\boldsymbol{f_1} = \frac{\boldsymbol{F_g}}{m} + \mathbf{R}_b^I \Big(\boldsymbol{\omega} \times (\boldsymbol{\omega} \times \boldsymbol{d}_{\boldsymbol{cp}}) + m\boldsymbol{F_0} + \mathbf{D}(\boldsymbol{I}^{-1}\boldsymbol{M_0} - \boldsymbol{I}^{-1}\boldsymbol{\omega} \times \boldsymbol{I}\ \boldsymbol{\omega}) \Big)$$

$$\boldsymbol{b_1} = \mathbf{R}_b^I \left(\frac{\boldsymbol{F_u}}{m} + \mathbf{D}\boldsymbol{I}^{-1}\boldsymbol{M_u} \right)$$

$$\mathbf{D} = \begin{bmatrix} 0 & -\text{d} & 0 \\ \text{d} & 0 & 0 \\ 0 & 0 & 0 \end{bmatrix}, \quad \boldsymbol{F_g} = \begin{bmatrix} 0 \\ 0 \\ mg \end{bmatrix}$$

Similarly, the angular acceleration of the helicopter around the yaw axis is:

$$\ddot{\psi} = f_2 + \boldsymbol{b_2}\mathbf{u} \tag{3.52}$$

where,

$$f_2 = \boldsymbol{f_s}\Big(\boldsymbol{I^{-1}M_0} - \boldsymbol{I^{-1}\omega} \times \mathbf{I}\,\boldsymbol{\omega}\Big) + f_q q + f_r r$$

$$\boldsymbol{b_2} = \boldsymbol{f_s I^{-1} M_u}$$

and,

$$f_q = \dot{\phi}\cos\phi\sec\theta + \dot{\theta}\sin\phi\tan\theta\sec\theta$$
$$f_r = -\dot{\phi}\sin\phi\sec\theta + \dot{\theta}\cos\phi\tan\theta\sec\theta$$
$$\boldsymbol{f_s} = [0 \quad \sec\theta\sin\phi \quad \sec\theta\cos\phi]$$

Finally, by combining Eqs. (3.51) and (3.52), the square control-affine input-output formulation of the helicopter dynamics is:

$$\ddot{\mathbf{y}}_{4\times1} = \mathbf{g}(\boldsymbol{y}, \dot{\boldsymbol{y}})_{4\times1} + \mathbf{c}(\boldsymbol{y}, \dot{\boldsymbol{y}})_{4\times4}\mathbf{u}_{4\times1} \tag{3.53}$$

where,

$$\mathbf{y} = \left[\frac{\boldsymbol{x_{cp}}_{3\times1}}{\psi}\right], \quad \mathbf{g}(\boldsymbol{y}, \dot{\boldsymbol{y}}) = \left[\frac{\boldsymbol{f_1}_{3\times1}}{f_2}\right], \quad \mathbf{c}(\boldsymbol{y}, \dot{\boldsymbol{y}}) = \left[\frac{\boldsymbol{b_1}_{3\times4}}{\boldsymbol{b_2}_{1\times4}}\right]$$

This formulation relates the four control inputs to the four control outputs, i.e. the three components of the control point position and the yaw angle of the helicopter.

Therefore, Eq. (3.53) represents a non-iterative control-oriented model of the helicopter dynamics in the control-affine and square form. This form is suitable for the application of a wide range of nonlinear MIMO control approaches in the

control design for small-scale helicopters.

3.8 Rotational Dynamics Using the First-Principles Approach

The hybrid model approach, in which the rotor is explicitly modeled and then coupled to the fuselage equations of motion through rotor flapping spring derivatives, is used in section 3.2 to obtain the rotational dynamics of the helicopter. In this section, an alternative method is used to obtain the rotational dynamics of the helicopter using the first-principles approach based on blade element and momentum theories. The angular momentum of the main rotor, which is often ignored due to its complexity, is considered in the fuselage equations of motion. To do this, the angular momentum of the combined fuselage and rotor system is calculated and the modified equations of motion of the fuselage are derived. The roll and pitch moments are then derived using the blade element and momentum theories and an alternate control-affine formulation of the helicopter dynamics is obtained again.

To obtain the rotational dynamics of the helicopter, the angular momentum of the combined fuselage and rotor system is calculated. Since most small-scale helicopters have a hingeless and stiff rotor hub assembly, the rotor is assumed to be rigid and the momentum effects due to the flapping are neglected. The main blades are assumed to have a symmetrical airfoil for which the moment required to twist the blade around its feathering axis (spanwise r-axis in Figure 3.3) is negligible, so the momentum effects due to the feathering are also neglected. A top view of the main rotor is shown in Figure 3.3, and the total angular momentum of the combined fuselage and main rotor system is:

$$\mathbf{H}_{_{CG}} = \mathbf{I}\boldsymbol{\omega} + \mathbf{R}^{b}_{rpn}\mathbf{H}_{r} + \boldsymbol{L}_{\boldsymbol{CG}} \times m(\boldsymbol{v} + \boldsymbol{\omega} \times \boldsymbol{L}_{\boldsymbol{CG}}) \tag{3.54}$$

where $\boldsymbol{L_{CG}} = [0\ 0\ z_{cg}]^T$ is the vector of the main rotor hub offset from the CG, $\mathbf{R}^b_{rpn}$ is the rotation matrix from the blade $\{rpn\}$ to the body $\{B\}$ coordinates, inverse of which is given in Eq. (3.16), and $\mathbf{H}_r$ is the angular momentum of the main rotor in the $\{rpn\}$ coordinates represented as:

$$\mathbf{H}_r = \mathbf{I}_r \boldsymbol{\omega_{rpn}} \tag{3.55}$$

$$\boldsymbol{\omega_{rpn}} = \mathbf{R}^{rpn}_b \boldsymbol{\omega_r} \tag{3.56}$$

$$\boldsymbol{\omega_r} = \boldsymbol{\omega} + \boldsymbol{\Omega} \tag{3.57}$$

where $\boldsymbol{\Omega} = [0\ 0\ \Omega]^T$ and $\mathbf{I}_r = \text{diag}_{3\times3}(I_r, I_p, I_n)$ in which the off-diagonal terms are ignored. The main rotor speed Ω, is assumed to be constant throughout this analysis.

The last term appeared in Eq. (3.54) is due to the small vertical offset of the main rotor hub from the CG. Since the product of the offset and the rotor mass is very small this term is neglected. Using the Newton-Euler method, the total moment vector acting on the helicopter is:

$$\mathbf{M} = \frac{d\mathbf{H}_{CG}}{dt} = \dot{\mathbf{H}}_{CG} + \boldsymbol{\omega} \times \mathbf{H}_{CG} \tag{3.58}$$

Using $\dot{\mathbf{R}}^b_{rpn}\mathbf{H}_r = \boldsymbol{\Omega} \times (\mathbf{R}^b_{rpn}\mathbf{H}_r)$ and substituting Eqs. (3.54) to (3.57) into (3.58) results in:

$$\begin{aligned}\mathbf{M}(\Psi) &= \mathbf{I}\dot{\boldsymbol{\omega}} + \dot{\mathbf{R}}^b_{rpn}\mathbf{H}_r + \mathbf{R}^b_{rpn}\dot{\mathbf{H}}_r + \boldsymbol{\omega} \times (\mathbf{I}\boldsymbol{\omega} + \mathbf{R}^b_{rpn}\mathbf{H}_r) \\ &= \mathbf{I}\dot{\boldsymbol{\omega}} + \boldsymbol{\omega} \times \mathbf{I}\boldsymbol{\omega} + \mathbf{M}_r(\Psi)\end{aligned} \tag{3.59}$$

where,

$$\mathbf{M}_r(\Psi) = \mathbf{R}^b_{rpn}\mathbf{I}_r\mathbf{R}^{rpn}_b\dot{\boldsymbol{\omega}}_{\boldsymbol{r}} + \boldsymbol{\omega_r} \times \left(\mathbf{R}^b_{rpn}\mathbf{I}_r\mathbf{R}^{rpn}_b\boldsymbol{\omega_r}\right) - \mathbf{R}^b_{rpn}\mathbf{I}_r\left(\boldsymbol{\Omega} \times (\mathbf{R}^{rpn}_b\boldsymbol{\omega_r})\right) \tag{3.60}$$

The terms $\mathbf{I}\dot{\boldsymbol{\omega}} + \boldsymbol{\omega} \times \mathbf{I}\boldsymbol{\omega}$ in Eq. (3.59) correspond to the changes in the angular momentum of the fuselage. The new term $\mathbf{M}_r(\Psi)$, represents the moment corresponding to the changes in the angular momentum of the main rotor which varies with the rotor azimuth angle Ψ. This term is often absent in the fuselage equations of motion in the literature [10, 14, 21, 22, 23, 24, 26, 27].

To obtain the equations of motion of the fuselage independent of Ψ, an equivalent TPP rotor disk model is considered for the rotating blades by averaging $\mathbf{M}_r(\Psi)$ around Ψ as:

$$\begin{aligned}\mathbf{M}_r &= \frac{1}{2\pi}\int_0^{2\pi} \mathbf{M}_r(\Psi) \\ &= \frac{1}{2\pi}\int_0^{2\pi} \Big[\mathbf{R}^b_{rpn}\mathbf{I}_r\mathbf{R}^{rpn}_b\dot{\boldsymbol{\omega}}_{\boldsymbol{r}} + \boldsymbol{\omega}_{\boldsymbol{r}} \times \big(\mathbf{R}^b_{rpn}\mathbf{I}_r\mathbf{R}^{rpn}_b\boldsymbol{\omega}_{\boldsymbol{r}}\big) - \\ &- \mathbf{R}^b_{rpn}\mathbf{I}_r\big(\boldsymbol{\Omega} \times (\mathbf{R}^{rpn}_b\boldsymbol{\omega}_{\boldsymbol{r}})\big)\Big]\,\mathrm{d}\Psi \end{aligned} \tag{3.61}$$

Manipulation of Eq. (3.61) results in:

$$\mathbf{M}_r = \mathbf{I}_s\dot{\boldsymbol{\omega}} + \boldsymbol{\omega} \times \mathbf{I}_s\boldsymbol{\omega} + \boldsymbol{\omega} \times \mathbf{I}_r\boldsymbol{\Omega} \tag{3.62}$$

where $\mathbf{I}_s$ is the equivalent moment of inertia tensor of the TPP rotor disk model defined as:

$$\mathbf{I}_s = \frac{1}{2\pi}\int_0^{2\pi} \mathbf{R}^b_{rpn}\mathbf{I}_r\mathbf{R}^{rpn}_b\,\mathrm{d}\Psi = \begin{bmatrix} \frac{I_P+I_r}{2} & 0 & 0 \\ 0 & \frac{I_P+I_r}{2} & 0 \\ 0 & 0 & I_n \end{bmatrix} \tag{3.63}$$

Substituting Eq. (3.62) into (3.59) results in:

$$\mathbf{M} = (\mathbf{I} + \mathbf{I}_s)\dot{\boldsymbol{\omega}} + \boldsymbol{\omega} \times \big((\mathbf{I} + \mathbf{I}_s)\boldsymbol{\omega} + \mathbf{I}_r\boldsymbol{\Omega}\big) \tag{3.64}$$

Introducing an effective moment of inertia tensor $\mathbf{I}_e = \mathbf{I} + \mathbf{I}_s$ and rearranging Eq. (3.64) results in the modified equations of motion of the fuselage as:

$$\dot{\boldsymbol{\omega}} = \mathbf{I}_e^{-1}\mathbf{M} - \mathbf{I}_e^{-1}(\boldsymbol{\omega} \times \mathbf{I}_e\boldsymbol{\omega}) - \mathbf{I}_e^{-1}(\boldsymbol{\omega} \times \mathbf{I}_r\boldsymbol{\Omega}) \tag{3.65}$$

3.8.1 Gyroscopic Effect of Main Rotor

Incorporating the angular momentum of the main rotor in the equations of motion of the fuselage allows for a better understanding of how a helicopter reacts to the applied moments and external disturbances. In fact, the term $\boldsymbol{\omega} \times \mathbf{I}_r\boldsymbol{\Omega}$ in Eq. (3.65) represents the gyroscopic effect of the main rotor which results in a 90 deg phase shift in the attitude response to the moments applied to the helicopter and increases the vehicle's resistance to the external disturbances by maintaining its orientation.

The gyroscopic effect of main rotor has significant effects on the roll and pitch responses of the helicopter as shown in Figures 3.6 and 3.7, which are obtained from the simulations of the Evolution-EX helicopter subject to the external moments.

The parameters of the Evolution-EX model are summarized in Table 5.1. The attitude response of the helicopter to a 15 Nm disturbance moment around the roll axis of the fuselage is shown in Figure 3.6 for the Evolution-EX helicopter with a counter clockwise rotor indicating that with the rotor gyroscopic effect present in the equations of motion as in Eq. (3.65), the helicopter precesses around the negative pitch axis due to the 90 deg phase shift caused by the gyroscopic effect. However, without including the gyroscopic effect of the rotor in the fuselage equations of motion, the vehicle tilts around the roll axis which is the opposite to the actual rotation of the helicopter and it settles about 10 deg greater in

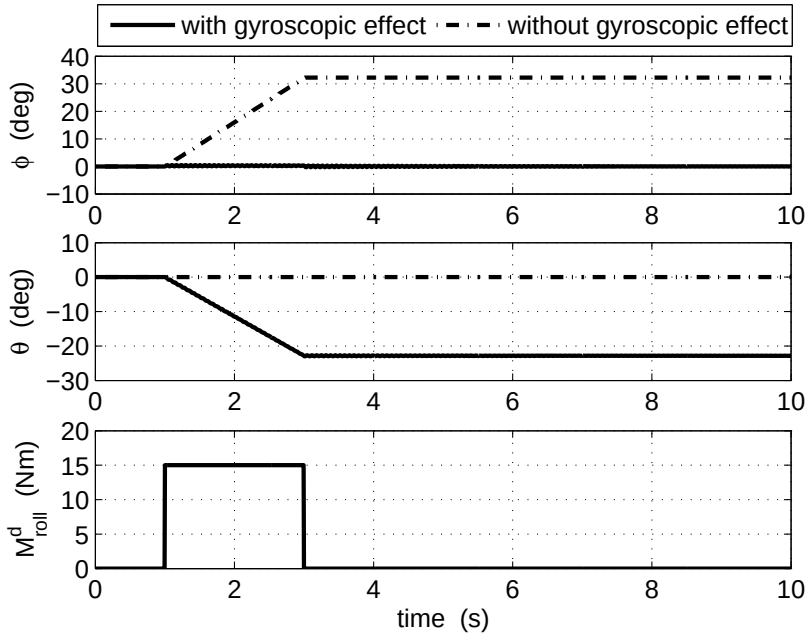

Figure 3.6: Gyroscopic effect on the attitude response to a 15 Nm roll disturbance moment ($\Omega = 1100$ rpm).

magnitude than the case in which the gyroscopic effect is included.

The attitude response of the helicopter to a 15 N m disturbance moment around the pitch axis of the fuselage is shown in Figure 3.7, which indicates that the helicopter precesses around the roll axis with the rotor gyroscopic effect included. However, without including the gyroscopic effect, the vehicle tilts around the pitch axis which is the opposite to the actual behavior of the helicopter and settles about 10 deg greater than the case in which the gyroscopic effect is included.

Note that in the hybrid model approach, the gyroscopic effect is not explicitly included in the rotor dynamics. Instead, the flapping equations (3.6) and (3.7) are derived such that this effect is implicitly considered. For example, the longitudinal command δ_{lon} in Eq. (3.6) generates a moment around the x-axis of the fuselage shown in Figure 3.2, but results in a longitudinal flapping angle "a_1" around the y-axis of the fuselage which is due to the gyroscopic effect of the

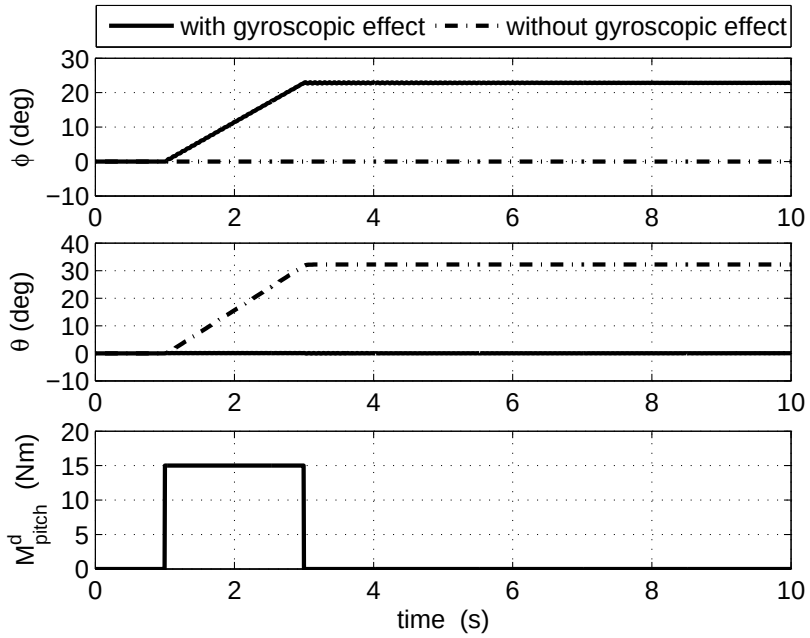

Figure 3.7: Gyroscopic effect on the attitude response to a 15 Nm pitch disturbance moment ($\Omega = 1100$ rpm).

rotor.

3.8.2 Roll and Pitch Moments using First-Principles

An alternative way of calculating the induced roll and pitch moments on the helicopter fuselage is by using the first-principles approach. The longitudinal and lateral cyclic commands cause the helicopter to pitch and roll by generating more lift on one side of the main rotor than the other. The new roll and pitch moments derived using the blade element and momentum theories are:

$$\tilde{M}_{roll} = \rho\pi R_{mr}^5 \Omega^2 C_{M_\phi} = \mathrm{f}_\phi + \mathbf{b}_\phi \mathbf{u} \tag{3.66}$$

$$\tilde{M}_{pitch} = \rho\pi R_{mr}^5 \Omega^2 C_{M_\theta} = \mathrm{f}_\theta + \mathbf{b}_\theta \mathbf{u} \tag{3.67}$$

where,

$$C_{M_\phi} = -\frac{\sigma_{mr}}{4\pi}\int_0^1\int_0^{2\pi} C_{L_\alpha}\Big(\theta - \frac{u_n}{u_p}\Big)u_p^2\sin(\Psi)\tau_{mr}\,\mathrm{d}\Psi\mathrm{d}\tau_{mr}$$
$$C_{M_\theta} = \frac{\sigma_{mr}}{4\pi}\int_0^1\int_0^{2\pi} C_{L_\alpha}\Big(\theta - \frac{u_n}{u_p}\Big)u_p^2\cos(\Psi)\tau_{mr}\,\mathrm{d}\Psi\mathrm{d}\tau_{mr}$$

and,

$$\begin{aligned}
\mathrm{f}_\phi &= \frac{1}{8}\rho\pi R_{mr}^5\Omega^2\sigma_{mr}C_{L_\alpha}\mu_x(\lambda_0-\mu_z)\\
\mathbf{b}_\phi &= \frac{1}{12}\rho\pi R_{mr}^5\Omega^2\sigma_{mr}C_{L_\alpha}\begin{bmatrix} -2\mu_x \\ \frac{3}{4}\mu_x\mu_y \\ -\frac{3}{8}(\mu_y^2+3\mu_x^2+2) \\ 0\end{bmatrix}^T
\end{aligned} \tag{3.68}$$

$$\begin{aligned}
\mathrm{f}_\theta &= \frac{1}{8}\rho\pi R_{mr}^5\Omega^2\sigma_{mr}C_{L_\alpha}\mu_y(\lambda_0-\mu_z)\\
\mathbf{b}_\theta &= \frac{1}{12}\rho\pi R_{mr}^5\Omega^2\sigma_{mr}C_{L_\alpha}\begin{bmatrix} -2\mu_y \\ \frac{3}{8}(\mu_x^2+3\mu_y^2+2) \\ -\frac{3}{4}\mu_x\mu_y \\ 0\end{bmatrix}^T
\end{aligned} \tag{3.69}$$

The new roll and pitch moments applied on the fuselage are:

$$\tilde{L}_{mr} = \tilde{M}_{roll} + L_S \tag{3.70}$$
$$\tilde{M}_{mr} = \tilde{M}_{pitch} + M_S \tag{3.71}$$

where $\tilde{M}_{roll}$ and $\tilde{M}_{pitch}$ are obtained from Eqs. (3.66) and (3.67) and L_S and M_S are the stabilizer moment contributions to the roll and pitch moments applied on the fuselage. The stabilizer bar acts as an attitude rate feedback as well as a secondary input to cyclic pitch command through the Bell-Hiller mixer shown in

Figure 4.2, and is modeled as [46],

$$L_S = \alpha_1 \dot{\theta} - \alpha_2 \delta_{lon} = \mathrm{f}_{\mathbf{S_x}} + \mathbf{b}_{\mathbf{S_x}} \mathbf{u} \tag{3.72}$$

$$M_S = -\alpha_1 \dot{\phi} + \alpha_2 \delta_{lat} = \mathrm{f}_{\mathbf{S_y}} + \mathbf{b}_{\mathbf{S_y}} \mathbf{u} \tag{3.73}$$

where $\dot{\theta}$ and $\dot{\phi}$ are calculated using Eq. (3.3) and the input-independent and input-dependent components are:

$$\mathrm{f}_{\mathbf{S_x}} = \alpha_1 \dot{\theta}, \quad \mathbf{b}_{\mathbf{S_x}} = -[0 \ 0 \ \alpha_2 \ 0] \tag{3.74}$$

$$\mathrm{f}_{\mathbf{S_y}} = -\alpha_1 \dot{\phi}, \quad \mathbf{b}_{\mathbf{S_y}} = [0 \ \alpha_2 \ 0 \ 0] \tag{3.75}$$

where α_1 and α_2 are the rate and input derivatives of the stabilizer bar and are obtained using a system identification method described in Chapter 5.

By substituting Eqs. (3.70) and (3.71) into Eq. (3.14), the modified total forces and moments applied on the fuselage are:

$$\mathbf{F} = \begin{bmatrix} X_{mr} + X_{fus} \\ Y_{mr} + Y_{tr} + Y_{vt} + Y_{fus} \\ Z_{mr} + Z_{ht} + Z_{fus} \end{bmatrix} + \mathbf{R}_b^{I^{-1}} \begin{bmatrix} 0 \\ 0 \\ mg \end{bmatrix} \tag{3.76}$$

$$\tilde{\mathbf{M}} = \begin{bmatrix} \tilde{L}_{mr} + L_{tr} + L_{vt} \\ \tilde{M}_{mr} + M_{tr} + M_{ht} \\ N_{mr} + N_{tr} + N_{vt} \end{bmatrix} \tag{3.77}$$

By substituting Eqs. (3.76) and (3.77) into (3.1) and (3.2), the nonlinear

helicopter dynamics are:

$$\begin{aligned}
\dot{\mathbf{x}}_{6\times1} &= \tilde{\mathbf{h}}(\mathbf{x},\mathbf{u})_{6\times1} \\
\dot{\boldsymbol{\theta}} &= \boldsymbol{\Phi}(\boldsymbol{\theta})\ \boldsymbol{\omega} \\
\dot{\mathbf{p}} &= \mathbf{R}_b^I(\boldsymbol{\theta})\ \boldsymbol{\upsilon}
\end{aligned} \tag{3.78}$$

where $\mathbf{x} = [u\ v\ w\ p\ q\ r]^T$, and $\tilde{\mathbf{h}}(\mathbf{x},\mathbf{u})$ is a new nonlinear function of the states and inputs.

By rearranging Eqs. (3.76) and (3.77) and neglecting the rate feedback terms of the stabilizer bar, $\mathrm{f}_{\mathbf{S_x}}$ and $\mathrm{f}_{\mathbf{S_y}}$, which provide the zero-dynamics stability as described earlier, the modified input-independent force and moment vectors are:

$$\begin{aligned}
\tilde{\mathbf{F}}_{\mathbf{0}} &= \begin{bmatrix} X_{fus} \\ \mathrm{f}_{Y_{tr}} + Y_{vt} + Y_{fus} \\ \mathrm{f}_{Z_{mr}} + Z_{ht} + Z_{fus} \end{bmatrix} + \mathbf{R}_b^{I^{-1}} \begin{bmatrix} 0 \\ 0 \\ mg \end{bmatrix} \\
\tilde{\mathbf{M}}_{\mathbf{0}} &= \begin{bmatrix} \mathrm{f}_{\phi} + \mathrm{f}_{\mathbf{S_x}} + \mathrm{f}_{L_{tr}} + L_{vt} \\ \mathrm{f}_{\theta} + \mathrm{f}_{\mathbf{S_y}} + \mathrm{f}_{M_{tr}} + M_{ht} \\ \mathrm{f}_{N_{mr}} + \mathrm{f}_{N_{tr}} + N_{vt} \end{bmatrix}
\end{aligned} \tag{3.79}$$

and the modified input-dependent matrices are:

$$\tilde{\mathbf{F}}_{\mathbf{u}} = \begin{bmatrix} 0 \\ \mathbf{b}_{\mathbf{Y_{tr}}} \\ \mathbf{b}_{\mathbf{Z_{mr}}} \end{bmatrix}, \quad \tilde{\mathbf{M}}_{\mathbf{u}} = \begin{bmatrix} \mathbf{b}_{\phi} + \mathbf{b}_{\mathbf{S_x}} + \mathbf{b}_{\mathbf{L_{tr}}} \\ \mathbf{b}_{\theta} + \mathbf{b}_{\mathbf{S_y}} + \mathbf{b}_{\mathbf{M_{tr}}} \\ \mathbf{b}_{\mathbf{N_{mr}}} + \mathbf{b}_{\mathbf{N_{tr}}} \end{bmatrix} \tag{3.80}$$

where f_{ϕ}, $\mathbf{b}_{\phi}$, f_{θ}, $\mathbf{b}_{\theta}$ are found from Eqs. (3.68) and (3.69) and $\mathrm{f}_{\mathbf{S_x}}$, $\mathbf{b}_{\mathbf{S_x}}$, $\mathrm{f}_{\mathbf{S_y}}$, $\mathbf{b}_{\mathbf{S_x}}$ are found from Eqs. (3.74) and (3.75) and the rest of the terms are found in the previous sections.

By combining the Eqs. (3.79) and (3.80), the total forces and moments are:

$$\tilde{\mathbf{F}} = \tilde{\mathbf{F}}_{\mathbf{0}} + \tilde{\mathbf{F}}_{\mathbf{u}}\mathbf{u} \tag{3.81}$$

$$\tilde{\mathbf{M}} = \tilde{\mathbf{M}}_{\mathbf{0}} + \tilde{\mathbf{M}}_{\mathbf{u}}\mathbf{u} \tag{3.82}$$

Substituting Eqs. (3.81) and (3.82) into (3.1) and (3.2) results in:

$$\underbrace{\begin{bmatrix} \dot{\mathbf{v}} \\ \hline \dot{\boldsymbol{\omega}} \end{bmatrix}}_{\dot{\mathbf{x}}_{6\times1}} = \underbrace{\begin{bmatrix} \frac{\tilde{\mathbf{F}}_{\mathbf{0}}}{m} - \boldsymbol{\omega}\times\mathbf{v} \\ \hline \mathbf{I}^{-1}(\tilde{\mathbf{M}}_{\mathbf{0}} - \boldsymbol{\omega}\times\mathbf{I}\,\boldsymbol{\omega}) \end{bmatrix}}_{\tilde{\mathbf{f}}(\mathbf{x})_{6\times1}} + \underbrace{\begin{bmatrix} \frac{\tilde{\mathbf{F}}_{\mathbf{u}}}{m} \\ \hline \mathbf{I}^{-1}\tilde{\mathbf{M}}_{\mathbf{u}} \end{bmatrix}}_{\tilde{\mathbf{b}}(\mathbf{x})_{6\times4}}\mathbf{u} \tag{3.83}$$

The helicopter dynamics are derived in the control-affine form again by rewriting Eq. (3.83) as:

$$\begin{aligned} \dot{\mathbf{x}}_{6\times1} &= \tilde{\mathbf{f}}(\mathbf{x})_{6\times1} + \tilde{\mathbf{b}}(\mathbf{x})_{6\times4}\mathbf{u}_{4\times1} \\ \dot{\boldsymbol{\theta}} &= \boldsymbol{\Phi}(\boldsymbol{\theta})\,\boldsymbol{\omega} \\ \dot{\mathbf{p}} &= \mathbf{R}_b^I(\boldsymbol{\theta})\,\boldsymbol{\upsilon} \end{aligned} \tag{3.84}$$

The helicopter dynamics obtained using the first-principles approach in Eq. (3.78) is simpler and has fewer rotor dynamic parameters (α_1 and α_2) compared to the one obtained using the hybrid model approach (K_β, K_{lon}, K_{lat}, τ_f, τ_s, A_b, B_A and K_s) in Eq. (3.38), so its system identification is easier. However, neglecting the momentum effects due to the rotor flapping in Eq. (3.78), results in less accuracy. These two models of the rotational dynamics in Eqs. (3.38) and (3.78) will be compared in more details using the flight test data in Section 5.4 in Chapter 5.

3.9 Summary

A new control-oriented model in an affine-in-control and square input-output formulation has been developed for the 6-DOF nonlinear dynamics of a small-scale unmanned helicopter. This formulation is non-iterative and allows for the application of a wide range of nonlinear MIMO control approaches that are unsuitable for the underactuated and non affine-in-control systems. A combination of the first-principles and system identification is used to derive the control-affine model of the helicopter dynamics. Then a square input-output formulation is obtained using the control point approach. To model the rotational dynamics of the helicopter, two different methods including the "hybrid model" and "first-principles" approaches are used and compared. A more detailed comparison of these models using flight test data will be presented in Chapter 5. To obtain a complete model of the helicopter for control design purposes, the inverse kinematics of the actuating mechanisms of the helicopter will be derived in Chapter 4. A robust control design based on the square and control-affine model of the helicopter will be presented in Chapter 6.

Chapter 4

Kinematic Modeling of the Actuating Mechanisms[1]

The actuating mechanisms of a small-scale helicopter, often known as the Bell-Hiller mixer, is a system of multiple linkage mechanisms which are complex and nonlinear and difficult to mathematically model without linearizing and simplifying.

To design a model-based controller for a small-scale helicopter, a kinematic model of its actuating mechanisms is required. The detailed kinematic model of a 4-point swashplate mechanism and the Bell-Hiller mixer is still lacking in the literature. These complex mechanisms have highly nonlinear kinematics but are often treated as linear linkage mechanisms using simplifying assumptions [46, 50]. These simplifications could reduce the accuracy of the model.

A kinematic model of a 3-point swashplate mechanism and the Bell-Hiller mixer is presented in [46] and a linear model using the small angle assumptions is derived. Another approach for the kinematic model of the actuating mechanisms is described in [50] where experimental data from the actuating mechanisms of the helicopter is obtained and a curve-fitting method is used to obtain a linear relation between the servo actuator inputs and the collective pitch of the main

[1] A version of this chapter has been submitted for publication in [32].

and tail blades.

Another kinematic model for a 3-point swashplate mechanism and the Bell-Hiller mixer of a small-scale helicopter is described in [51], which results in a set of nonlinear algebraic equations solved by numerical methods. This is an iterative method which requires a high amount of computations making it unsuitable for real-time control applications.

Another approach for the kinematic model of the actuating mechanisms of a small-scale helicopter is presented in [52] using the forward and inverse kinematics of a 3-point swashplate mechanism which is modeled using the loop-closure equations. The Bell-Hiller mixer is modeled by writing the loop-closure equations in the Cartesian coordinates and using the dialytic elimination method. This results in 48 solutions through solving a 48^{th}-order polynomial and requires applying a large number of additional constraints to find the true solution.

In the next section, the inverse kinematics of the main rotor actuating mechanisms including a 4-point swashplate mechanism and the Bell-Hiller mixer as well as the actuating mechanism of the tail rotor are derived for a small-scale helicopter using a different approach that is suitable for the real-time control applications. The inverse kinematics of the actuating mechanisms of the helicopter is particularly important for the controller to calculate the required servo inputs.

4.1 Main Rotor Mechanism

The main rotor actuating mechanism of a small-scale helicopter is composed of two complex linkage mechanisms: the swashplate mechanism and the Bell-Hiller mixer. First, the kinematic equations of a 4-point swashplate mechanism are derived. Then, the kinematic model of the Bell-Hiller mixer is derived in the next section.

4.1.1 Swashplate Mechanism

The swashplate mechanism, shown in Figure 4.1, is composed of two pinned plates, one rotating and the other one stationery. Four servos allow for a three-dimensional motion of the lower stationery plate which cause certain points on the upper rotating plate such as A and B to experience different movements as the azimuth angle changes.

The motion of the swashplate is characterized by two successive Euler rotations, δ_x and δ_y, respectively around x_1 and y_1 axes of the fixed coordinates $\{x_1 y_1 z_1\}$ attached to the swashplate's lower stationery plate at the point C and the vertical displacement z_c from the center of the swashplate, point C, to the origin of the reference coordinate $\{x_i y_i z_i\}$, point O.

The forward kinematics of the swashplate is a procedure to calculate the swashplate's orientations δ_x and δ_y, and displacement z_c, in terms of the corresponding servo angles θ_{11} to θ_{41}.

To derive the forward and inverse kinematics of the swashplate mechanism, the method used in [51] is extended to a four-point swashplate mechanism used in the Evolution-EX helicopter. In this method, the position of each corner point b_1 to b_4, is calculated using two different kinematic loops. Then, the kinematic equations are derived by equating the relations found from each kinematic loop. For instance, the position of the point b_1 can be calculated either through the linkage $Op_1j_1b_1$ expressed in the reference coordinates $\{x_i y_i z_i\}$, or by expressing its position first in the local coordinates $\{x_1 y_1 z_1\}$, then in the reference coordinates $\{x_i y_i z_i\}$ through a homogeneous transformation. This procedure is repeated

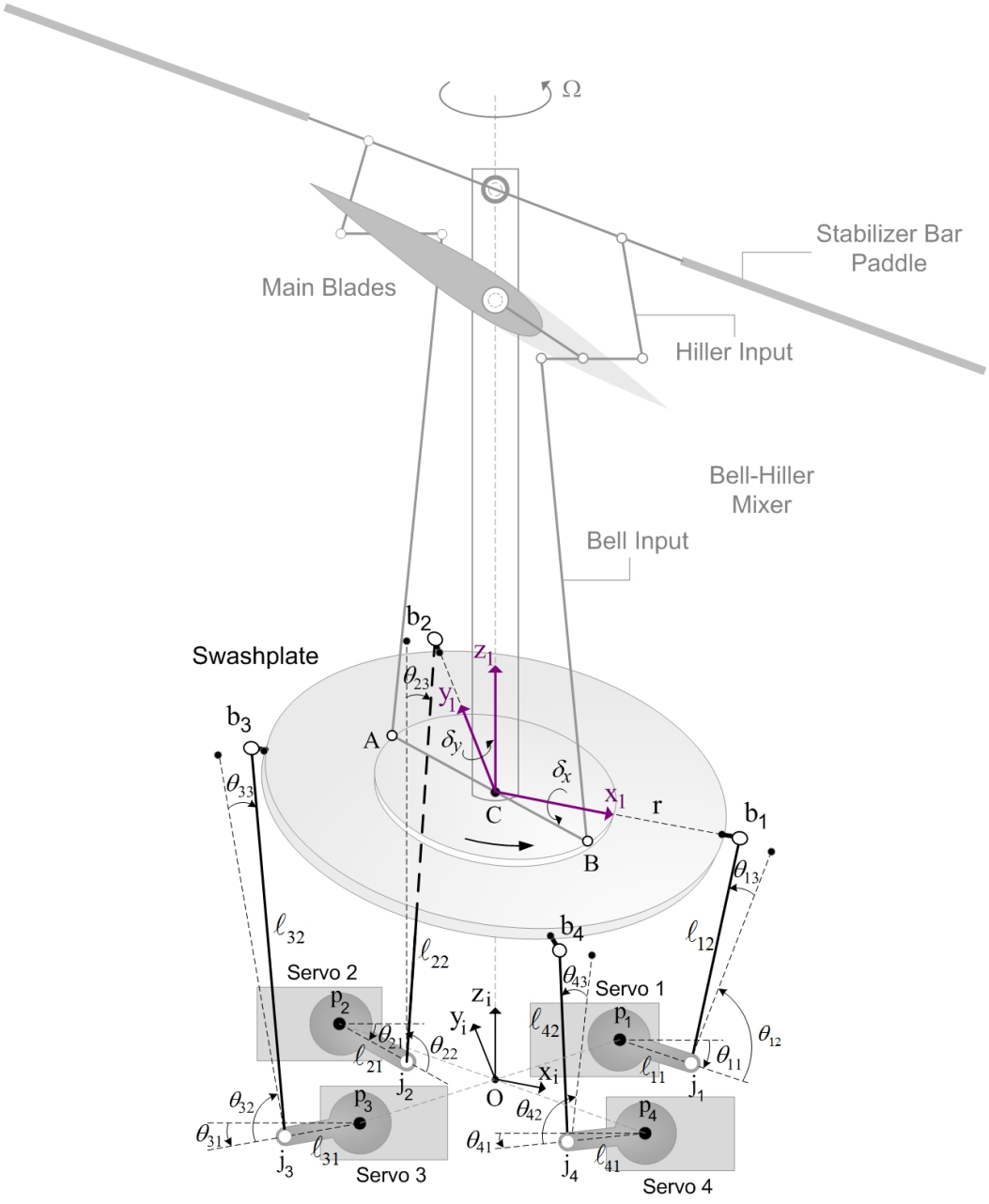

Figure 4.1: Helicopter Swashplate mechanism.

for all four points on the swashplate as follows:

$$\begin{aligned}
\mathbf{R}^i_{b1} &= \mathbf{H}^i_1 r_{b_1} = \mathbf{T}_{y,y_{p_1}} \mathbf{T}_{x,x_{p_1}} \mathbf{R}_{y,\theta_{11}} \mathbf{T}_{x,\ell_{11}} \mathbf{R}_{y,\theta_{12}} \mathbf{R}_{z,\theta_{13}} \mathbf{l}_{b_1} \\
\mathbf{R}^i_{b2} &= \mathbf{H}^i_1 r_{b_2} = \mathbf{T}_{y,y_{p_2}} \mathbf{T}_{x,x_{p_2}} \mathbf{R}_{y,\theta_{21}} \mathbf{T}_{x,\ell_{21}} \mathbf{R}_{y,\theta_{22}} \mathbf{R}_{z,\theta_{23}} \mathbf{l}_{b_2} \\
\mathbf{R}^i_{b3} &= \mathbf{H}^i_1 r_{b_3} = \mathbf{T}_{y,y_{p_3}} \mathbf{T}_{x,x_{p_3}} \mathbf{R}_{y,\theta_{31}} \mathbf{T}_{x,-\ell_{31}} \mathbf{R}_{y,\theta_{32}} \mathbf{R}_{z,\theta_{33}} \mathbf{l}_{b_3} \\
\mathbf{R}^i_{b4} &= \mathbf{H}^i_1 r_{b_4} = \mathbf{T}_{y,y_{p_4}} \mathbf{T}_{x,x_{p_4}} \mathbf{R}_{y,\theta_{41}} \mathbf{T}_{x,-\ell_{41}} \mathbf{R}_{y,\theta_{42}} \mathbf{R}_{z,\theta_{43}} \mathbf{l}_{b_4}
\end{aligned} \tag{4.1}$$

where,

$$\begin{aligned}
&\mathbf{r}_{b_1} = [r\ 0\ 0\ 1]^T,\ \mathbf{r}_{b_2} = [0\ r\ 0\ 1]^T,\ \mathbf{r}_{b_3} = [-r\ 0\ 0\ 1]^T,\ \mathbf{r}_{b_4} = [0\ -r\ 0\ 1]^T \\
&\mathbf{l}_{b_1} = [\ell_{12}\ 0\ 0\ 1]^T,\ \mathbf{l}_{b_2} = [\ell_{22}\ 0\ 0\ 1]^T,\ \mathbf{l}_{b_3} = [-\ell_{32}\ 0\ 0\ 1]^T,\ \mathbf{l}_{b_4} = [-\ell_{42}\ 0\ 0\ 1]^T
\end{aligned}$$

and $\mathbf{H}^i_1$ is the homogeneous transformation between the coordinates $\{\mathrm{x_1 y_1 z_1}\}$ and $\{\mathrm{x_i y_i z_i}\}$ defined as:

$$\mathbf{H}^i_1 = \mathbf{T}_{z,z_c} \mathbf{R}_{y,\delta_y} \mathbf{R}_{x,\delta_x} \tag{4.2}$$

and $\mathbf{R}$ and $\mathbf{T}$ are homogenous rotation and transformation matrices defined as:

$$\mathbf{R}_{x,\delta_x} = \begin{bmatrix} 1 & 0 & 0 & 0 \\ 0 & \cos\delta_x & -\sin\delta_x & 0 \\ 0 & \sin\delta_x & \cos\delta_x & 0 \\ 0 & 0 & 0 & 1 \end{bmatrix},\ \mathbf{R}_{y,\delta_y} = \begin{bmatrix} \cos\delta_y & 0 & \sin\delta_y & 0 \\ 0 & 1 & 0 & 0 \\ -\sin\delta_y & 0 & \cos\delta_y & 0 \\ 0 & 0 & 0 & 1 \end{bmatrix}$$

$$\mathbf{T}_{x,\ell_{11}} = \begin{bmatrix} 1 & 0 & 0 & \ell_{11} \\ 0 & 1 & 0 & 0 \\ 0 & 0 & 1 & 0 \\ 0 & 0 & 0 & 1 \end{bmatrix},\ \mathbf{T}_{y,y_{p_1}} = \begin{bmatrix} 1 & 0 & 0 & 0 \\ 0 & 1 & 0 & y_{p_1} \\ 0 & 0 & 1 & 0 \\ 0 & 0 & 0 & 1 \end{bmatrix},\ \mathbf{T}_{z,z_c} = \begin{bmatrix} 1 & 0 & 0 & 0 \\ 0 & 1 & 0 & 0 \\ 0 & 0 & 1 & z_c \\ 0 & 0 & 0 & 1 \end{bmatrix} \tag{4.3}$$

Expanding Eq. (4.1) results in:

$$
\begin{aligned}
& r\cos\delta_y - x_{p_1} = \ell_{12}\cos\theta_{11} + \ell_{12}\cos\theta_{13} + \ell_{11}\cos\theta_{11} \\
& r\sin\delta_y - z_c = \ell_{12}\sin\theta_{11} + \ell_{12}\cos\theta_{13} + \ell_{11}\sin\theta_{11} \\
& \cos^2\theta_{13} = 1 - \left(\frac{y_{p_1}}{\ell_{12}}\right)^2 \\
& r\sin\delta_x\sin\delta_y - x_{p_2} = \ell_{22}\cos\theta_{21} + \ell_{22}\cos\theta_{23} + \ell_{21}\cos\theta_{21} \\
& -r\sin\delta_x\cos\delta_y - z_c = \ell_{22}\sin\theta_{21} + \ell_{22}\cos\theta_{23} + \ell_{21}\sin\theta_{21} \\
& \cos^2\theta_{23} = 1 - \left(\frac{r\cos\delta_x - y_{p_2}}{\ell_{22}}\right)^2 \\
& r\cos\delta_y + x_{p_3} = \ell_{32}\cos\theta_{31} + \ell_{32}\cos\theta_{33} + \ell_{31}\cos\theta_{31} \\
& r\sin\delta_y + z_c = \ell_{32}\sin\theta_{31} + \ell_{32}\cos\theta_{33} + \ell_{31}\sin\theta_{31} \\
& \cos^2\theta_{33} = 1 - \left(\frac{y_{p_3}}{\ell_{32}}\right)^2 \\
& r\sin\delta_x\sin\delta_y + x_{p_4} = \ell_{42}\cos\theta_{41} + \ell_{42}\cos\theta_{43} + \ell_{41}\cos\theta_{41} \\
& -r\sin\delta_x\cos\delta_y + z_c = \ell_{42}\sin\theta_{41} + \ell_{42}\cos\theta_{43} + \ell_{41}\sin\theta_{41} \\
& \cos^2\theta_{43} = 1 - \left(\frac{r\cos\delta_x + y_{p_4}}{\ell_{42}}\right)^2
\end{aligned}
\tag{4.4}
$$

Denoting the left hand side of the equations in Eq. (4.4) in order by n_i,

$i = 1\text{to}12$, and rearranging the equations results in:

$$\begin{aligned}
\left(n_1 - \ell_{11}\cos\theta_{11}\right)^2 &= \ell_{12}^2\cos^2\left(\theta_{11}+\theta_{12}\right)\cos^2\theta_{13}\\
\left(n_2 - \ell_{11}\sin\theta_{11}\right)^2 &= \ell_{12}^2\sin^2\left(\theta_{11}+\theta_{12}\right)\cos^2\theta_{13}\\
\left(n_4 - \ell_{21}\cos\theta_{21}\right)^2 &= \ell_{22}^2\cos^2\left(\theta_{21}+\theta_{22}\right)\cos^2\theta_{23}\\
\left(n_5 - \ell_{21}\sin\theta_{21}\right)^2 &= \ell_{22}^2\sin^2\left(\theta_{21}+\theta_{22}\right)\cos^2\theta_{23}\\
\left(n_7 - \ell_{31}\cos\theta_{31}\right)^2 &= \ell_{32}^2\cos^2\left(\theta_{31}+\theta_{32}\right)\cos^2\theta_{33}\\
\left(n_8 - \ell_{31}\sin\theta_{31}\right)^2 &= \ell_{32}^2\sin^2\left(\theta_{31}+\theta_{32}\right)\cos^2\theta_{33}\\
\left(n_{10} - \ell_{41}\cos\theta_{41}\right)^2 &= \ell_{42}^2\cos^2\left(\theta_{41}+\theta_{42}\right)\cos^2\theta_{43}\\
\left(n_{11} - \ell_{41}\sin\theta_{41}\right)^2 &= \ell_{42}^2\sin^2\left(\theta_{41}+\theta_{42}\right)\cos^2\theta_{43}
\end{aligned} \tag{4.5}$$

Rearranging Eq. (4.5), the forward kinematics of the swashplate are:

$$\left(n_1 - \ell_{11}\cos\theta_{11}\right)^2 + \left(n_2 - \ell_{11}\sin\theta_{11}\right)^2 = n_3\ell_{12}^2 \tag{4.6}$$

$$\left(n_4 - \ell_{21}\cos\theta_{21}\right)^2 + \left(n_5 - \ell_{21}\sin\theta_{21}\right)^2 = n_6\ell_{22}^2 \tag{4.7}$$

$$\left(n_7 - \ell_{31}\cos\theta_{31}\right)^2 + \left(n_8 - \ell_{31}\sin\theta_{31}\right)^2 = n_9\ell_{32}^2 \tag{4.8}$$

$$\left(n_{10} - \ell_{41}\cos\theta_{41}\right)^2 + \left(n_{11} - \ell_{41}\sin\theta_{41}\right)^2 = n_{12}\ell_{42}^2 \tag{4.9}$$

Given the values of the servo inputs, the unknown variables of the swashplate mechanism, δ_x, δ_y and z_c can be calculated using Eqs. (4.6) to (4.9). This set of nonlinear algebraic equations does not have a closed-form solution and must be solved using numerical methods. A solution process could be first to solve Eqs. (4.6) and (4.8) for δ_y and z_c and then, solve Eq. (4.7) for δ_x. Next, the calculated unknown variables, δ_x, δ_y and z_c, are checked to satisfy Eq. (4.9). However, the inverse kinematic of the swashplate mechanism which is required for the control design has a closed-form analytical solution as described next.

To derive the inverse kinematics of the swashplate, Eqs. (4.6) to (4.9) are used again to calculate the servo angles, θ_{11} to θ_{41}, in terms of the swashplate's orientations δ_x and δ_y, and displacement z_c. By expanding and rearranging Eqs. (4.6) to (4.9), the inverse kinematic of the swashplate mechanism is calculated as:

$$\begin{aligned}
\theta_{11} &= \arccos\left(\frac{\ell_{11}^2 - n_3\ell_{12}^2 + n_1^2 + n_2^2}{2n_1\ell_{11}}\cos\beta_1\right) + \beta_1 \\
\theta_{21} &= \arccos\left(\frac{\ell_{21}^2 - n_6\ell_{22}^2 + n_4^2 + n_5^2}{2n_4\ell_{21}}\cos\beta_2\right) + \beta_2 \\
\theta_{31} &= \arccos\left(\frac{\ell_{31}^2 - n_9\ell_{32}^2 + n_7^2 + n_8^2}{2n_7\ell_{31}}\cos\beta_3\right) + \beta_3 \\
\theta_{41} &= \arccos\left(\frac{\ell_{41}^2 - n_{12}\ell_{42}^2 + n_{10}^2 + n_{11}^2}{2n_{10}\ell_{41}}\cos\beta_4\right) + \beta_4
\end{aligned} \tag{4.10}$$

where,

$$\beta_i = \arctan\left(\frac{n_{3i-1}}{n_{3i-2}}\right),\ i = 1 \text{ to } 4 \tag{4.11}$$

The closed-form solution for the inverse kinematics of the swashplate mechanism derived in Eq. (4.10) is used for the control experiments in Chapters 7 and 8.

4.1.2 Bell-Hiller Mixer

The pitch angle of the main rotor blades can change both collectively and cyclically. The Bell-Hiller mixer is the core part of the main rotor actuating mechanism, that changes the collective and cyclic pitch angles of the main rotor blades by mixing the Bell and Hiller inputs as shown in Figure 4.2. The pitch angle of the main rotor blades can be represented by the first harmonic components of the Fourier series expansion in terms of the azimuth angle Ψ:

$$\theta_{mr} = \delta_{col} + \delta_{lat}\sin(\Psi) + \delta_{lon}\cos(\Psi) \tag{4.12}$$

Solving the inverse kinematics of the Bell-Hiller mixer results in the corresponding orientations δ_x and δ_y, and displacement z_c, of the swashplate in terms of the desired collective and cyclic pitch of the blades. This is a complicated 12-bar linkage mechanism with inputs as the pitch angle of the main blade Θ_6, and the flapping angle of the stabilizer bar Θ_4, and the outputs as the swashplate orientations δ_x and δ_y, and the displacement z_c. The kinematic equations of the Bell-Hiller mixer are derived in two steps described as follows.

4.1.3 Collective Pitch to Swashplate Displacement

In the first step, the inverse kinematics of the Bell-Hiller mixer is derived so that the vertical displacement of the swashplate z_c is obtained in terms of the collective pitch of the main rotor δ_{col}. To do this, the kinematic equations are derived for the azimuth angle at which the cyclic pitch is zero and the blades only have a collective pitch. In the second step, the kinematic equations are derived so that the orientations of the swashplate δ_x and δ_y, are obtained in terms of the cyclic pitch of the main rotor.

Unlike the swashplate mechanism, the inverse kinematics of the Bell-Hiller mixer does not have a closed-form solution. Therefore, a fast numerical approach is used in this section to solve the inverse kinematics of the Bell-Hiller mixer. In this approach, the kinematic equations of the Bell-Hiller mixer are derived in the isotropic coordinates using the "vector loops" approach to minimize the computations.

Since the Bell-Hiller mixer is a symmetrical mechanism, a seven-bar linkage, a half-model of the mechanism shown in Figure 4.2, is used for simplicity. To obtain the inverse kinematics of this linkage, the kinematic equations for the loop-closures "C2386C" and "457864" are derived. First, the following variables

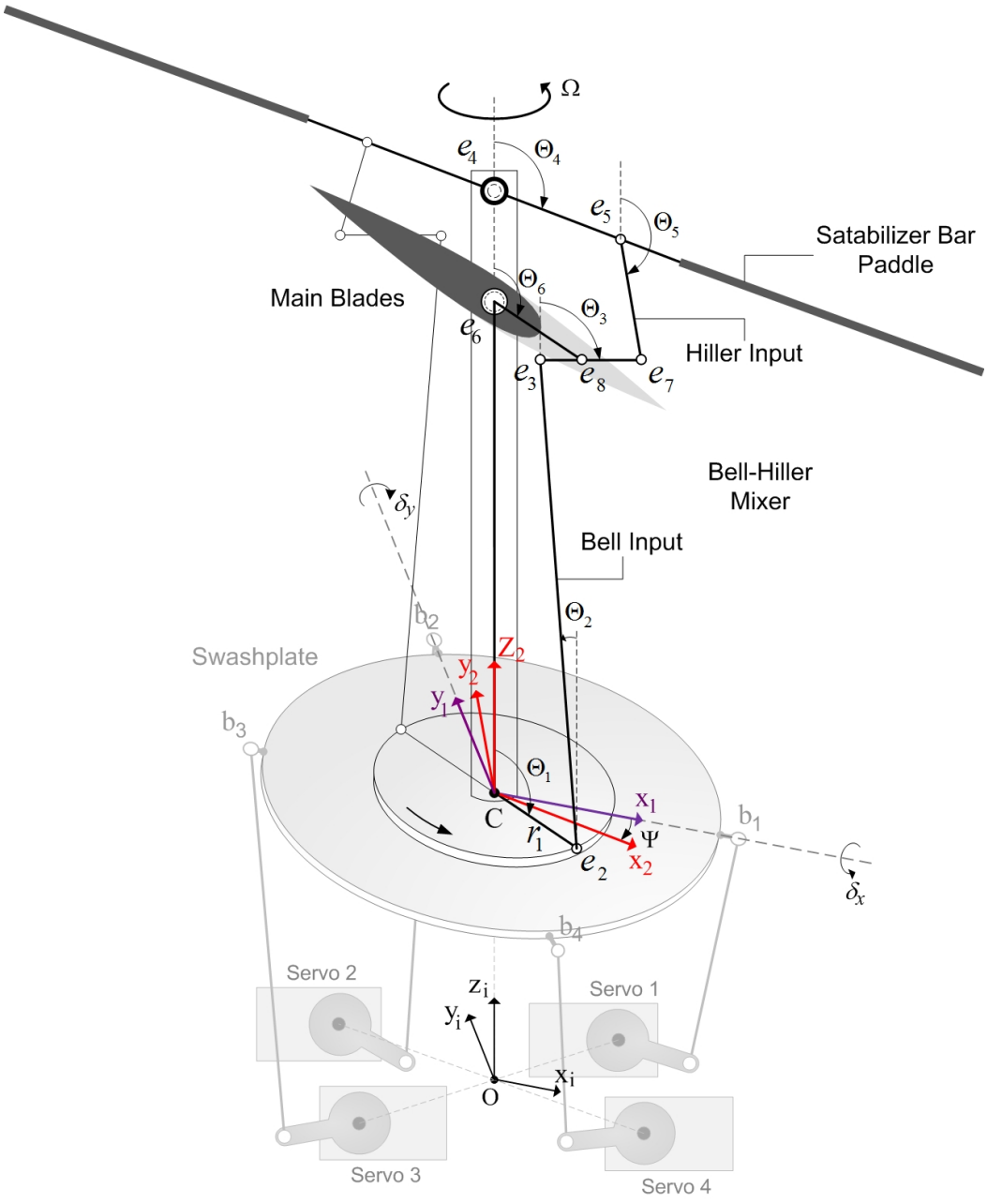

Figure 4.2: Helicopter Bell-Hiller Mixer mechanism.

are defined:

$$\theta_i = e^{i\Theta_i} = \cos\Theta_i + i\sin\Theta_i, \quad i = 1 \text{ to } 6 \tag{4.13}$$

where Θ_i are the linkage angles shown in Figure 4.2 in radians. For example, the angle Θ_6 is the input to the inverse kinematics and is related to the collective pitch as:

$$\Theta_6 = \frac{\pi}{2} - \delta_{col} \tag{4.14}$$

Also, the length variables a_i and b_i are defined in Table 4.1.

Table 4.1: Parameters of the Bell-Hiller mixer.

$a_0 = \ell_{e_6e_4}$	$a_3 = \ell_{e_3e_8}$	$a_6 = \ell_{e_6e_8}$
$a_1 = \ell_{Ce_2}$	$a_4 = \ell_{e_4e_5}$	$b_1 = \ell_{e_8e_7}$
$a_2 = \ell_{e_2e_3}$	$a_5 = \ell_{e_5e_7}$	$S = \ell_{Ce_6}$

Since the kinematic equations relating the vertical displacement of the swashplate to the collective pitch of the blade is desired in this step, the variables θ_1, θ_4, θ_6 are defined as the inputs, and θ_2, θ_3, θ_5 and S are defined as the outputs of the mechanism. Modeling the links as vectors in the complex plane results in:

$$\begin{aligned} S + a_6\theta_6 &= a_1\theta_1 + a_2\theta_2 + a_3\theta_3 \\ a_0 + a_4\theta_4 + a_5\theta_5 &= a_6\theta_6 + b_1\theta_3 \end{aligned} \tag{4.15}$$

Rearranging Eq. (4.15) to solve for θ_2 and θ_5 in terms of S and θ_3 results in:

$$\begin{aligned} a_2\theta_2 &= S + C_1 - a_3\theta_3 \\ a_5\theta_5 &= C_2 + b_1\theta_3 \end{aligned} \tag{4.16}$$

where,

$$\begin{aligned} C_1 &= a_6\theta_6 - a_1\theta_1 \\ C_2 &= a_6\theta_6 - a_4\theta_4 - a_0 \end{aligned} \tag{4.17}$$

Solving the inverse kinematics of linkage at zero cyclic pitch angle results in:

$$\Theta_1 = \Theta_4 = \frac{\pi}{2} \tag{4.18}$$

Substituting Eq. (4.18) into (4.17) results in:

$$\begin{aligned} C_1 &= a_6\theta_6 - a_1 i \\ C_2 &= a_6\theta_6 - a_4 i - a_0 \end{aligned} \tag{4.19}$$

Equation (4.19) is used to eliminate θ_2 and θ_5 in Eq. (4.16). Multiplying both sides of the Eq. (4.16) by their complex conjugate parts and using the unit vector relations $\theta_2\bar{\theta}_2 = 1$ and $\theta_5\bar{\theta}_5 = 1$, where bar denotes the complex conjugate, results in:

$$\begin{aligned} a_2^2 &= (S + C_1 - a_3\theta_3)(\bar{S} + \bar{C}_1 - a_3\theta_3^{-1}) \\ a_5^2 &= (C_2 + b_1\theta_3)(\bar{C}_2 + b_1\theta_3^{-1}) \\ S &= \bar{S} \end{aligned} \tag{4.20}$$

Expanding Eq. (4.20) results in:

$$f_j = \alpha_{0j} + \alpha_{1j}\theta_3 + \alpha_{2j}S + \beta_{1j}\theta_3^{-1} + \beta_{2j}\theta_3^{-1}S = 0, \quad j = 1, 2$$
$$f_3 = \bar{S} - S = 0 \tag{4.21}$$

where,

$$\alpha_{01} = C_1\bar{S} + C_1\bar{C}_1 + a_3^2 - a_2^2 \qquad \alpha_{02} = b_1^2 - a_5^2 + C_2\bar{C}_2$$
$$\alpha_{11} = -a_3(\bar{C}_1 + \bar{S}) \qquad \alpha_{12} = b_1\bar{C}_2$$
$$\alpha_{21} = \bar{S} + \bar{C}_1 \qquad \alpha_{22} = 0$$
$$\beta_{11} = -C_1a_3 \qquad \beta_{12} = b_1C_2$$
$$\beta_{21} = -a_3 \qquad \beta_{22} = 0 \tag{4.22}$$

Multiplying each of the three equations in Eq. (4.21) by the monomials 1, θ_3, and S and using the Sylvester-Type Elimination method [53], results in:

$$\mathbf{Q}_{9\times9}\mathbf{m}_{9\times1} = 0 \tag{4.23}$$

where $\mathbf{m}_{9\times1}$ is the vector of the monomials and $\mathbf{Q}_{9\times9}$ is the matrix obtained by

multiplying Eq. (4.21) by the the monomials as:

$$\mathbf{Q}_{9\times 9} = \begin{bmatrix} \alpha_{01} & \alpha_{11} & \alpha_{21} & 0 & 0 & 0 & \beta_{11} & \beta_{21} & 0 \\ \beta_{11} & \alpha_{01} & \beta_{21} & \alpha_{11} & \alpha_{21} & 0 & 0 & 0 & 0 \\ 0 & 0 & \alpha_{01} & 0 & \alpha_{11} & \alpha_{21} & 0 & \beta_{11} & \beta_{21} \\ \alpha_{02} & \alpha_{12} & \alpha_{22} & 0 & 0 & 0 & \beta_{12} & \beta_{22} & 0 \\ \beta_{12} & \alpha_{02} & \beta_{22} & \alpha_{12} & \alpha_{22} & 0 & 0 & 0 & 0 \\ 0 & 0 & \alpha_{02} & 0 & \alpha_{12} & \alpha_{22} & 0 & \beta_{12} & \beta_{22} \\ \bar{S} & 0 & -1 & 0 & 0 & 0 & 0 & 0 & 0 \\ 0 & \bar{S} & 0 & 0 & -1 & 0 & 0 & 0 & 0 \\ 0 & 0 & \bar{S} & 0 & 0 & -1 & 0 & 0 & 0 \end{bmatrix}, \quad \mathbf{m}_{9\times 1} = \begin{bmatrix} 1 \\ \theta_3 \\ S \\ \theta_3^2 \\ \theta_3 S \\ S^2 \\ \theta_3^{-1} \\ \theta_3^{-1} S \\ \theta_3^{-1} S^2 \end{bmatrix} \tag{4.24}$$

Factoring the variable $\bar{S}$ from Eq. (4.24) and splitting the matrix $\mathbf{Q}$ into the sparse matrices $\mathbf{Q}_1$ and $\mathbf{Q}_2$, results in:

$$\big(\mathbf{Q}_1 + \mathbf{Q}_2 \bar{S}\big)\mathbf{m} = 0 \tag{4.25}$$

where,

$$\mathbf{Q}_{1_{9\times 9}} = \begin{bmatrix} \gamma_1 & \gamma_2 & \gamma_3 & 0 & 0 & 0 & \beta_{11} & \beta_{21} & 0 \\ \beta_{11} & \gamma_1 & \beta_{21} & \gamma_2 & \gamma_3 & 0 & 0 & 0 & 0 \\ 0 & 0 & \gamma_1 & 0 & \gamma_2 & \gamma_3 & 0 & \beta_{11} & \beta_{21} \\ \alpha_{02} & \alpha_{12} & \alpha_{22} & 0 & 0 & 0 & \beta_{12} & \beta_{22} & 0 \\ \beta_{12} & \alpha_{02} & \beta_{22} & \alpha_{12} & \alpha_{22} & 0 & 0 & 0 & 0 \\ 0 & 0 & \alpha_{02} & 0 & \alpha_{12} & \alpha_{22} & 0 & \beta_{12} & \beta_{22} \\ 0 & 0 & -1 & 0 & 0 & 0 & 0 & 0 & 0 \\ 0 & 0 & 0 & 0 & -1 & 0 & 0 & 0 & 0 \\ 0 & 0 & 0 & 0 & 0 & -1 & 0 & 0 & 0 \end{bmatrix} \tag{4.26}$$

$$\mathbf{Q}_{2_{9\times 9}} = \begin{bmatrix} C_1 & -a_3 & 1 & 0 & 0 & 0 & 0 & 0 & 0 \\ 0 & C_1 & 0 & -a_3 & 1 & 0 & 0 & 0 & 0 \\ 0 & 0 & C_1 & 0 & -a_3 & 1 & 0 & 0 & 0 \\ 0 & 0 & 0 & 0 & 0 & 0 & 0 & 0 & 0 \\ 0 & 0 & 0 & 0 & 0 & 0 & 0 & 0 & 0 \\ 0 & 0 & 0 & 0 & 0 & 0 & 0 & 0 & 0 \\ 1 & 0 & 0 & 0 & 0 & 0 & 0 & 0 & 0 \\ 0 & 1 & 0 & 0 & 0 & 0 & 0 & 0 & 0 \\ 0 & 0 & 1 & 0 & 0 & 0 & 0 & 0 & 0 \end{bmatrix} \tag{4.27}$$

and $\gamma_1 = C_1\bar{C}_1 + a_3^2 - a_2^2$, $\gamma_2 = -a_3\bar{C}_1$ and $\gamma_3 = \bar{C}_1$. In order for Eq. (4.25) to have a non-trivial solution, the following condition must hold:

$$\mathbf{Q}_1\mathbf{m} = -\bar{S}\mathbf{Q}_2\mathbf{m} \tag{4.28}$$

Equation (4.28) is a generalized eigenvalue problem and can be solved by the QZ decomposition method [54]. Also, this equation can be easily solved in MATLAB$^{\text{TM}}$as:

$$S = eig(\mathbf{Q}_1, \mathbf{Q}_2, 'qz') \tag{4.29}$$

Therefore, given the collective pitch angle, δ_{col}, the vertical displacement of the swashplate z_c is calculated as:

$$z_c = h_{e_6} - S \tag{4.30}$$

where h_{e_6} is the fixed height of the rotor grip from the point O, shown in Figure 4.2 and its value is listed in Table 4.2.

The above method provides a fast numerical solution for the nonlinear kinematics of the Bell-Hiller mixer. However, since the matrices $\mathbf{Q}_1$ and $\mathbf{Q}_2$ in Eqs. (4.26) and (4.27) are square matrices of dimension 9, solving the inverse kinematics of the Bell-Hiller mixer using the above method results in 9 solutions. This is a significant reduction compared to [52] with 48 solutions. The true solution of the inverse kinematics can be obtained by applying physical constraints of the mechanism as described in the following Pseudocode:

For i = 1 to 9
  $y = S(i)$
  If (y is real) & ($y \geq S_{min}$) & ($y \leq S_{max}$)
    $z_c = h_{e_6} - y$
End

4.1.4 Cyclic Pitch to Swashplate Orientations

Given the swashplate vertical displacement z_c in Eq. (4.30), the inverse kinematic equations of the Bell-Hiller mixer are derived so that the orientations of the swashplate expressed by the Euler angles δ_x and δ_y are obtained in terms of the lateral and longitudinal cyclic pitch angles δ_{lat} and δ_{lon}. To do this, a local coordinates $\{\mathrm{x_1y_1z_1}\}$ attached to the swashplate's moving upper plate at the point C is defined as shown in Figure 4.2. Then, according to Eq. (4.12), the kinematic equations are derived once at the azimuth angle $\Psi = 0$ deg, to solve for δ_y in terms of the longitudinal cyclic pitch δ_{lon}, and once at the azimuth angle $\Psi = 90$ deg, to solve for δ_x in terms of the lateral cyclic pitch δ_{lat}.

A similar procedure is followed to derive the kinematic equations for the orientation of the swashplate. Since the tilting angles of the swashplate to the cyclic pitch angle are desired, here the variables S, θ_4 and θ_6 are defined as the inputs, and θ_1, θ_2, θ_3 and θ_5 are defined as the outputs of the mechanism. Rearranging Eq. (4.15) to solve for θ_2 and θ_5 in terms of θ_1 and θ_3 results in:

$$\begin{aligned} a_2\theta_2 &= C_3 - a_3\theta_3 - a_1\theta_1 \\ a_5\theta_5 &= C_2 + b_1\theta_3 \end{aligned} \tag{4.31}$$

where,

$$\begin{aligned} C_2 &= a_6\theta_6 - a_0 - a_4\theta_4 \\ C_3 &= S + a_6\theta_6 \end{aligned} \tag{4.32}$$

where S is obtained from Eq. (4.29). Since the stabilizer bar's effect as a secondary input to the cyclic pitch is already included in the flapping equations (3.6) and (3.7) in Chapter 3, the flapping angle of the stabilizer bar is again considered

zero ($\Theta_4 = \frac{\pi}{2}$), and Eq. (4.32) is rewritten as:

$$\begin{aligned} C_2 &= a_6\theta_6 - a_0 - a_4 i \\ C_3 &= S + a_6\theta_6 \end{aligned} \tag{4.33}$$

Equation (4.33) is used to eliminate θ_2 and θ_5 in Eq. (4.31). Multiplying both sides of Eq. (4.31) by their complex conjugate parts and using the unit vector relations $\theta_2\bar{\theta}_2 = 1$ and $\theta_5\bar{\theta}_5 = 1$ results in:

$$\begin{aligned} a_2^2 &= (C_3 - a_3\theta_3 - a_1\theta_1)(\bar{C}_3 - a_3\theta_3^{-1} - a_1\bar{\theta}_1) \\ a_5^2 &= (C_2 + b_1\theta_3)(\bar{C}_2 + b_1\theta_3^{-1}) \\ \theta_1\bar{\theta}_1 &= 1 \end{aligned} \tag{4.34}$$

Expanding Eq. (4.34) results in:

$$\begin{aligned} f_j &= \alpha'_{0j} + \alpha'_{1j}\theta_3 + \alpha'_{2j}\theta_1 + \beta'_{1j}\theta_3^{-1} + \beta'_{2j}\theta_3^{-1}\theta_1 = 0, \quad j = 1, 2 \\ f_3 &= \theta_1\bar{\theta}_1 - 1 = 0 \end{aligned} \tag{4.35}$$

where,

$$\begin{aligned} \alpha'_{01} &= -a_1C_3\bar{\theta}_1 + C_3\bar{C}_3 + a_3^2 - a_2^2 & \alpha'_{02} &= b_1^2 - a_5^2 + C_2\bar{C}_2 \\ \alpha'_{11} &= -a_3(\bar{C}_3 - a_1\bar{\theta}_1) & \alpha'_{12} &= b_1\bar{C}_2 \\ \alpha'_{21} &= a_1^2\bar{\theta}_1 - a_1\bar{C}_3 & \alpha'_{22} &= 0 \\ \beta'_{11} &= -a_3C_3 & \beta'_{12} &= b_1C_2 \\ \beta'_{21} &= a_1a_3 & \beta'_{22} &= 0 \end{aligned} \tag{4.36}$$

Multiplying each of the three equations in Eq. (4.35) by the monomials 1, θ_1

and θ_3, and applying the Sylvester-Type Elimination method results in:

$$\mathbf{Q}'_{9\times 9}\mathbf{m}'_{9\times 1} = 0 \tag{4.37}$$

where $\mathbf{m}'_{9\times 1}$ is the vector of the monomials and $\mathbf{Q}'_{9\times 9}$ is the matrix obtained by multiplying Eq. (4.35) by the the monomials as:

$$\mathbf{Q}'_{9\times 9} = \begin{bmatrix} \alpha'_{01} & \alpha'_{11} & \alpha'_{21} & 0 & 0 & 0 & \beta'_{11} & \beta'_{21} & 0 \\ \beta'_{11} & \alpha'_{01} & \beta'_{21} & \alpha'_{11} & \alpha'_{21} & 0 & 0 & 0 & 0 \\ 0 & 0 & \alpha'_{01} & 0 & \alpha'_{11} & \alpha'_{21} & 0 & \beta'_{11} & \beta'_{21} \\ \alpha'_{02} & \alpha'_{12} & \alpha'_{22} & 0 & 0 & 0 & \beta'_{12} & \beta'_{22} & 0 \\ \beta'_{12} & \alpha'_{02} & \beta'_{22} & \alpha'_{12} & \alpha'_{22} & 0 & 0 & 0 & 0 \\ 0 & 0 & \alpha'_{02} & 0 & \alpha'_{12} & \alpha'_{22} & 0 & \beta'_{12} & \beta'_{22} \\ -1 & 0 & \bar{\theta}_1 & 0 & 0 & 0 & 0 & 0 & 0 \\ 0 & -1 & 0 & 0 & \bar{\theta}_1 & 0 & 0 & 0 & 0 \\ 0 & 0 & -1 & 0 & 0 & \bar{\theta}_1 & 0 & 0 & 0 \end{bmatrix}, \quad \mathbf{m}'_{9\times 1} = \begin{bmatrix} 1 \\ \theta_3 \\ \theta_1 \\ \theta_3^2 \\ \theta_3\theta_1 \\ \theta_1^2 \\ \theta_3^{-1} \\ \theta_3^{-1}\theta_1 \\ \theta_3^{-1}\theta_1^2 \end{bmatrix} \tag{4.38}$$

Factoring the variable $\bar{\theta}_1$ from Eq. (4.38) and splitting the matrix $\mathbf{Q}'$ into the sparse matrices $\mathbf{Q}'_1$ and $\mathbf{Q}'_2$, results in:

$$\big(\mathbf{Q}'_1 + \mathbf{Q}'_2\bar{\theta}_1\big)\mathbf{m}' = 0 \tag{4.39}$$

where,

$$\mathbf{Q}'_{1_{9\times 9}} = \begin{bmatrix} \gamma'_1 & \gamma'_2 & \gamma'_3 & 0 & 0 & 0 & \beta'_{11} & \beta'_{21} & 0 \\ \beta'_{11} & \gamma'_1 & \beta'_{21} & \gamma'_2 & \gamma'_3 & 0 & 0 & 0 & 0 \\ 0 & 0 & \gamma'_1 & 0 & \gamma'_2 & \gamma'_3 & 0 & \beta'_{11} & \beta'_{21} \\ \alpha'_{02} & \alpha'_{12} & \alpha'_{22} & 0 & 0 & 0 & \beta'_{12} & \beta'_{22} & 0 \\ \beta'_{12} & \alpha'_{02} & \beta'_{22} & \alpha'_{12} & \alpha'_{22} & 0 & 0 & 0 & 0 \\ 0 & 0 & \alpha'_{02} & 0 & \alpha'_{12} & \alpha'_{22} & 0 & \beta'_{12} & \beta'_{22} \\ -1 & 0 & 0 & 0 & 0 & 0 & 0 & 0 & 0 \\ 0 & -1 & 0 & 0 & 0 & 0 & 0 & 0 & 0 \\ 0 & 0 & -1 & 0 & 0 & 0 & 0 & 0 & 0 \end{bmatrix} \tag{4.40}$$

$$\mathbf{Q}'_{2_{9\times 9}} = \begin{bmatrix} -a_1C_3 & a_1a_3 & a_1^2 & 0 & 0 & 0 & 0 & 0 & 0 \\ 0 & -a_1C_3 & 0 & a_1a_3 & a_1^2 & 0 & 0 & 0 & 0 \\ 0 & 0 & -a_1C_3 & 0 & a_1a_3 & a_1^2 & 0 & 0 & 0 \\ 0 & 0 & 0 & 0 & 0 & 0 & 0 & 0 & 0 \\ 0 & 0 & 0 & 0 & 0 & 0 & 0 & 0 & 0 \\ 0 & 0 & 0 & 0 & 0 & 0 & 0 & 0 & 0 \\ 0 & 0 & 1 & 0 & 0 & 0 & 0 & 0 & 0 \\ 0 & 0 & 0 & 0 & 1 & 0 & 0 & 0 & 0 \\ 0 & 0 & 0 & 0 & 0 & 1 & 0 & 0 & 0 \end{bmatrix} \tag{4.41}$$

and $\gamma'_1 = C_3\bar{C}_3 + a_3^2 - a_2^2$, $\gamma'_2 = -a_3\bar{C}_3$ and $\gamma'_3 = -a_1\bar{C}_3$.

Therefore, given the longitudinal and lateral cyclic inputs δ_{lon} and δ_{lat} and the vertical displacement of the swashplate z_c, the tilt angle of the swashplate

Table 4.2: Parameters of the Bell-Hiller mixer's linear approximation.

Parameter	**Value(m)**
r_1	0.023
$\ell_{e_3e_7}$	0.038
$\ell_{e_7e_8}$	0.025
$\ell_{e_6e_8}$	0.031
z_0	0.069
h_{e_6}	0.168

Θ_1, is:

$$\Theta_1 = arg(\bar{\theta}_1) \tag{4.42}$$

where $\bar{\theta}_1$ is a complex number and is calculated using the QZ decomposition method as:

$$\bar{\theta}_1 = eig(\mathbf{Q}'_1, \mathbf{Q}'_2, 'qz') \tag{4.43}$$

In addition, a linear approximation of the inverse kinematics of the Bell-Hiller mixer is derived using the small-angle assumptions in the following for a comparison with the nonlinear model:

$$\begin{aligned}
\delta_{col} &= \frac{\ell_{e_7e_8}}{\ell_{e_3e_7}\ell_{e_6e_8}}(z_c - z_0) \\
\delta_{lon} &= -\frac{\ell_{e_7e_8}r_1}{\ell_{e_3e_7}\ell_{e_6e_8}}(\Theta_{1_{lon}}) \\
\delta_{lat} &= \frac{\ell_{e_7e_8}r_1}{\ell_{e_3e_7}\ell_{e_6e_8}}(\Theta_{1_{lat}})
\end{aligned} \tag{4.44}$$

where z_0 is the height of the swashplate from the point O shown in Figure 4.2, at zero collective pitch. The parameters of the linear approximation of the Bell-

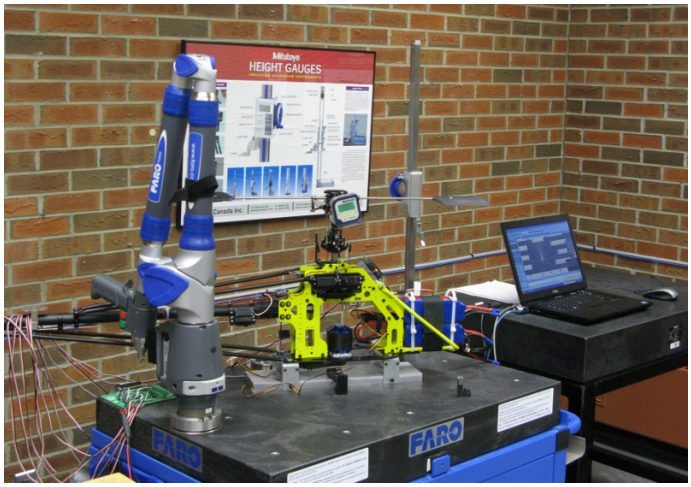

Figure 4.3: Fero arm machine used to measure the dimensions of the actuating mechanisms.

Hiller mixer kinematics in Eq. (4.44) are listed in Table 4.2. The dimensions of the actuating mechanisms are measured using a FARO arm machine shown in Figure 4.3.

Note that Eq. (4.42) calculates the longitudinal and lateral tilt angle of the swashplate $\Theta_{1_{lon}}$ and $\Theta_{1_{lat}}$, which are not necessarily equal to the swashplate's Euler angles δ_x and δ_y. To obtain the Euler angles of the swashplate in general, two basis vectors are defined as:

$$\begin{aligned} \hat{\boldsymbol{n}}_1 &= \mathbf{R}_{y,\Theta_{1_{lon}}}[1\ 0\ 0\ 0]^T \\ \hat{\boldsymbol{n}}_2 &= \mathbf{R}_{x,\Theta_{1_{lat}}}[0\ 1\ 0\ 0]^T \end{aligned} \tag{4.45}$$

where $\hat{\boldsymbol{n}}_1$ and $\hat{\boldsymbol{n}}_2$ are the perpendicular unity vectors on the tilted plane of the swashplate and $\mathbf{R}$ is the rotation matrix defined in Eq. (4.3).

By defining $\hat{\boldsymbol{n}}_3$ as the normal vector of the tilted plane of the swashplate, it can be calculated as:

$$\hat{\boldsymbol{n}}_3 = \hat{\boldsymbol{n}}_1 \times \hat{\boldsymbol{n}}_2 \tag{4.46}$$

The normal vector $\hat{\boldsymbol{n}}_3$ could also be derived in terms of the tilt angles of the swashplate δ_x and δ_y using the homogeneous transformation $\mathbf{H}_1^i$ defined in Eq. (4.2) as:

$$\hat{\boldsymbol{n}}_3 = \mathbf{H}_1^i[0\ 0\ 1\ 0]^T = [n_{31}\ n_{32}\ n_{33}\ 0]^T \tag{4.47}$$

Equating Eqs. (4.46) and (4.47) results in the swashplate's Euler angles as:

$$\begin{aligned} \delta_x &= -\arcsin\left(n_{32}\right) \\ \delta_y &= \arcsin\left(\frac{n_{31}}{\cos\delta_x}\right) \end{aligned} \tag{4.48}$$

Combining Eqs. (4.10), (4.29) and (4.42) results in the inverse kinematics of the entire main rotor actuating mechanism representing the four swash servo inputs θ_{11} to θ_{41} in terms of the collective pitch angle δ_{col} and longitudinal and lateral cyclic pitch angles of the main rotor δ_{lon} and δ_{lat}, which is essential for the control implementation in Chapters 7 and 8. The forward and inverse kinematics of the tail rotor are described in the following section.

4.2 Tail Rotor Mechanism

The tail rotor has a complex mechanism composed of two planar linkage mechanisms shown in Figure 4.4. The four-bar linkage mechanism "1234", moves the L-shape link "345" pivoted at point "4". An spherical joint at point "5", connects this link to a T-shaped link which slides on the spinning shaft of the tail rotor. As the T-bar slides on the shaft, the pitch angle of the tail blade changes through another linkage mechanism "5678".

To derive the forward kinematics of the tail rotor mechanism, two kinematic loops "12341" and "56785" are defined and the kinematic equations are derived by

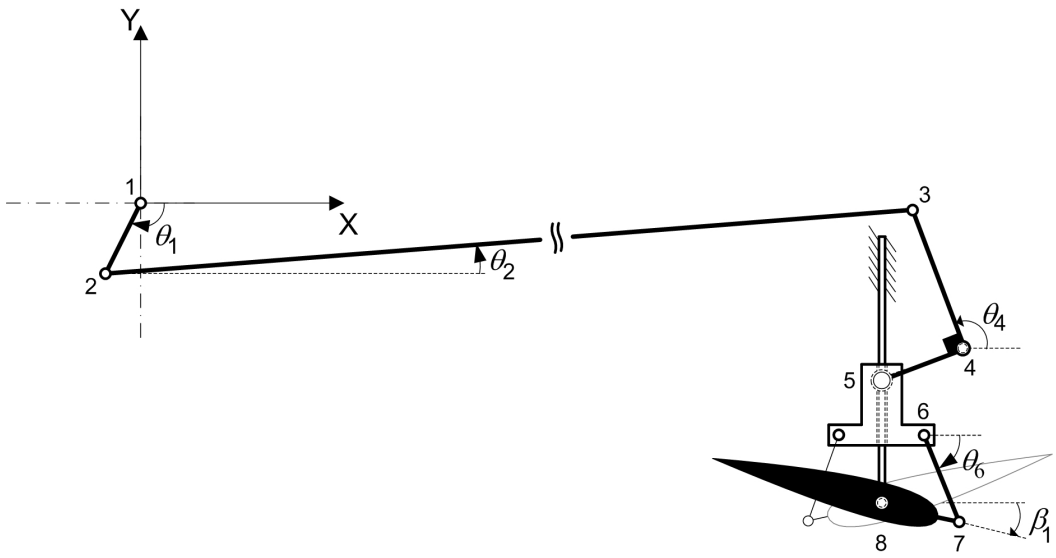

Figure 4.4: Helicopter tail mechanism.

writing the loop-closure equations for each loop. Writing the kinematic equations for the loop-closure "12341" results in:

$$\boldsymbol{l}_{12} + \boldsymbol{l}_{23} = \boldsymbol{l}_{14} + \boldsymbol{l}_{43} \tag{4.49}$$

Expanding (4.49) in the Cartesian coordinates results in:

$$\begin{aligned} c_1 \cos\theta_1 + c_2 \cos\theta_2 &= c_4 \cos\theta_4 + x_4 \\ c_1 \sin\theta_1 + c_2 \sin\theta_2 &= c_4 \sin\theta_4 + y_4 \end{aligned} \tag{4.50}$$

where $c_1 = |\boldsymbol{l}_{12}|$, $c_2 = |\boldsymbol{l}_{23}|$, $c_4 = |\boldsymbol{l}_{43}|$ and x_4 and y_4 are the horizontal and vertical distance of the point "4" form the origin of the X-Y coordinates, respectively.

Rearranging Eq. (4.50) results in:

$$\begin{aligned} c_2 \cos\theta_2 &= m_1 + c_4 \cos\theta_4 \\ c_2 \sin\theta_2 &= m_2 + c_4 \sin\theta_4 \end{aligned} \tag{4.51}$$

where $m_1 = x_4 - c_1 \cos\theta_1$ and $m_2 = y_4 - c_1 \sin\theta_1$. Adding the squares of the equations in Eq. (4.51) and eliminating θ_2 results in:

$$c_2^2 = (m_1 + c_4 \cos\theta_4)^2 + (m_2 + c_4 \sin\theta_4)^2 \tag{4.52}$$

Solving Eq. (4.52) for θ_4 results in:

$$\theta_4 = \arccos\left(\frac{c_2^2 - c_4^2 - m_1^2 - m_2^2}{2c_4 m_1}\cos\gamma_1\right) + \gamma_1 \tag{4.53}$$

where $\gamma_1 = \arctan\left(\frac{m_2}{m_1}\right)$. Equation (4.53) provides a nonlinear relation between the angle of the L-shape link, θ_4, and the servo input θ_1.

Writing the kinematic equations for the loop-closure "56785" results in:

$$\boldsymbol{l}_{15} + \boldsymbol{l}_{56} + \boldsymbol{l}_{67} = \boldsymbol{l}_{18} + \boldsymbol{l}_{87} \tag{4.54}$$

Expanding Eq. (4.54) in the Cartesian coordinates results in:

$$\begin{aligned} x_{56} + c_6 \cos\theta_6 &= c_8 \cos\beta_1 \\ y_5 + y_{56} + c_6 \sin\theta_6 &= y_8 + c_8 \sin\beta_1 \end{aligned} \tag{4.55}$$

where $c_6 = |\boldsymbol{l}_{67}|, c_8 = |\boldsymbol{l}_{87}|$, and x_{56} and y_{56} are the fixed horizontal and vertical offsets between the points "5" and "6" on the T-shaped link and y_8 is the fixed vertical offset of the point "8" from the origin of the X-Y coordinates. The variable y_5 is the vertical displacement of the slider from the origin of the X-Y coordinates and is calculated as:

$$y_5 = y_4 + b_4 \cos\theta_4 \tag{4.56}$$

where $b_4 = |\boldsymbol{l}_{45}|$. Substituting Eq. (4.56) into Eq. (4.55) and rearranging Eq. (4.55) results in:

$$\begin{aligned} c_6 \cos\theta_6 &= m_3 + c_8 \cos\beta_1 \\ c_6 \sin\theta_6 &= m_4 + c_8 \sin\beta_1 \end{aligned} \tag{4.57}$$

where $m_3 = -x_{56}$ and $m_4 = y_8 - y_5 - y_{56}$. Adding the squares of the equations in Eq. (4.57) and eliminating θ_6 results in:

$$c_6^2 = (m_3 + c_8 \cos\beta_1)^2 + (m_4 + c_8 \sin\beta_1)^2 \tag{4.58}$$

Solving Eq. (4.58) for β_1 results in:

$$\beta_1 = \arcsin\left(\frac{c_6^2 - c_8^2 - m_3^2 - m_4^2}{2c_8 m_4}\cos\gamma_2\right) - \gamma_2 \tag{4.59}$$

where $\gamma_2 = \arctan\left(\frac{m_3}{m_4}\right)$. Equation (4.59) provides a nonlinear relation between the pitch angle of the tail blade, β_1, and the angle of the L-shape link, θ_1. Therefore, combining Eqs. (4.53) and (4.59) results in the forward kinematics of the tail mechanism which allows for the calculation of the pitch angle of the tail blade β_1, in terms of the tail servo input θ_1. The second tail blade is actuated through a mirrored mechanism as shown in Figure 4.4 and its pitch angle is equal and opposite to that of the first blade.

The model-based controller described in Chapter 6 uses the pitch angle of the tail blades as the control input for the yaw motion of the helicopter. Therefore, the inverse kinematics of the tail mechanism is required to calculate the desired servo inputs.

The inverse kinematics of the tail mechanism is required to calculate the desired servo inputs for the control design. The inverse kinematics can be ob-

tained by following a similar procedure on the same kinematic loops "12341" and "56785". Rearranging and solving Eq. (4.57) for θ_4 in terms of β_1, and then solving Eq. (4.51) for θ_1 in terms of θ_4 results in the inverse kinematics of the tail mechanism as:

$$\theta_1 = \arccos\left(\frac{(m_1')^2 + (m_2')^2 + c_1^2 - c_2^2}{2c_1 m_1'}\cos\gamma_1'\right) + \gamma_1' \tag{4.60}$$

where,

$$\begin{aligned} m_1' &= c_4\cos\theta_4 + x_4 & \theta_4 &= \arccos\left(\frac{m_4' - c_6\sin\theta_6}{b_4}\right) \\ m_2' &= c_4\sin\theta_4 + y_4 & \theta_6 &= \arccos\left(\frac{m_3'}{c_6}\right) \\ m_3' &= c_8\cos\beta_1 - x_{56} & \gamma_1' &= \arctan\left(\frac{m_2'}{m_1'}\right) \\ m_4' &= y_8 + c_8\sin\beta_1 - y_{56} - y_4 \end{aligned}$$

Again, a linear approximation of the inverse kinematics of the tail mechanism is derived for the comparison with the nonlinear model, using the small-angle assumptions as:

$$\delta_{ped} = \frac{\ell_{12}\ell_{45}}{\ell_{43}\ell_{87}}(\theta_{tail} + \frac{\pi}{2}) + \delta_{0_{tail}} \tag{4.61}$$

where,

$$\begin{aligned} \delta_{ped} &= \beta_1 \\ \theta_{tail} &= \theta_1 - \frac{\pi}{2} \end{aligned} \tag{4.62}$$

and $\theta_{0_{tail}} = 0.1169$ rad is the pitch angle of the tail blade when $\theta_{tail} = 0$. The parameter of the linear approximation of the tail rotor mechanism are listed in

Table 4.3: Parameters of the tail mechanism's linear approximation.

Parameter	**Value(m)**
ℓ_{12}	0.018
ℓ_{45}	0.015
ℓ_{43}	0.032
ℓ_{87}	0.015

Table 4.3. In addition, the tail rotor pitch can be expressed in terms of the pulse width of the tail servo of the Evolution-EX helicopter as:

$$\theta_{tail} = \alpha_{tail}(PW) + \delta_{0_{tail}} \tag{4.63}$$

where PW is the pulse width of the pulse width modulation (PWM) servo signal in seconds and the coefficients $\alpha_{tail} = -1698.5$ rad/s and $\delta_{0_{tail}} = 1.4724$ rad are obtained from the calibration diagram of the tail servo.

4.3 Experimental Validation of the Kinematic Model

To validate the derived inverse kinematic models of the main rotor represented by Eqs. (4.10), (4.29) and (4.42) and the tail rotor kinematic model in Eq. (4.60), two simple experimental setups shown in Figs. 4.5 and 4.6 are used. To accurately measure the pitch angles of the main and tail blades, a 2000 pulse per revolution (PPR) optical encoder is attached to each blade grip of the main rotor and one blade grip of the tail rotor on the Evolution-EX helicopter.

The data collection process is automatic. The servo signals and the measurement data from the encoders are collected at the same time using a PCI-6602 National Instrument data acquisition card and a PC running the xPC Target real-time kernel. The experimental data is collected by sending PWM signals to

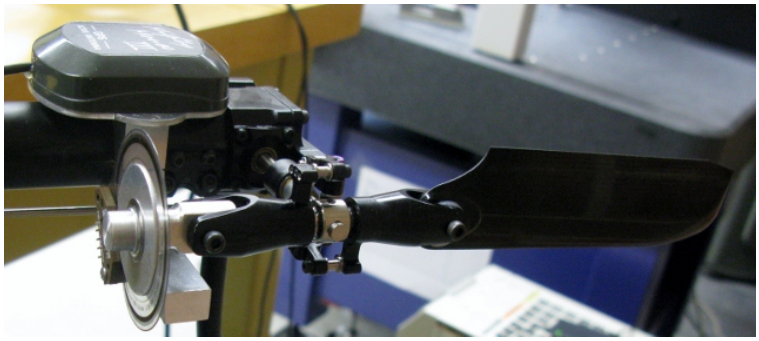

Figure 4.5: The measurement setup for the tail rotor mechanism.

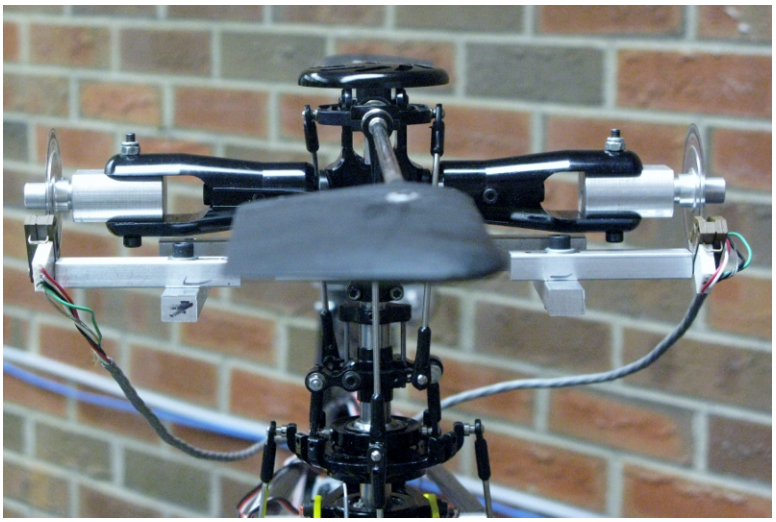

Figure 4.6: The measurement setup for the main rotor mechanism.

the servos of the helicopter and measuring the corresponding blade pitch angles using the optical encoders shown in Figs. 4.5 and 4.6. For example, to validate the kinematic model of the collective pitch to the swashplate displacement in Eq. (4.29), the stabilizer bar is fixed at zero flapping angle and the four servos of the main rotor are commanded such that the swashplate moves vertically and z_c increases from 60 to 80 mm in increments of about 2.5 mm, while the tilt of the swashplate is kept at zero ($\delta_x = \delta_y = 0$), and at the same time, the corresponding encoder measurements from each blade grip are collected.

The above process is repeated for the longitudinal and lateral cyclic tests and the tail rotor mechanism. The experimental data and predicted responses

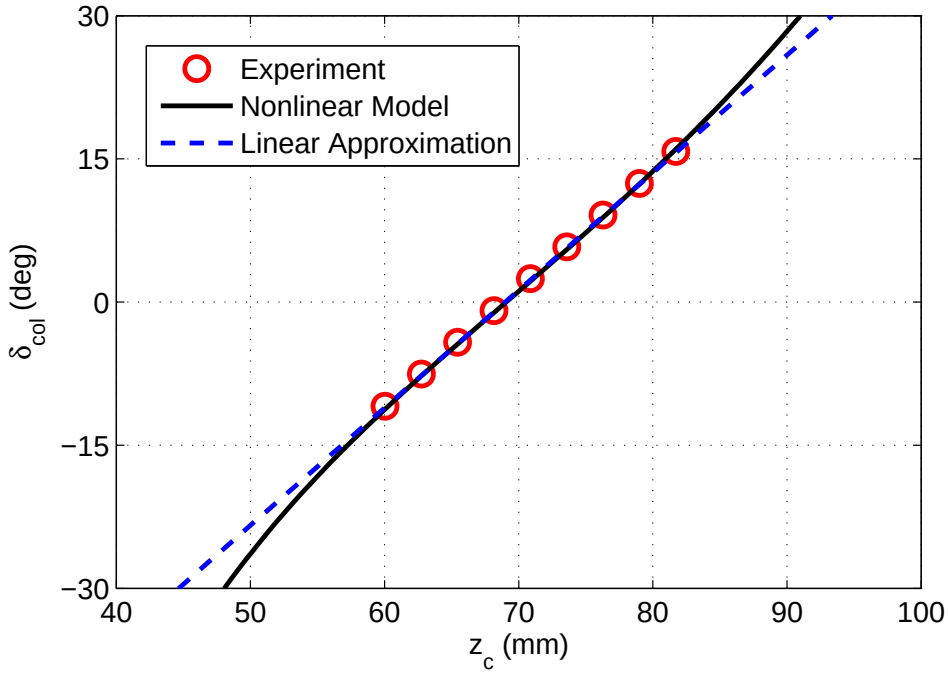

Figure 4.7: Experimental results of the collective pitch versus swashplate displacement and comparison to the nonlinear model and linear approximation.

of the nonlinear kinematic model of the actuating mechanisms of the helicopter as well as the linear approximation models are compared in Figures 4.7 to 4.10, which shows a good match between the predicted nonlinear kinematic model of the main and tail rotor mechanisms and the experimental data. Therefore, the inverse kinematics of the helicopter actuating mechanisms are validated.

The results in Figures 4.7 to 4.10 also indicate that the Bell-Hiller mixer and the tail rotor mechanism of the helicopter are designed such that the kinematic models obtained from the linear approximations accurately represent the actual kinematics of the system within the operation range of the servos. However, the linear approximations are not valid for a larger range of servo angles. For example, in the collective pitch versus swashplate displacement graph shown in Figure 4.7, the prediction of the nonlinear kinematic model deviates from the

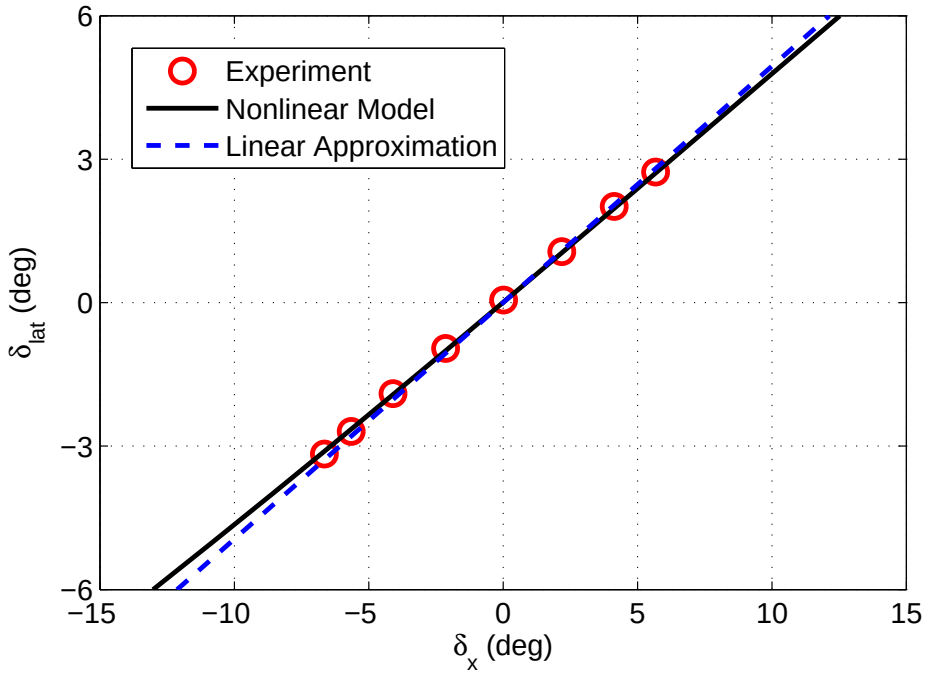

Figure 4.8: Experimental results of the lateral cyclic pitch versus swashplate orientation and comparison to the nonlinear model and linear approximation.

linear approximation model for collective pitch angles larger than 15 deg.

4.4 Summary

The inverse kinematics of the actuating mechanisms of the main rotor including a 4-point swashplate mechanism and the Bell-Hiller mixer and the actuating mechanism of the tail rotor have been developed for a small-scale helicopter, which will be used for the control experiments in Chapters 7 and 8. The linear approximations of the nonlinear kinematics of the main and tail rotor actuating mechanisms are also derived. The kinematic models of the main and tail rotor mechanisms are validated in experiments and the nonlinear models and the linear approximations are compared. The system identification and validation of the mathematical model of the helicopter will be presented in the next chapter.

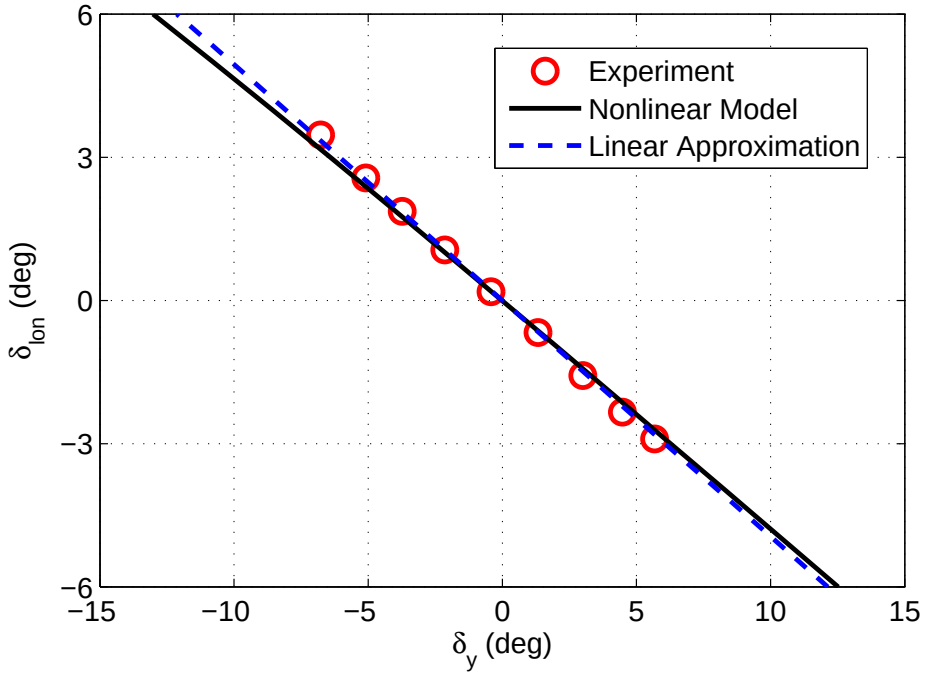

Figure 4.9: Experimental results of the longitudinal cyclic pitch versus swashplate orientation and comparison to the nonlinear model and linear approximation.

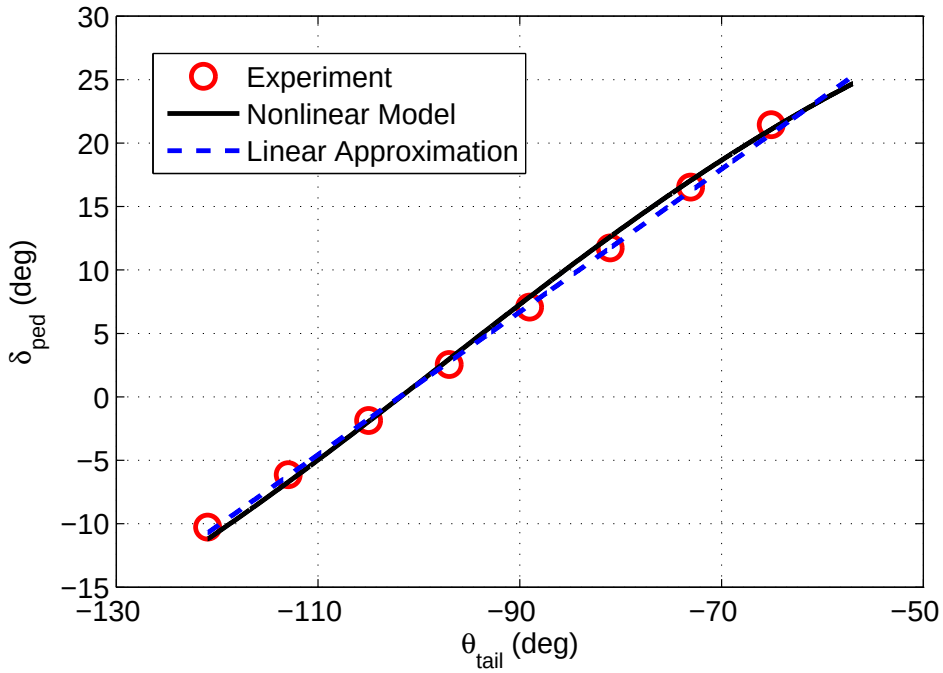

Figure 4.10: Experimental results of the tail blade pitch versus tail servo arm input and comparison to the nonlinear model and linear approximation.

Chapter 5

System Identification and Model Validation using Ground and Flight Test Data[1]

System identification is often used for small-scale helicopters to extract a mathematical model or the parameters of an existing model using experimental data. The two main approaches used in the system identification technique are: time-domain and frequency-domain identification.

Frequency-domain identification is used to derive linear models and is suitable for the systems whose dynamics can be represented by a transfer function. Comprehensive Identification from FrEquency Response (CIFER) is used for the identification of a small-scale Yamaha R-50 [41]. First, the flight data is collected using frequency sweeps applied one at a time to each control input while the others are used to maintain the helicopter in hover or cruise flight. Then, the frequency response for each input-output pair is computed and conditioned to remove the effect of secondary inputs. Finally, by solving an optimization problem a state-space model whose frequency response matches the flight data is extracted and validated in the time-domain.

MOdeling for flight Simulation and Control Analysis (MOSCA) is another frequency-domain identification tool for the identification of a small-scale CMU

[1] A version of this chapter has been published in [29] and submitted for publication in [33].

R-50 helicopter [40]. MOSCA combines first-principles and system identification techniques and uses optimization methods in the frequency-domain to obtain both linear and nonlinear helicopter models. A 30-state nonlinear helicopter model is linearized around multiple operating points and MOSCA is used to extract the frequency responses. Then, these frequency responses for each input-output pair are computed using numerous flight data. Finally, by minimizing a weighted cost function of the mismatch between the corresponding frequency responses at various operating points, the parameters of the nonlinear model are estimated.

The time-domain identification method is another approach which is suitable for both linear and nonlinear systems and can be used to estimate unknown parameters of a nonlinear model. A time-domain identification approach is used in [44] to identify the model parameters of a Hirobo-90 small-scale helicopter. In this approach, first the nonlinear model is linearized around hover and its state-space representation is derived. Then, flight data is collected around hover and the parameters of the linearized model is estimated using the Levenberg-Marquardt (LM) method [45].

Another time-domain identification approach is presented in [46] for a small-size Ikarus ECO helicopter. System identification is performed on a SISO basis using four different test stands to isolate the fuselage motion into a set of decoupled SISO systems. First, the nonlinear model of the helicopter is linearized around hover and a transfer function for each DOF is computed. Then, the input-output data is collected for different DOFs by flying the helicopter on the stands. Direct least squares method is then used to estimate the parameters of the transfer functions.

Most system identification approaches in the literature are based on the linearized helicopter dynamics around some operating points [44, 46, 47, 48, 49]. This restricts the application of these approaches to linear control methods. In

this work, a system identification strategy to estimate parameters of the nonlinear model in Eq. (3.38) using the data from the ground and flight tests is carried out on the Evolution-EX helicopter. To validate this model in the time-domain, flight data is used as described next.

Some parameters such as the mass, moment of inertia, air density, rotor speed, gear ratios, size of the components, etc are measured directly. The remaining parameters are found using a time-domain system identification technique that is suitable for nonlinear models. Actual physical parameters of the main and tail rotor blades such as the lift curve slopes and zero lift drag coefficients are determined using the ground test data from an aerodynamic force measurement testbed. This testbed is specially designed to measure the forces and moments generated by the rotors of small-scale helicopters around hover. The rest of the parameters including those of the rotor dynamics and empennage drag are estimated using the flight test data. The system identification strategy is described in the next section.

5.1 Identification using Ground Test Data

To determine the lift and drag coefficients of the main and tail rotors including C_{L_0}, C_{L_α}, C_{D_0}, $C_{L\alpha_{tr}}$ and $C_{D0_{tr}}$, an aerodynamic force measurement testbed as shown in Figure 5.1 was developed. The setup is designed for small-scale unmanned helicopters to emulate hover flight conditions and measure the aerodynamic forces and moments generated by the main and tail rotors around hover [29].

The testbed has a 1.8 m main pole to minimize the ground effect of the main rotor. To mount the helicopter on the testbed, an interface mechanism composed of a set of three adjustable plates is used as shown in Figure 5.2. The plates can

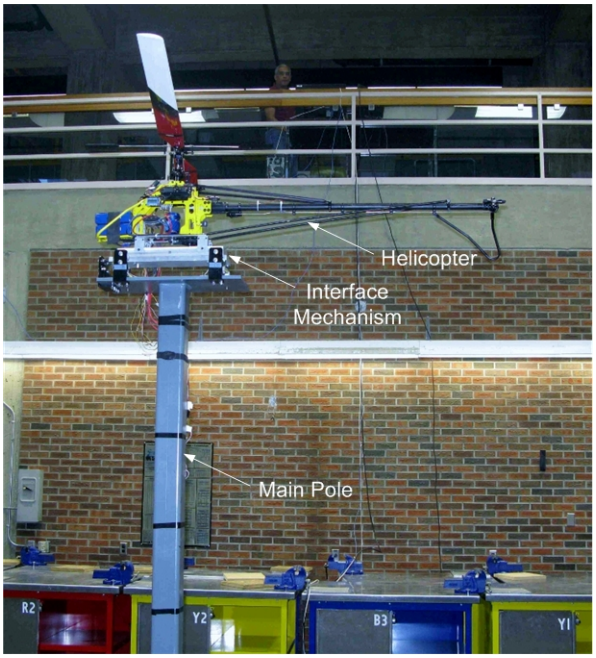

Figure 5.1: Aerodynamic force measurement testbed around hover.

slide with respect to each other to allow for an easy alignment of the CG with respect to the main pole. After the position of the CG is adjusted, the plates and the helicopter are bolted to each other to form a rigid system. This rigid system is connected to an upper frame of the pole through eight load cells attached to the three perpendicular faces of the plates. The eight load cells can measure all the forces and moments applied by the helicopter fuselage to the testbed.

A ground station computer running the xPC Target real-time kernel, commands the helicopter servos and collects the data from the load cells using a PCI-6602 National Instrument data acquisition card at the sampling frequency of 100 Hz. Using the ground data from applying different collective commands to the servos of the helicopter and measuring the corresponding aerodynamic forces and moments through the load cells, the lift and drag coefficients of the main and tail rotors can be estimated.

To determine the lift and drag coefficients of the main rotor, a flight scenario

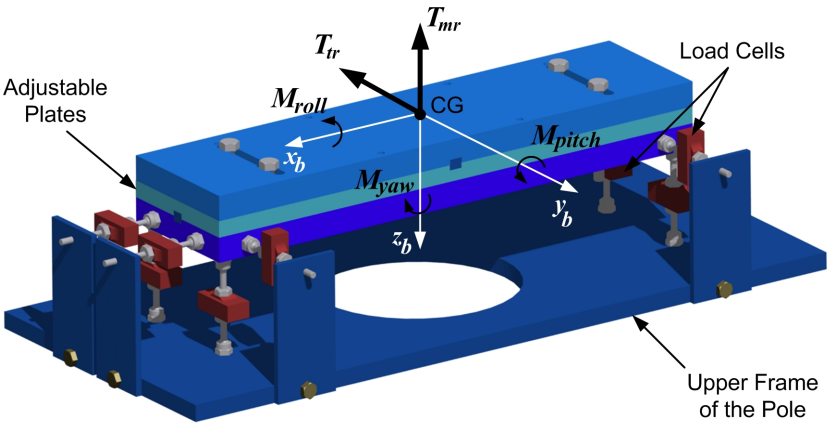

Figure 5.2: Schematic of the testbed interface assembly.

is designed to emulate hover flight conditions at different thrust loadings. The tail blades are detached throughout this test so that the main rotor drag torque required for the estimation of the drag coefficient is measured at the same time. In this test, the cyclic pitch is fixed to zero and the collective pitch increases from 0 to 8.4 degrees in increments of 1.2 degrees and the corresponding force measurements are collected.

Since the helicopter is fixed on the testbed throughout the tests, velocity components of the fuselage are zero and the main rotor thrust in Eq. (3.18) is:

$$\underbrace{T_{mr}}_{Y} = \underbrace{\frac{1}{6}\rho\pi R_{mr}^4\Omega^2\sigma_{mr}\left[1 \quad \left(\delta_{col} - \frac{3}{2}\lambda_0\right)\right]}_{X}\underbrace{\begin{bmatrix} C_{L_0} \\ C_{L_\alpha} \end{bmatrix}}_{\beta} \tag{5.1}$$

Since the thrust in Eq. (5.1) is linear with respect to the lift coefficients, a linear least squares method is used to identify the unknown coefficients, C_{L_0} and C_{L_α}, using:

$$\beta = (X^T X)^{-1} X^T Y \tag{5.2}$$

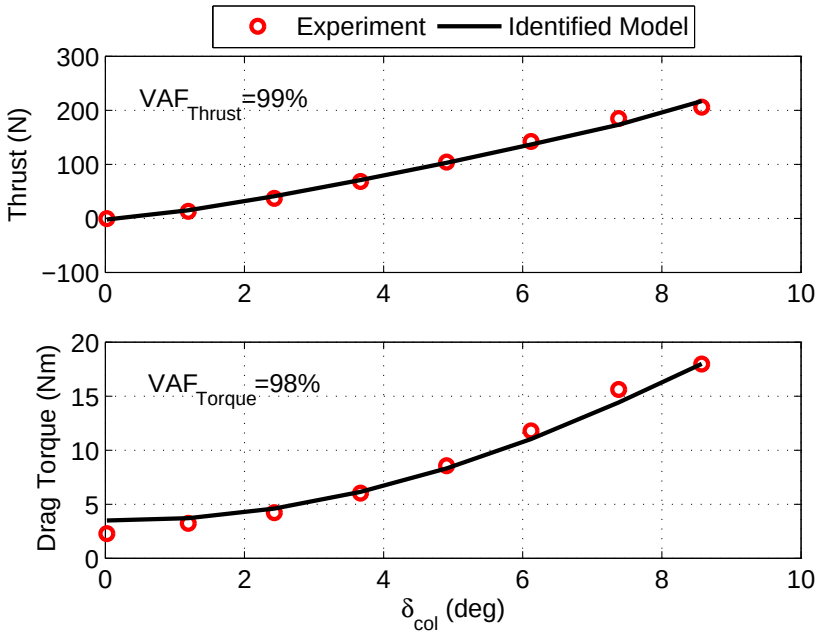

Figure 5.3: Main rotor thrust and drag torque vs. collective input under these conditions: $\Omega = 1100$ rpm; $R_{mr} = 0.95$ m; $\rho = 1.107$ kg/m^3; $\sigma_{mr} = 0.06$.

The lift coefficients obtained for the Evolution-EX helicopter are $C_{L_0} = 0.0077$ and $C_{L_\alpha} = 5.496$ rad^{-1}. As was expected, the estimated value of the zero lift coefficient C_{L_0}, is very small due to the symmetrical airfoil profile of the main rotor blades.

Repeating the above identification process for the drag torque model in Eq. (3.23), the zero lift drag coefficient of the main rotor C_{D_0} is estimated and listed in Table 5.1.

A comparison between the experimental data and the predicted response of the identified models is shown in Figure 5.3. A "VAF" index value representing a measure of the quality of the output generated by the identified model is calculated using the variance accounted for (VAF) index [56], as:

$$\text{VAF} = \left(1 - \frac{\text{var}(y - \hat{y})}{\text{var}(y)}\right) \times 100\% \tag{5.3}$$

where y is the measured output (experimental data) and $\hat{y}$ is the predicted output. The VAF indices of the thrust and drag torque shown in Figure 5.3 are 99% and 98%, respectively, indicating an excellent match between the predicted model of the thrust and drag torque and the experimental data in hover. Note that each point on the shown graphs corresponds to a quasi-steady hover condition. For example, the 4.8 deg collective pitch and 100 N thrust corresponds to the hover condition for the helicopter with a mass of 10.19 kg, while, the 8.4 deg collective pitch and 200 N thrust corresponds to the hover condition for the helicopter with a mass of 20.38 kg. The induced velocity required for the identification process in Eq. (5.2) is found for each point using the induced velocity formula at hover as:

$$V_h = \sqrt{\frac{T_{mr}}{2\rho\pi R_{mr}^2}} \tag{5.4}$$

It is also shown in Figure 5.3 that the thrust and drag torque of the main rotor both change with the collective pitch in a nonlinear manner. The reason is that the inflow ratio of the main rotor, λ_0, is not constant and changes with the thrust in a nonlinear manner itself. For example, increasing the collective pitch in Eq. (5.1) increases the thrust in a nonlinear manner, because, it also increases the induced velocity of the rotor in Eq. (5.4), which results in a partial decrease of the angle of attack and the thrust value. Similar approach can be used to show that the drag torque in Eq. (3.23) changes with the collective pitch in a nonlinear manner. Also, the drag torque of the main rotor versus the thrust is shown in Figure 5.4. The results indicate that the drag torque of the main rotor varies with the thrust in a nonlinear manner.

To identify the lift and drag coefficients of the tail rotor $C_{L\alpha_{tr}}$ and $C_{D0_{tr}}$, the main rotor blades are removed and the tail rotor blades are attached. Then, the

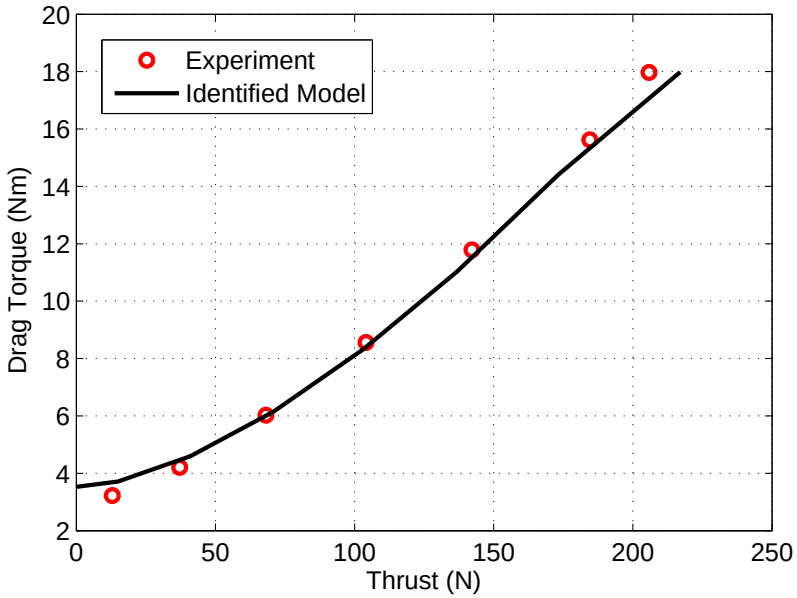

Figure 5.4: Main rotor drag torque vs. thrust under these conditions: $\Omega = 1100$ rpm; $R_{mr} = 0.95$ m; $\rho = 1.107$ kg/m^3; $\sigma_{mr} = 0.06$.

data sets are collected and the above identification process is repeated for the tail rotor thrust and drag torque models in Eqs. (3.28) and (3.29), respectively. The estimated coefficients of the tail rotor obtained from Eq. (5.2) are listed in Table 5.1. The experimental data and predicted response of the tail rotor thrust and drag torque models are compared in Figure 5.5 and VAF indices of above 90% are obtained indicating that a good match between the predicted models and the experimental data is achieved.

5.2 Identification using Flight Test Data

To identify the unknown parameters of the rotor dynamics and empennage drag in Eq. (3.38), the data from real flight tests using the Evolution-EX small-scale helicopter are used.

The mathematical model of the helicopter in Eq. (3.38), is nonlinear with respect to the model parameters as well as the states. Therefore, a time-domain

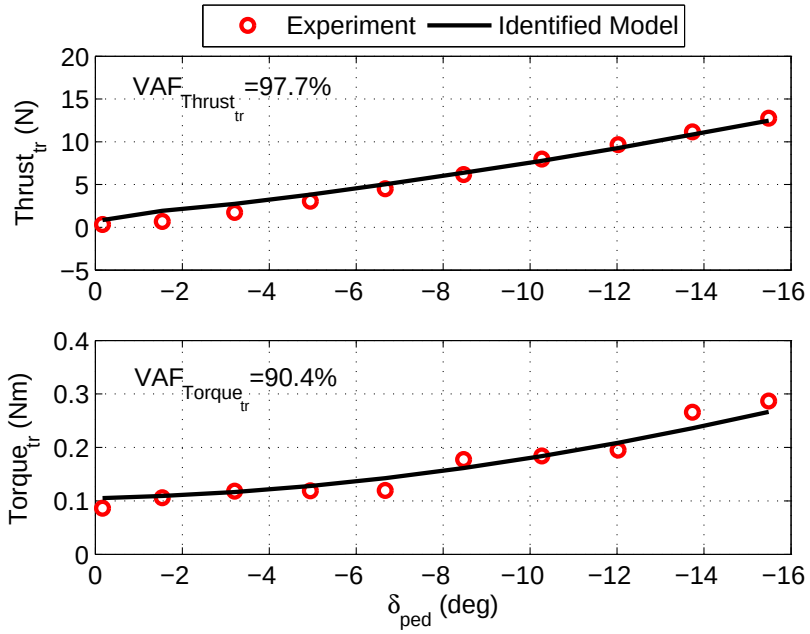

Figure 5.5: Tail rotor thrust and drag torque vs. pedal input under these conditions: $\Omega_{tr} = 6600$ rpm; $R_{tr} = 0.15$ m; $\sigma_{tr} = 0.11$.

system identification technique based on the nonlinear least squares method is used. This is an optimization technique in which the measured outputs, y, from the flight tests are compared with the predicted outputs, $\hat{y}$, from the simulation of the helicopter model in Eq. (3.38) and the model parameters are chosen to minimize prediction errors using the following cost function:

$$J_i = \sum_{j=1}^{M} \sum_{k=1}^{N} E_j^2(k), \quad i = 1 \; to \; P \tag{5.5}$$

where $E_j(k) = y_j - \hat{y}_j$, N is the number of data samples, M is the number of outputs and P is the number of iterations.

The identification process includes the following steps:

1. Data Collection: Flight maneuvers are performed on the Evolution-EX helicopter by a ground pilot using a radio transmitter to excite the dynamic modes of interest and input-output flight data with a sufficient length is

collected. The pilot commands to the servos are recorded in pulse width modulation (PWM) using an onboard servo switch card (SSC) module and converted to the real angles through offline kinematic calculations of the Bell-Hiller mixer. The measurements of all the states of the helicopter are collected using the Crossbow IMU module at a sampling frequency of 20 Hz. Then, the input-output data set is assembled. The states that do not determine the dynamic response of the system such as the position data from GPS are not used in the identification process. Only the states of the dynamic equations such as the angular rates and velocities of the helicopter CG are used as the output variables in Eq. (5.5) to identify the unknown parameters of the system.

2. State-Space Model Representation: The state-space representation of the helicopter nonlinear model in Eq. (3.38) is used. Initial values of the states and the parameters, as well as the upper and lower bounds of the unknown parameters are defined.

3. Parameter Estimation: The unknown parameters of the model are identified in this step using an iterative prediction-error minimization technique. To do this, the state-space model of the helicopter is integrated using the recorded inputs from the flight tests and initial guess values of the parameters, and the outputs are predicted at every time step. Then, the cost function, J, Eq. (5.5), is calculated at the end of the simulation and the parameter values are updated using the Trust-Region-Reflective algorithm [55]. This is repeated in an iterative process until the cost function is minimized and becomes smaller than the termination tolerance.

4. Data Comparison: Finally, the predicted outputs are compared with the measured outputs and a "VAF" index value is calculated using Eq. 5.3.

Since the helicopter is an unstable system, it is difficult to design a single maneuver to properly excite all different modes at the same time and have the pilot maintain stability of the vehicle. Therefore, to estimate the parameters of interest, different flight maneuvers are used to excite dynamic modes of the helicopter. This sequential identification process has the following steps which are outlined in the next sections.

5.2.1 Roll and Pitch Identification

To identify the unknown parameters of the rotor dynamics including K_β, K_{lon}, K_{lat}, τ_f, τ_s, A_b, B_A and K_s in Eqs. (3.6) to (3.11) a roll and pitch identification process is used. Since, the pitch and roll dynamics are coupled, identification of these parameters are performed simultaneously to get a more accurate prediction result.

To properly excite the roll and pitch dynamics of the helicopter, input commands shown in Figure 5.6 are applied. These input commands contain low to high frequencies as well as small to full cyclic excitations. To apply these maneuvers, the helicopter is first brought to hover. Then, the pilot starts exciting the pitch dynamics while maintaining the roll, heave and heading approximately constant. This is followed by another maneuver to excite the roll dynamics and maintain the other three constant.

After the flight data is collected, the lift and drag coefficients of the main and tail rotors obtained in the previous sections are updated. Then, the identification steps 2 to 4 (section 5.2) are applied on the data and the unknown parameters are estimated. The output variables, y_j, in Eq. (5.5), used in this step to identify the unknown parameters of the rotor dynamics, are the roll and pitch rates, p and q, and the state variables are: $p, q, \phi, \theta, a_1, b_1, c_1$ and d_1. The actual and predicted responses from this identification process are shown in Figure 5.6. The

VAF indices of the pitch and roll identified models shown in this Figure are 97.9% and 94.9%, respectively, indicating that an excellent match between the predicted model and the flight data is achieved with the estimated parameters.

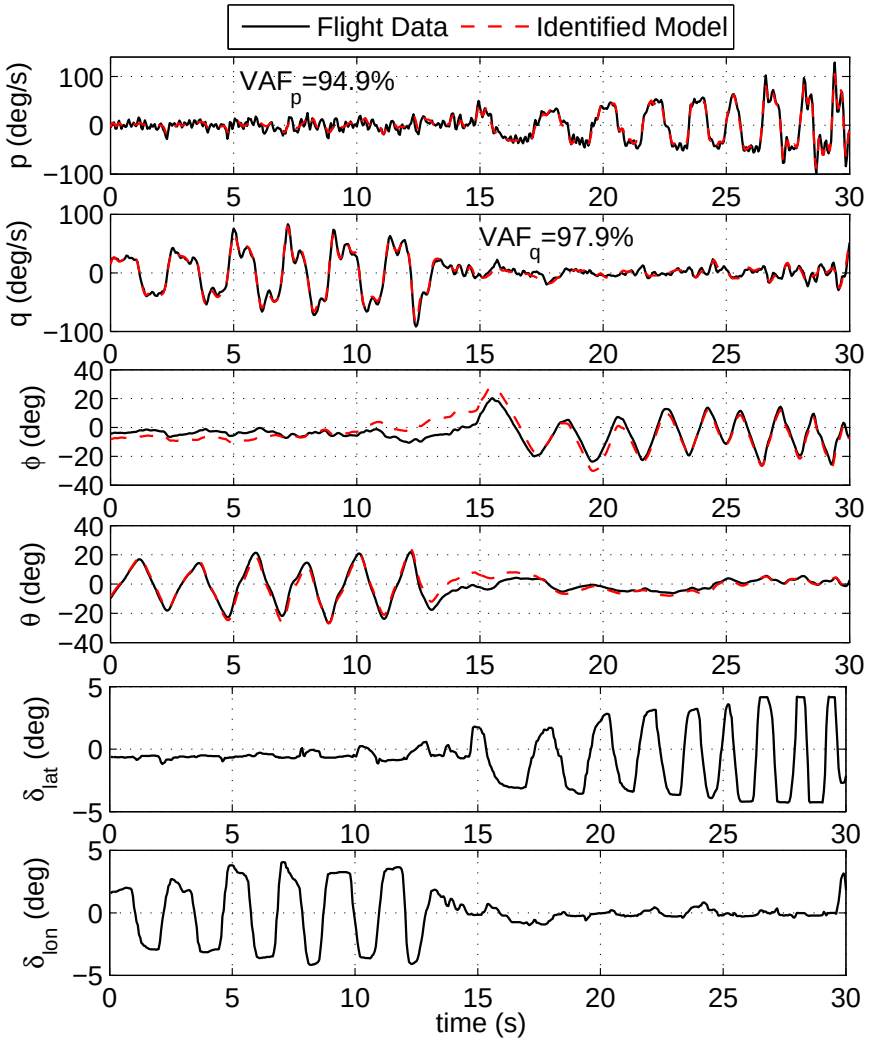

Figure 5.6: Actual and predicted roll and pitch responses and input excitations under these conditions: $\Omega = 1100$ rpm; $\rho = 1.107$ kg/m^3 (identification).

The above process is repeated using experimental tests from different roll and pitch maneuvers and parameter estimations corresponding to the highest VAF indices are chosen and listed in Table 5.1. The responses shown in Figure 5.6 are based on the selected parameter values which result in the highest VAF indices.

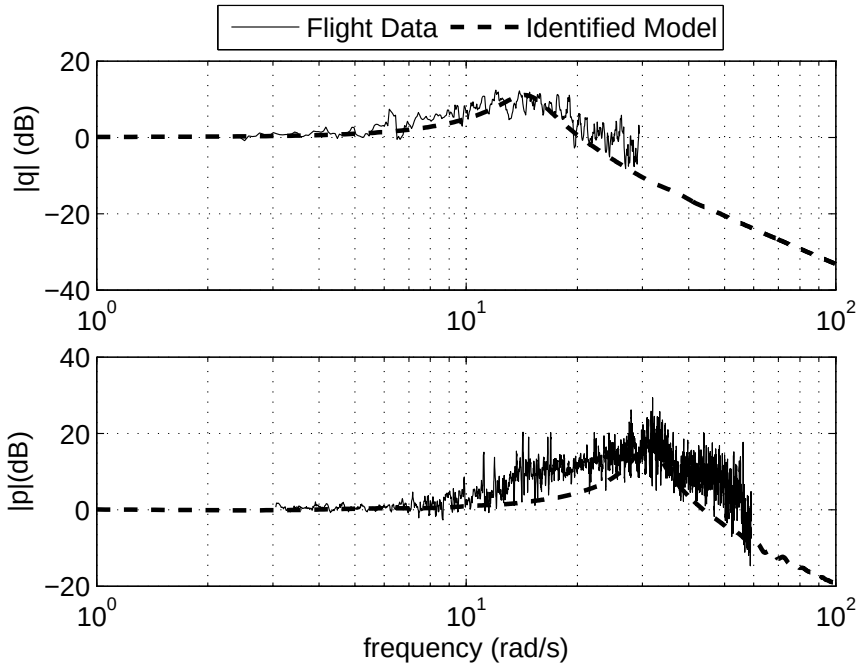

Figure 5.7: Frequency response comparison between the simulation and real flight test of the normalized pitch and roll rate responses at the sample rate of 20 Hz.

The frequency responses of the roll and pitch motion are compared in Figure 5.7 for the Evolution-EX helicopter. They show the magnitude of the normalized amplitude ratio of the roll and pitch rates to the lateral and longitudinal cyclic inputs respectively, which could be used as an alternative way to identify the f-r dynamics as mentioned earlier in this chapter. Figure 5.7 shows that the identified model properly matches the flight data in the frequency-domain. Note that the noise in the magnitude plots in Figure 5.7 is due to low signal-to-noise ratio as a result of the effects of the secondary inputs and thrust variations. These effects are often removed (conditioned) in the frequency-domain identification methods such as CIFER [41].

5.2.2 Yaw Identification

To identify the unknown parameters of the vertical tail and main rotor downwash on the tail rotor including $C_{L_\alpha}^{vt}$, S_{vt}, and K_λ, a yaw identification process is used. In this process, pedal step inputs are applied to excite the yaw dynamics such that the helicopter goes under a full clockwise (CW) turn followed by a full counter clockwise turn as shown in Figure 5.8.

Similar to the roll and pitch process, first, the parameters obtained from the previous identification processes are updated and then the identification steps 1 to 4 (section 5.2) are applied and the unknown parameters of the yaw motion are estimated. The actual and predicted responses for the yaw rate and yaw angle are shown in Figure 5.8. The VAF index for this identification process is 91.9%, which shows a good match between the predicted model and the actual flight data for the yaw dynamics. The estimated parameters from the yaw identification are listed in Table 5.1.

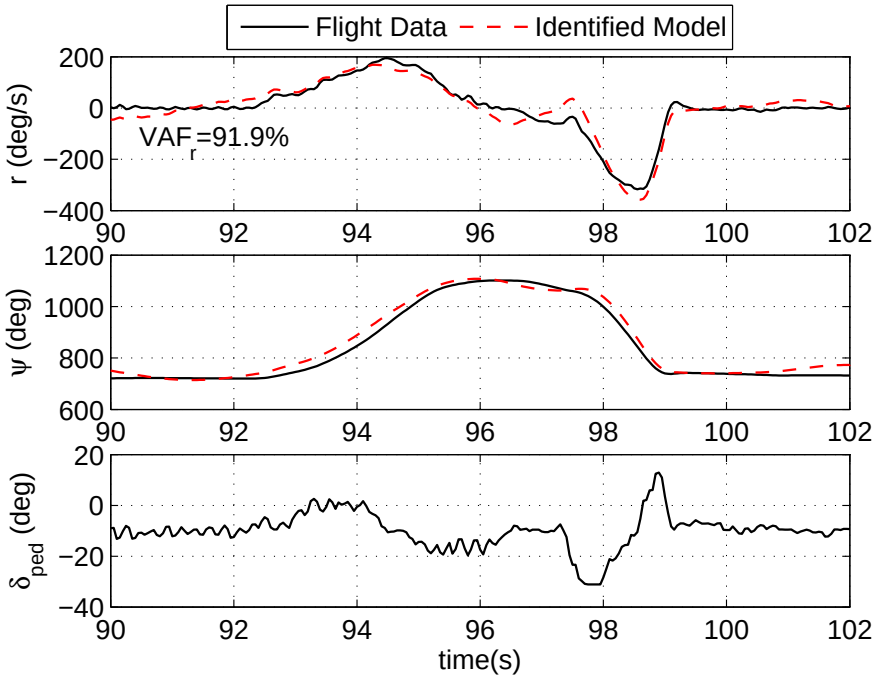

Figure 5.8: Actual and predicted yaw response under these conditions: Ω = 1100 rpm; $\rho = 1.107$ kg/m^3 (identification).

5.2.3 Heave Identification

To identify the unknown parameters of the horizontal tail as well as the fuselage drag along the z-axis including S_{ht}, $C^{ht}_{L_\alpha}$ and S^{fus}_z, a heave identification process is used. In this process, two consecutive step inputs with 9 deg and 10.3 deg collective pitch angles are applied to excite the heave dynamics as shown in Figure 5.9.

Similar to the previous processes, the identification steps 1 to 4 are used and the unknown parameters of the heave motion are estimated. The actual and predicted responses for the vertical velocity and altitude are shown in Figure 5.9. The VAF index for this identification process is 90.9%, indicating a good match between the predicted model and the actual flight data on the heave dynamics. Note that the Evolution-EX helicopter does not have a horizontal or vertical tail,

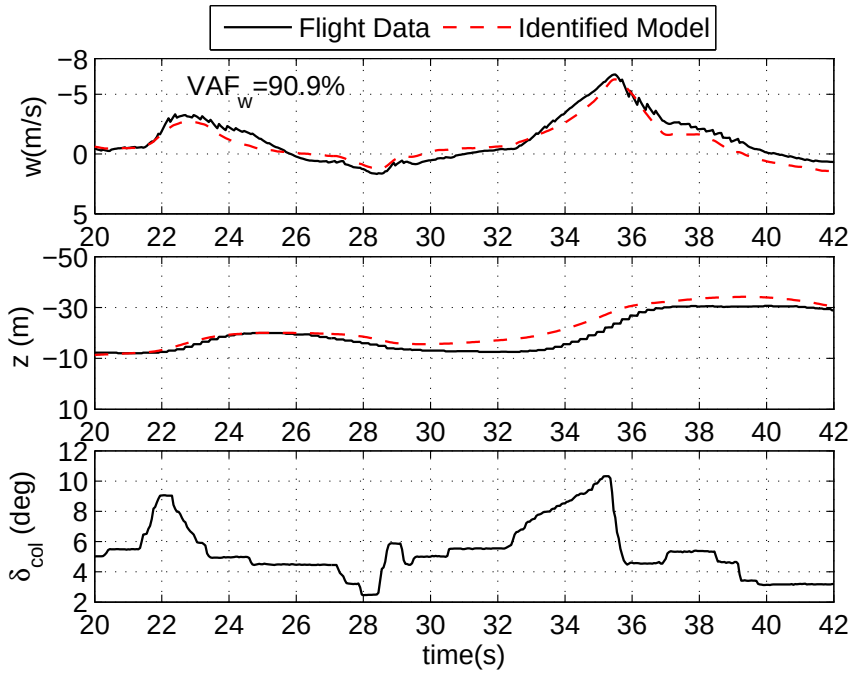

Figure 5.9: Actual and predicted heave response under these conditions: Ω = 1100 rpm; $\rho = 1.107$ kg/m^3 (Identification).

so these parameters are absent in Table 5.1.

5.2.4 Longitudinal and Lateral Velocity Identification

To identify the remaining unknown parameters of the fuselage drag including the frontal and side fuselage area coefficients S_x^{fus} and S_y^{fus}, a longitudinal and lateral velocity identification process is used. To see the effects of the fuselage drag and estimate the above parameters, the helicopter is flown in a circular path A as shown in Figure 5.10 reaching a longitudinal and lateral velocities above 10 m/s. The data from the flight path B is used for the validation in the next section.

The actual and predicted responses of helicopter longitudinal and lateral velocities as well as the position of the CG in the inertial frame are shown in Figure 5.11. The VAF indices for this identification process are 97.2% and 93% for the longitudinal and lateral velocities, respectively, indicating a good match

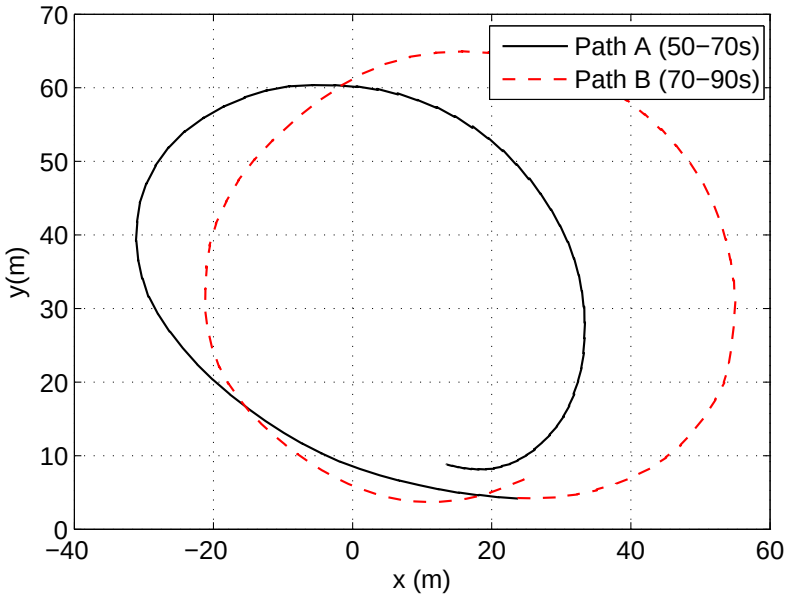

Figure 5.10: Flight paths used for the longitudinal and lateral velocity identification and validation.

between the predicted model and the actual flight data.

5.3 Model Validation

The identification strategy described in the previous section results in all the model parameters of the helicopter dynamics in Eq. (3.38) being identified. In the following, totally different data sets which were not used in the identification process are used to excite the roll, pitch, yaw, and heave dynamics of the helicopter and cross validate the model.

5.3.1 Roll and Pitch Validation

To validate the roll and pitch dynamics, new flight data, not used in the identification process, is used. The roll and pitch responses are shown in Figures 5.12 and 5.13. The VAF indices in these figures show that the helicopter dynamics in

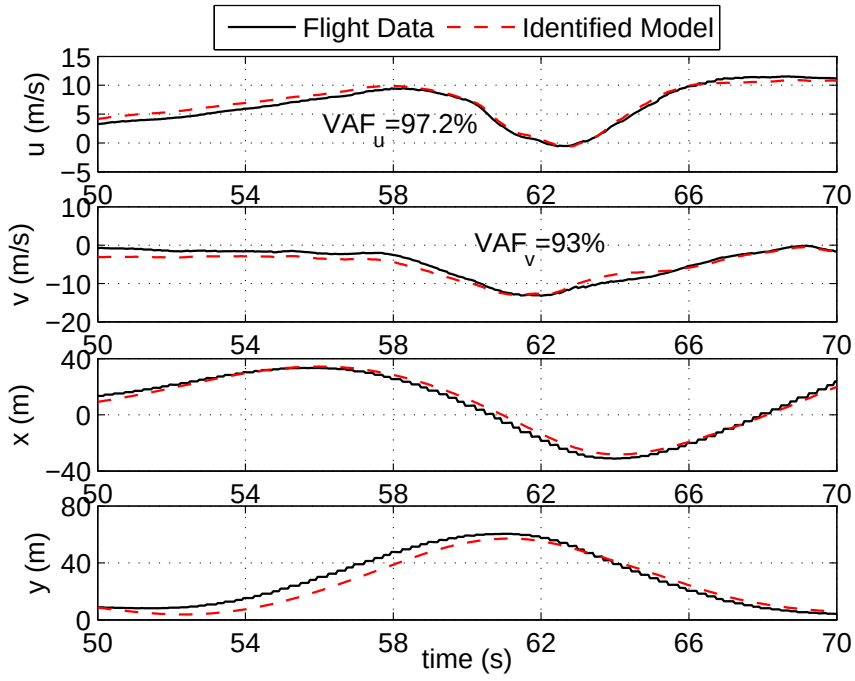

Figure 5.11: Actual and predicted longitudinal and lateral velocity responses on the circular path A under these conditions: $\Omega = 1100$ rpm; $\rho = 1.107$ kg/m^3 (Identification).

Eq. (3.38) accurately represent the roll and pitch dynamics of the helicopter.

5.3.2 Yaw Validation

To validate the yaw dynamics of the helicopter, data shown in Figures 5.14 and 5.15 are used. Figure 5.14 shows a sinusoidal excitation and the flat peaks in the command signal are due to the pedal input saturations. This saturation can cause the system to go unstable and must be taken into account in the design of the controller. A pedal step excitation is shown in Figure 5.15, which results in almost a full yaw turn. The yaw response and VAF index show that the helicopter dynamics in Eq. (3.38) accurately represent the yaw dynamics of the helicopter.

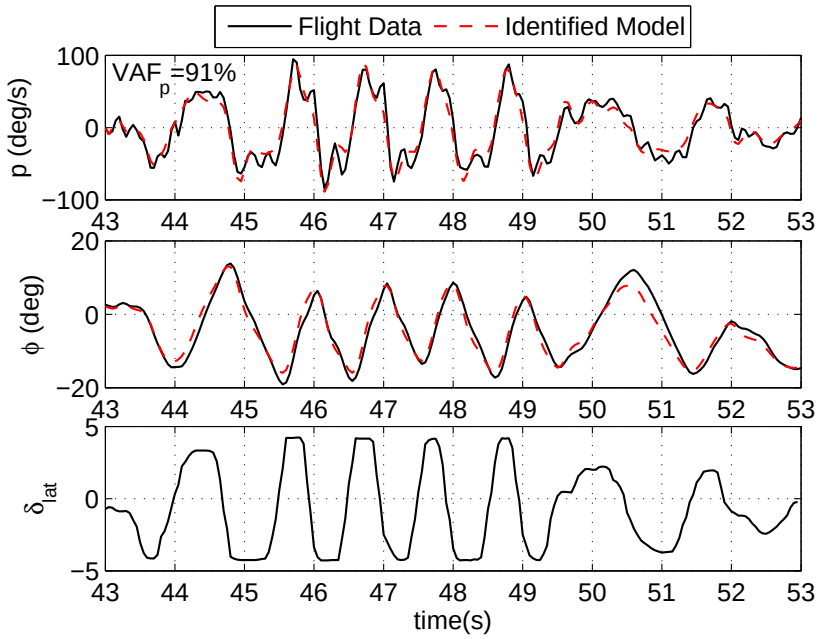

Figure 5.12: Actual and predicted roll response (Validation).

5.3.3 Heave Validation

The data sets shown in Figures 5.16 to 5.18 are used to validate the heave dynamics. A low-speed vertical descent is shown in Figure 5.16, which is known to be difficult to model due to the formation of an unsteady flow regime. A low-speed and a high-speed vertical climb maneuvers are also shown in Figures 5.17 and 5.18, respectively. The VAF indices in these figures show that the helicopter dynamics in Eq. (3.38) accurately represent the actual heave dynamics of the helicopter.

Note that the lower VAF values in the validation graphs for the heave dynamics could be due to the low accuracy of the vertical velocity measurements typically found in IMUs with a regular GPS receiver. This is due to the fact that the vertical velocity is not directly measured, but obtained through integration of the data from the accelerometers in the IMU and correction of the integration

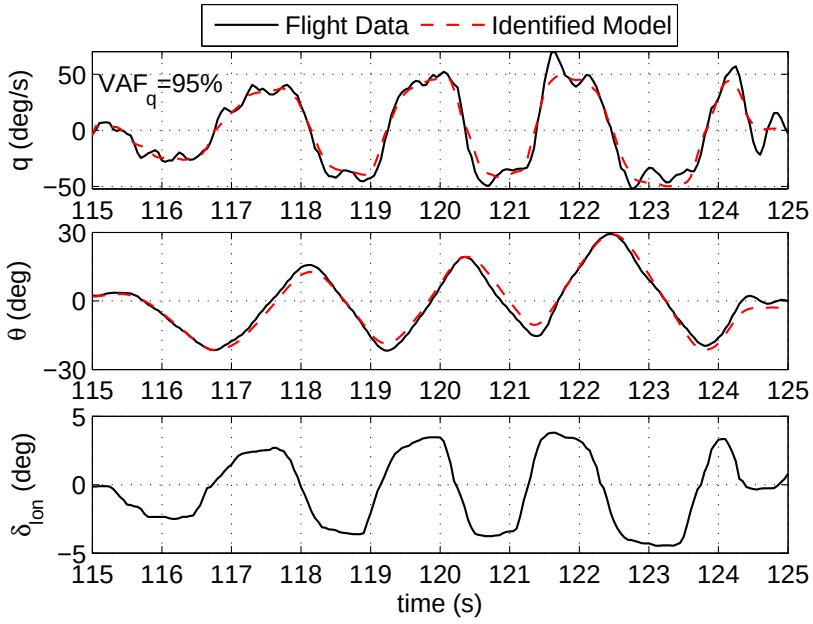

Figure 5.13: Actual and predicted pitch response (Validation).

drift using the GPS data. Therefore, the low accuracy of the altitude measurements typically found in most regular GPS receivers, results in a low accuracy in the heave velocity measurements.

5.3.4 Longitudinal and Lateral Velocity Validation

To validate the longitudinal and lateral velocity dynamics of the helicopter, data sets from the circular flight path B, shown in Figure 5.10 is used. Figure 5.19 shows the longitudinal and lateral velocity responses corresponding to this flight path.

The VAF indices in Figure 5.19 show that the helicopter dynamics in Eq. (3.49) also accurately represent the longitudinal and lateral velocity dynamics of the helicopter.

The above results show that the overall response of the nonlinear model of the helicopter dynamics has a good agreement with the real flight data. Consequently,

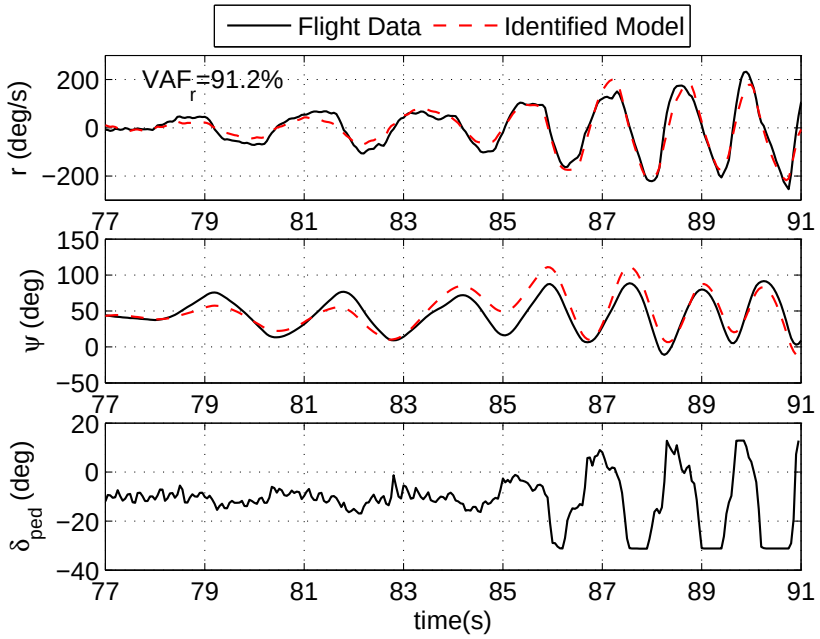

Figure 5.14: Actual and predicted yaw response (Validation).

the derived square control-affine model of the helicopter dynamics can be used for the control design.

5.4 Comparison of the Rotational Dynamic Models using the Flight Test Data

The rotational dynamics of the helicopter modeled based on the hybrid model approach in Eq. (3.38) is compared with the one modeled based on the first-principles approach in Eq. (3.78) using the flight test data.

The unknown parameters of the rotational dynamic model in Eq. (3.78) which are identified using the roll and pitch identification procedure are reduced to the rate and input derivatives of the stabilizer bar: α_1 and α_2. Similarly, input commands shown in Figure 5.6 are used and identification steps 1 to 4 are applied to find these parameters. The identification results are shown in Figure 5.20,

Table 5.1: Identified parameters of the Evolution-EX helicopter.

Parameter	**Value**	**Description**
m [kg]	11.5	Helicopter and avionics mass
ρ [kg/m^3]	1.107	Air density
c_{mr} [m]	0.082	Main rotor chord
c_{tr} [m]	0.025	Tail rotor chord
R_{mr} [m]	0.95	Main rotor radius
R_{tr} [m]	0.15	Tail rotor radius
Ω [rad/s]	115	Nominal main rotor speed
n_{tr} [−]	6.0	Gear ratio of tail rotor to main rotor
I_{xx} [kg m^2]	0.3	Rolling moment of inertia
I_{yy} [kg m^2]	1.6	Pitching moment of inertia
I_{zz} [kg m^2]	2.0	Yawing moment of inertia
z_{cg} [m]	−0.32	Main rotor hub height from CG
x_{fus} [m]	−1.22	Tail rotor hub offset from CG along x-axis
d [m]	3.0	Control point height from the main rotor hub
α_1 [−]	53	stabilizer bar rate derivative
α_2 [−]	55	stabilizer bar input derivative
α_{tail} [rad/s]	-1698.5	slope of the tail servo angle to the PW of the signal
C_{L_0} [−]	0.008	Main rotor blade zero lift curve slope
$C_{L\alpha}$ [rad^{-1}]	5.49	Main rotor blade lift curve slope
$C_{L\alpha_{tr}}$ [rad^{-1}]	4.95	Tail rotor blade lift curve slope
C_{D0} [−]	0.01	Main rotor blade zero lift drag coefficient
$C_{D0_{tr}}$ [−]	0.06	Tail rotor zero lift drag coefficient
$\delta_{0_{tail}}$ [rad]	1.4724	y-intercept of the tail servo angle to the PW of the signal
K_β [N m]	255	Hub torsional stiffness
K_{lon} [−]	1.0	Longitudinal cyclic to longitudinal flap gain
K_{lat} [−]	0.98	Lateral cyclic to lateral flap gain
τ_f [sec]	0.04	Main rotor time-constant of the rotor
τ_s [sec]	0.2	Stabilizer bar time-constant of the rotor
$\theta_{0_{tail}}$ [rad]	0.1169	zero pitch angle of the tail blade
A_b [−]	-0.1	Lateral flapping cross-coupling derivative
B_A [−]	0.1	Longitudinal flapping cross-coupling derivative
K_s [−]	0.3	Stabilizer bar to rotor flap gain
K_λ [−]	1.0	Main rotor downwash factor at fuselage
S_x^{fus} [m^2]	0.1	Frontal fuselage area
S_y^{fus} [m^2]	0.83	Side fuselage area
S_z^{fus} [m^2]	0.51	Vertical fuselage area

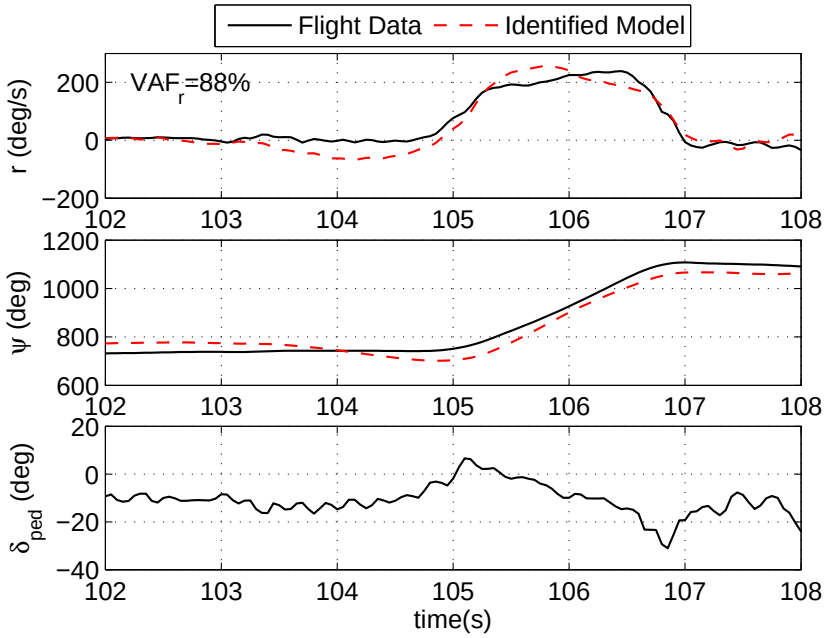

Figure 5.15: Actual and predicted yaw response (Validation).

indicating that a good match between the predicted model and the flight data is achieved.

To validate the model in Eq. (3.78), the flight test data shown in Figs. 5.21 and 5.22 are used. The VAF indices in these figures show that the helicopter dynamics in Eq. (3.78) accurately represents the roll and pitch dynamics of the helicopter.

The helicopter dynamics based on the first-principles approach in Eq. (3.78) is simpler and requires fewer unknown parameters to be identified compared to the one obtained using the hybrid model approach in Eq. (3.38), so its system identification is easier. On the other hand, a comparison between the results of the roll and pitch responses in Figures 5.6, 5.12 and 5.13, and Figures 5.20 to 5.22 based on the VAF indices, shows that the hybrid model approach more accurately represents the rotational dynamics of the helicopter. This is due to

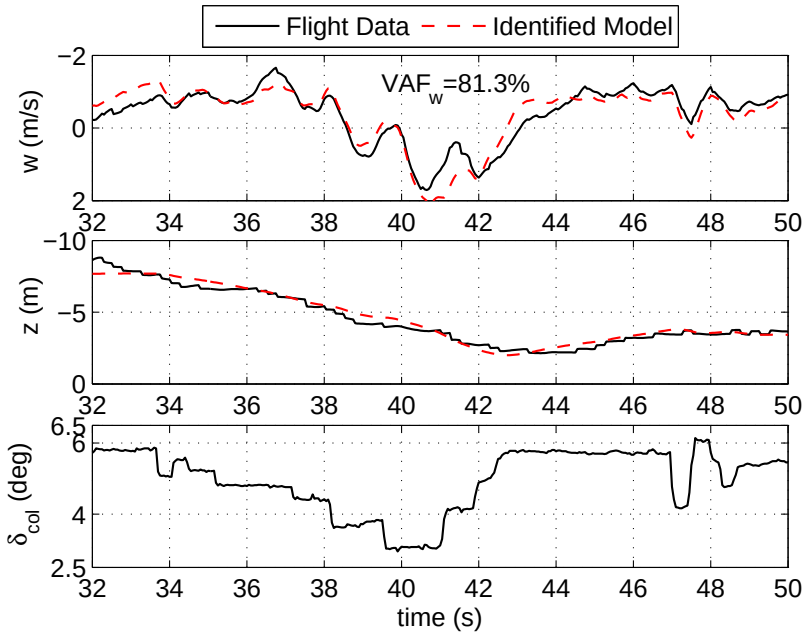

Figure 5.16: Actual and simulated heave response in a low-speed vertical descent (Validation).

the fact that the first-principles approach does not account for the effects of the rotor flapping. Therefore, the helicopter dynamics in Eq. (3.53), which is based on the hybrid model approach, will be used for the control design in Chapter 6.

5.5 Summary

A time-domain system identification strategy is used to identify the parameters of the nonlinear model of the helicopter using a combination of ground and flight test data. The ground test data is used to determine the lift and drag coefficients of the main and tail rotors using an aerodynamic force measurement testbed especially designed for small-scale unmanned helicopters to emulate hover flight conditions. Then, the unknown parameters of the rotor dynamics and empennage drag are identified using piloted flight test data. A nonlinear least squares method is used to find the parameters based on a sequential identification process. The model is cross validated using different flight data sets not used in the identification

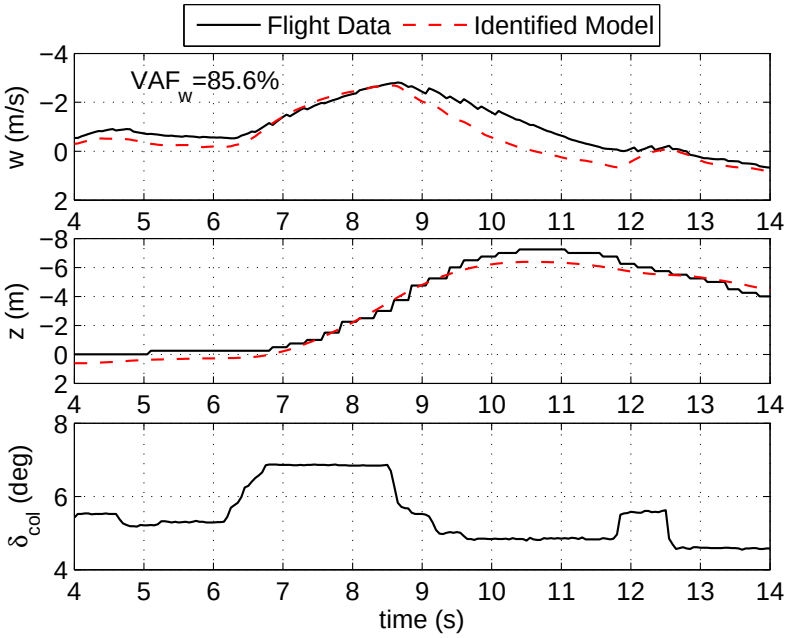

Figure 5.17: Actual and simulated heave response in a low-speed vertical climb (Validation).

process indicating that the overall response of the obtained nonlinear model of the helicopter matches the real flight data. The responses of the roll and pitch motion are also compared in the frequency-domain showing a good match between the identified model and the flight data in the frequency-domain as well. Moreover, the Rotational Dynamic Models based on the hybrid model and first-principles approaches are compared using the flight test data. This validated model is used in a robust control design next in Chapter 6.

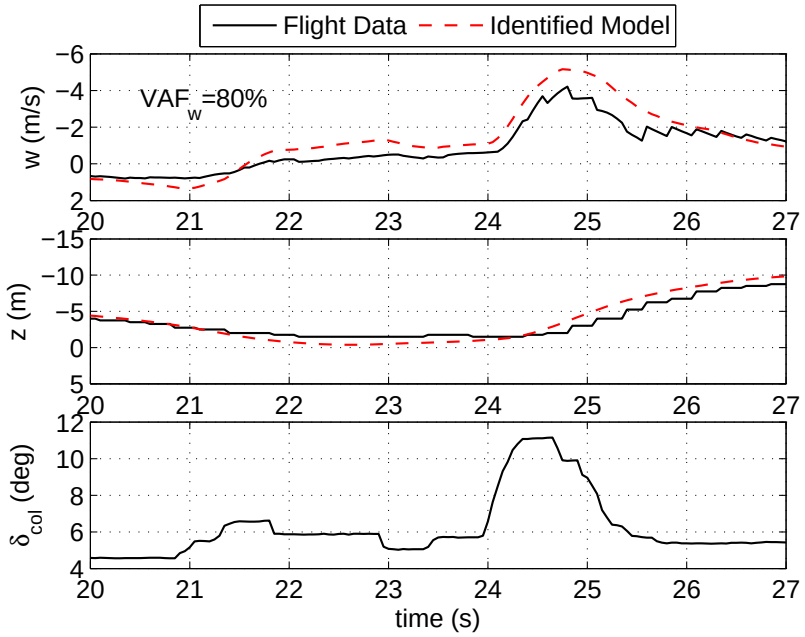

Figure 5.18: Actual and simulated heave response in a high-speed vertical climb (Validation).

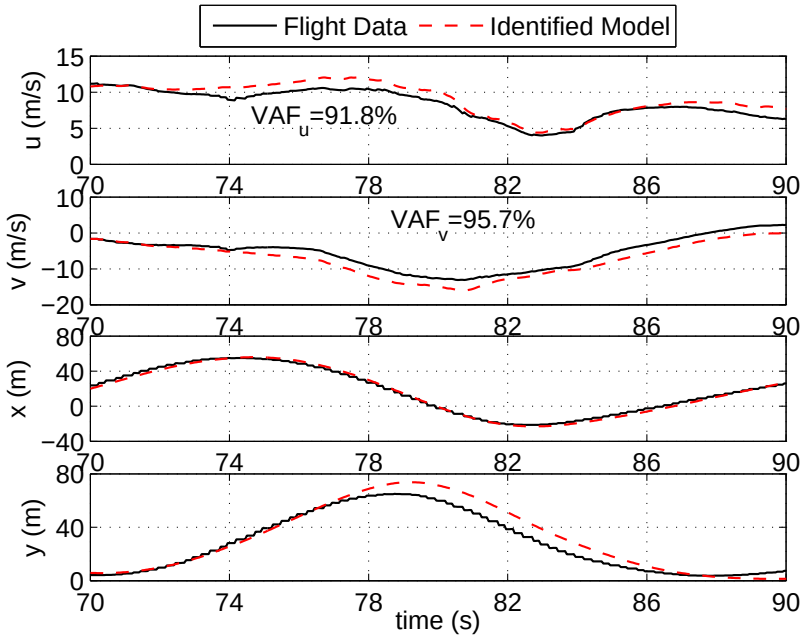

Figure 5.19: Actual and predicted longitudinal and lateral velocity responses on the circular flight path B (Validation).

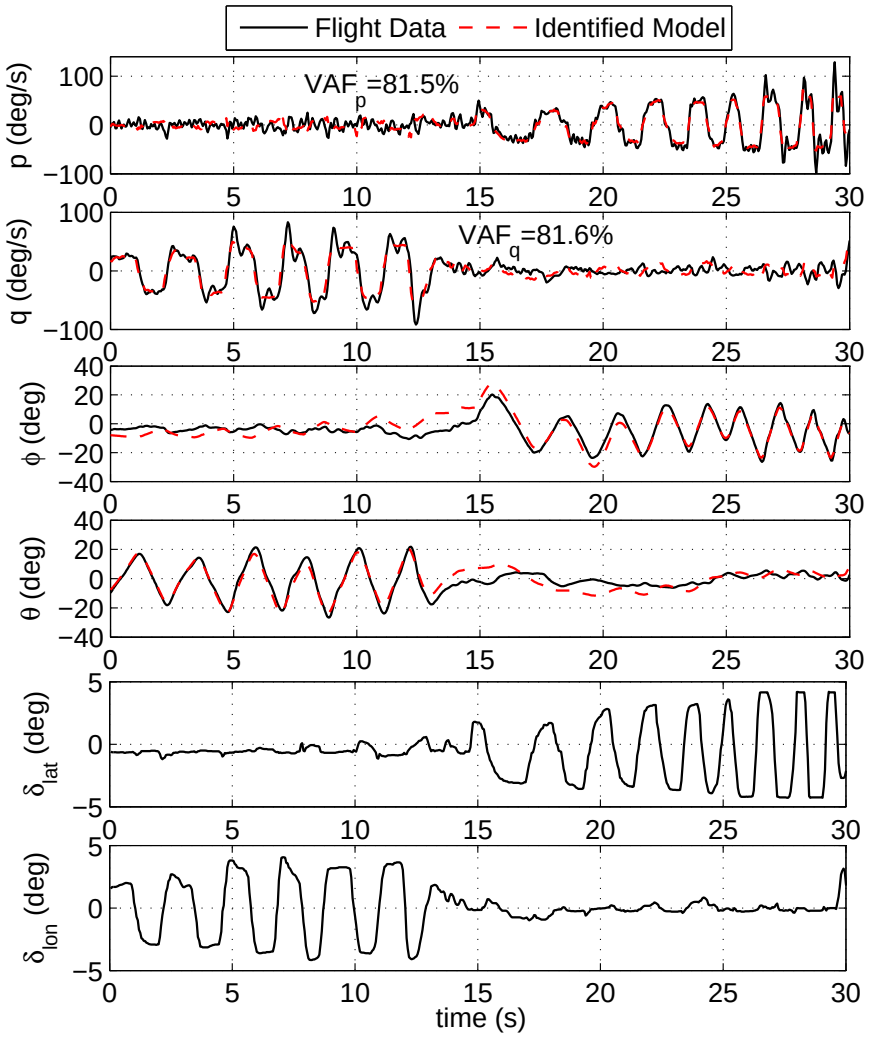

Figure 5.20: Actual and predicted roll and pitch responses and input excitations (identification).

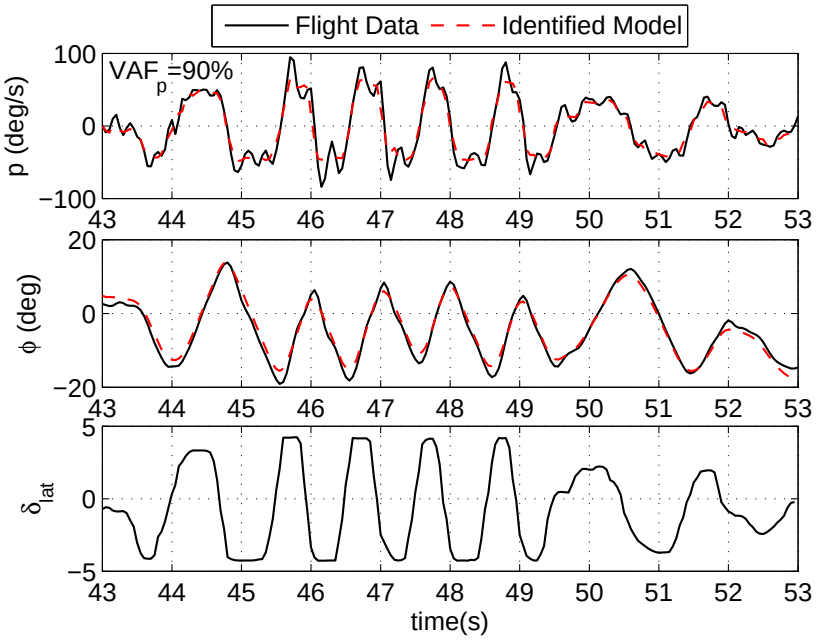

Figure 5.21: Actual and predicted roll response(Validation).

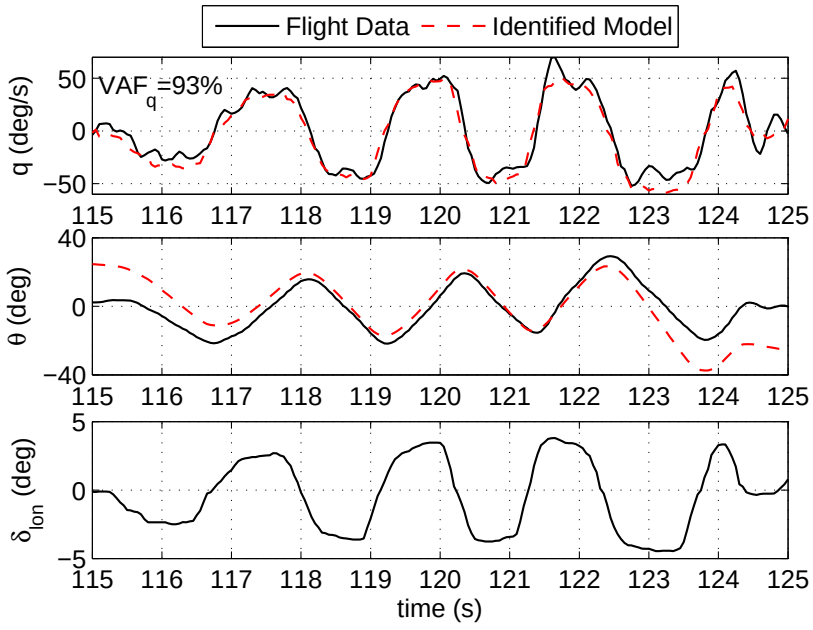

Figure 5.22: Actual and predicted pitch response (Validation).

Chapter 6

Nonlinear Control Design using Sliding Mode Control (SMC)[1]

6.1 Control Design

The new formulation in Eq. (3.53) makes possible the application of any nonlinear MIMO control methods that need the dynamic model of the helicopter in a square and affine-in-control input-output form. To demonstrate the application of this formulation in control of small-scale helicopters, a sliding mode control method is used as an example. The reason for choosing SMC is that helicopters are characterized with significant uncertainties due to the complicated aerodynamics of the rotor. In addition, these vehicles are inherently unstable and have a nonlinear dynamics with multiple inputs and outputs. The SMC algorithm is a useful candidate for the control of small-scale unmanned helicopters due to its robustness to the bounded uncertainties and model mismatches as well as guaranteed closed-loop stability and capability to deal with MIMO nonlinear systems.

Typically, a linearized model of the helicopter and a multi-loop control approach are used to design the SMC for small-scale helicopters [21, 22, 23, 24]. The SMC algorithm only works for the systems with dynamics represented by a

[1] A version of this chapter has been submitted for publication in [31].

square and affine-in-control formulation. The underactuated nonlinear helicopter dynamics is converted into the square affine-in-control input-output formulation in Eq. (3.53). This new formulation allows for the application of SMC using the nonlinear model of the helicopter for better performance in a wider range of flight regimes compared to a linearized model. A robust control design, based on the nonlinear model of the helicopter dynamics obtained in the previous section, is described next.

Sliding Mode Control (SMC)

The SMC design method in this section follows [18]. The obtained square control-affine input-output formulation of the helicopter dynamics in Eq. (3.53) is used:

$$\ddot{\mathbf{y}}_{4\times1} = \mathbf{g}(\boldsymbol{y}, \dot{\boldsymbol{y}})_{4\times1} + \mathbf{c}(\boldsymbol{y}, \dot{\boldsymbol{y}})_{4\times4}\mathbf{u}_{4\times1} \tag{6.1}$$

To design a sliding mode controller, four asymptotically stable equations in the state-space are defined:

$$\boldsymbol{s} = \dot{\boldsymbol{e}} + \boldsymbol{\lambda}\, \boldsymbol{e} = \mathbf{0} \tag{6.2}$$

where $\boldsymbol{s}$ is the surface function, $\boldsymbol{e} = \boldsymbol{y} - \boldsymbol{y}^d$ is the error of the control output from its desired value, and $\boldsymbol{\lambda} = \text{diag}_{4\times4}(\lambda_1, \lambda_2, \lambda_3, \lambda_4)$, with all the components to be strictly positive, is the convergence rate. Rewriting Eq. (6.2) in the following form:

$$\boldsymbol{s} = \dot{\boldsymbol{y}} - \boldsymbol{s_r} \tag{6.3}$$

where $\boldsymbol{s_r} = \dot{\boldsymbol{y}}^d - \boldsymbol{\lambda e}$. Since, the surface defined by Eq. (6.2) is asymptotically stable, if the system is controlled such that $\boldsymbol{s}$ reaches zero and stays at zero at

all times, the output error $\boldsymbol{e}$, will exponentially converge to zero. In order for $\boldsymbol{s}$ to be zero, the following Lyapunov candidate function is defined:

$$V = \frac{1}{2}\boldsymbol{s}^T\boldsymbol{s} \tag{6.4}$$

In order for $\dot{V} \leq 0$, the control input is calculated as:

$$\boldsymbol{u} = \hat{\boldsymbol{c}}^{-1}(-\hat{\boldsymbol{g}} + \dot{\boldsymbol{s}}_{\boldsymbol{r}} - \boldsymbol{K}sat(\boldsymbol{\Phi^{-1}s})) \tag{6.5}$$

where $\boldsymbol{K} = \text{diag}_{4\times4}(k_1, k_2, k_3, k_4)$ is the sliding mode control gain matrix, and $\hat{\boldsymbol{c}}$ and $\hat{\boldsymbol{g}}$ are the system matrices calculated using nominal values of the model parameters. To avoid chattering a continuous saturation function with a boundary layer thickness $\boldsymbol{\Phi}$ is used in Eq. (6.5) instead of a signum function and is defined as:

$$sat(\boldsymbol{\Phi^{-1}s}) = \begin{cases} 1 & \text{if} \quad s \geq \Phi \\ \boldsymbol{\Phi^{-1}s} & \text{if} \quad -\Phi < s < \Phi \\ -1 & \text{if} \quad s \leq -\Phi \end{cases} \tag{6.6}$$

Using the above saturation function results in a trade-off between tracking accuracy and robustness to bounded uncertainty [18].

In the absence of any model mismatch and uncertainties in Eq. (3.53), selection of any positive definite matrix $\boldsymbol{K}$ in Eq. (6.5) would result in the convergence of the error $\boldsymbol{e}$ to zero. The presence of external disturbances or parameter uncertainties requires the components of $\boldsymbol{K}$ to be large enough such that the following sliding condition is satisfied:

$$\dot{V} \leq -\boldsymbol{\eta}|\boldsymbol{s}| \tag{6.7}$$

where $\boldsymbol{\eta}$ has strictly positive components, and determines the convergence rate to the surface. This condition results in the following formula for the sliding control gain [18]:

$$(1-\Delta_{ii})k_i + \sum_{j\neq i}^{4}\Delta_{ij}k_j = G_i + \eta_i + \sum_{j=1}^{4}\Delta_{ij}|\dot{s}_{ri} - \hat{g}_j|,\ i = 1, ..., 4 \tag{6.8}$$

where, $\boldsymbol{G}$ and $\boldsymbol{\Delta}$ are the uncertainty bound matrices as:

$$|\boldsymbol{g} - \hat{\boldsymbol{g}}| \leq \boldsymbol{G} \tag{6.9}$$

$$\boldsymbol{c} = (\mathbf{I}_{4\times 4} + \boldsymbol{\delta})\hat{\boldsymbol{c}}, \quad |\boldsymbol{\delta}| \leq \boldsymbol{\Delta} \tag{6.10}$$

By knowing the uncertainty bounds $\boldsymbol{G}$ and $\boldsymbol{\Delta}$ and solving Eq. (6.8) for K_i's at every time step, it is guaranteed that the control outputs will converge to their desired trajectories.

6.2 Simulations

In this section, the trajectory tracking performance of the designed SMC and its robustness to model parameter uncertainties is demonstrated through computer simulations. The model parameters are from the Evolution-EX small-scale helicopter found in Table 5.1.

In these simulations, the obtained square control-affine model of the helicopter in Eq. (3.53) is used for the control design, while the more complex model in Eq. (3.38) is used as the helicopter plant model and includes the stabilizer bar dynamics and unsimplified model of the rotor flapping in Eqs. (3.6) and (3.7).

6.2.1 Figure-8 Trajectory Tracking with Parameter Uncertainties

The test trajectory is a three dimensional figure-8 shown in Figure 6.1, in which the helicopter is initially at rest at the position of $(x_p, y_p, z_p) = (10, -5, -100)$ m, a point outside the desired trajectory, and transitions to the main trajectory at 20 s through a 6^{th}-order polynomial path. Then, the figure-8 maneuver is started and continues to 120 sec. Finally, the trajectory ends at the position (8, 0, -100) m through another 6^{th}-order polynomial path starting at 120 s and ending at 150 s and stays in hover until the end of the simulation time at 180 s.

To verify controller robustness, the moment of inertia tensor and the vehicle mass are allowed to differ by 20% from the model nominal values listed in Table 5.1. The following three cases of uncertainties in the mass and moments of inertia values are simulated:

1. 1.2 times the nominal values (20% uncertainty)
2. equal to the nominal values (0% uncertainty)
3. 0.8 times the nominal values (-20% uncertainty)

Note that the above uncertainties are only applied to the model parameters of the plant, while the controller uses the original nominal values of the parameters and is unaware of the uncertainties.

In these simulations, the height of the control point d, is selected to be 3 m above the CG and the rotor speed is 1100 rpm. Also, the control gains are listed in Table 6.1.

The three-dimensional paths of the helicopter's control point and center of gravity are shown in Figure 6.1 for all three cases. The observed offset along the

Table 6.1: Control gains obtained from the simulations.

Gain	Description	Longitudinal	Lateral	Heading	Heave
λ	*Convergence rate*	1	0.5	3	3
F	*Bound on f*	10	10	1	1
Δ	*Bound on b*	0.5	0.5	0.5	0.5
η	*Surface reach time*	1	1	1	1
Φ	*Boundary layer THK*	0.5	0.5	0.8	0.8

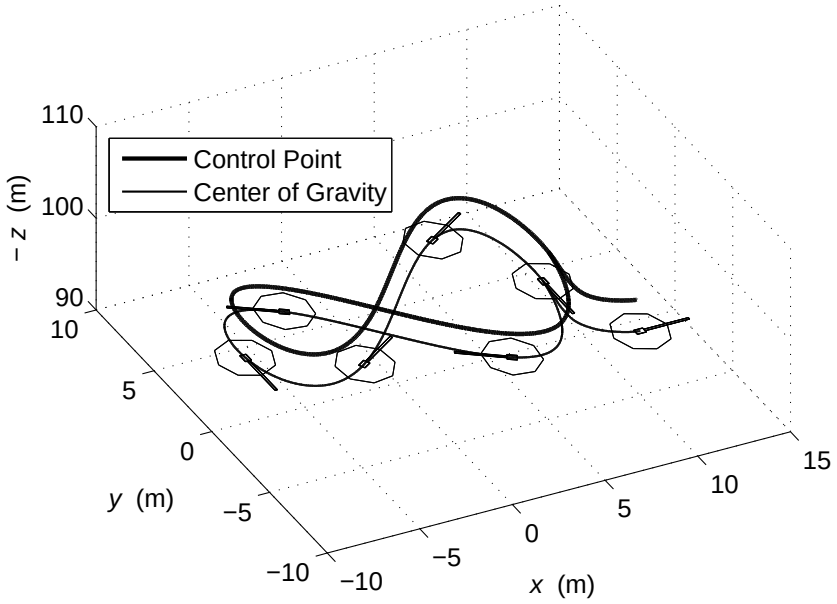

Figure 6.1: The trajectory of the CG and control point (figure-8 trajectory).

z-axis is due to the 3 m offset of the control point from the CG. All three cases are seen to coincide with the desired trajectory demonstrating the effectiveness of the controller in the presence of model parameter uncertainties. The helicopter icons are depicted at times 0, 20, 40, 60, 80, 100, 120, and 180 s. The icons for the times 20 and 180 s, correspond to the start and end points on the figure-8 path and overlap each other indicating that the controller has successfully accomplished the desired trajectory.

The control point position components and yaw angle of the helicopter are shown in Figure 6.2 indicating that the control outputs for all the three cases

coincide with the desired trajectories with negligible errors. Also, the tracking errors for these four control outputs are shown in Figure 6.3. The tracking results show that the controller successfully tracks the desired figure-8 trajectory with a mean absolute error of 0.18 m in the position of the control point and 0.08 deg in the yaw angle despite ±20% parameter variations. The errors could potentially be improved by further tuning of the control gains.

The control inputs are shown in Figure 6.4 and the controller has adjusted the magnitude of the required control inputs to compensate for the variations of the mass and moments of inertia from the nominal values. The magnitude of the collective pitch δ_{col}, is increased/decreased with the actual mass. The pedal input, δ_{tail}, which generates the counteracting torque to balance the main rotor drag torque is automatically adjusted to the changes in the collective pitch input. Moreover, the lateral and longitudinal inputs, δ_{lat} and δ_{lon}, are very small due to the negligible roll and pitch accelerations required for the desired maneuver, and they settle at their corresponding trim levels during hover (150 to 180 s).

As the helicopter is an underactuated system with 6-DOF and 4 inputs, satisfying the trajectory tracking requirements for the control outputs may not necessarily guarantee the stability of the helicopter. Since the control point is a point above the CG, the attitude of the helicopter could still have an oscillatory motion despite satisfactory performance of the control point. Therefore, the attitude states of the helicopter must also be monitored to assure the stability of the helicopter.

The roll, pitch and yaw Euler angles of the helicopter are shown in Figure 6.5, which shows that after the initial transient responses, the roll and pitch angles settle and reach constant angles in hover. This shows the stability of the heli-

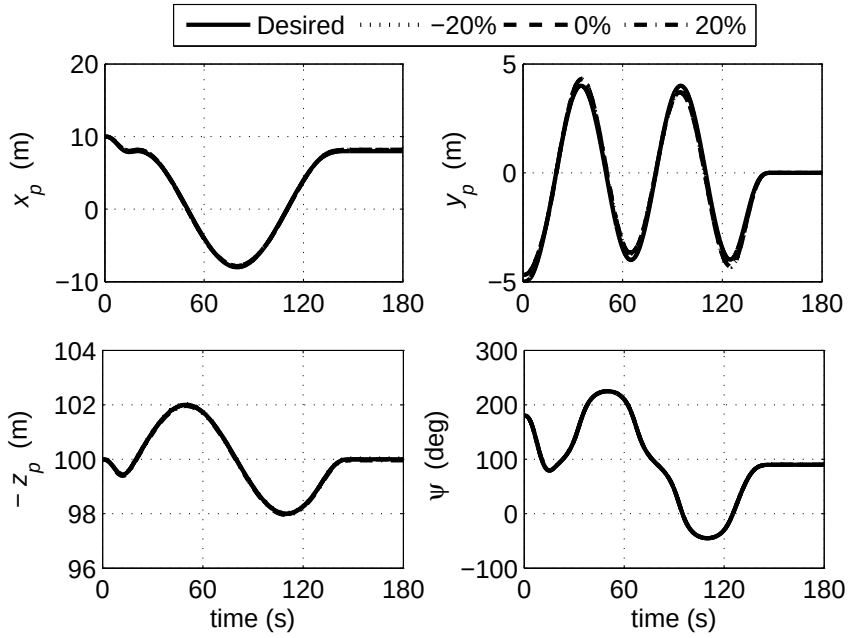

Figure 6.2: The position components of the control point and yaw angle (figure-8 trajectory).

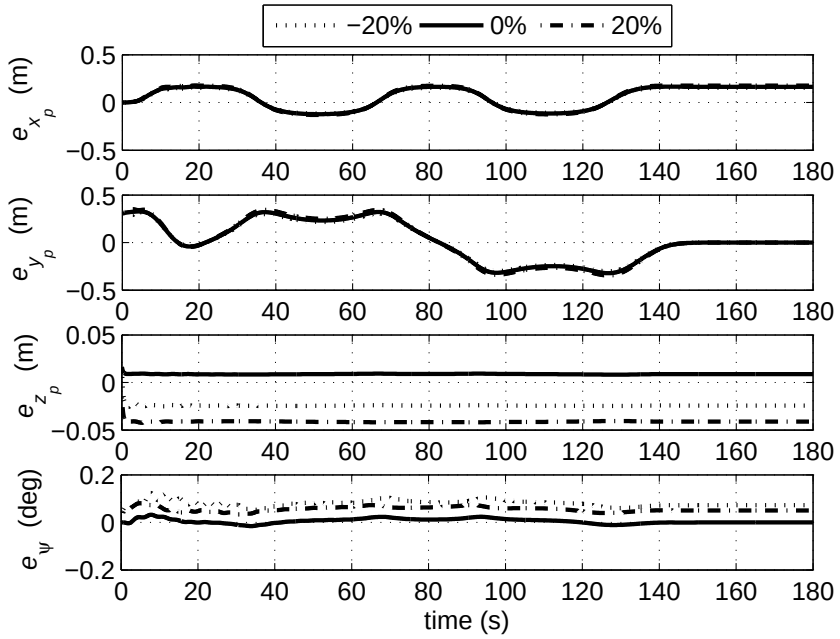

Figure 6.3: The error components of the control point position (figure-8 trajectory).

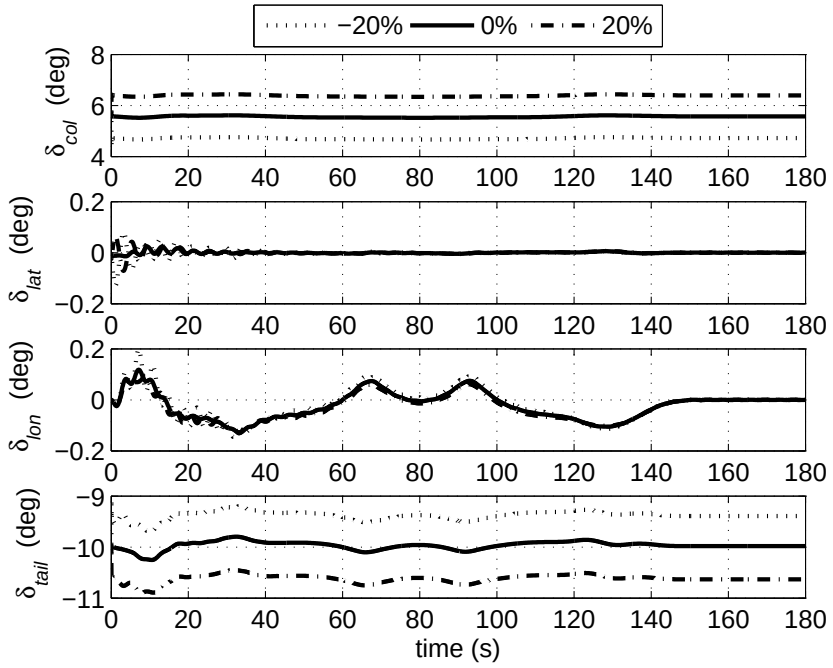

Figure 6.4: The control inputs: collective, longitudinal/latitude cyclic and pedal (figure-8 trajectory).

copter attitude while performing this maneuver for all the three cases. The roll and pitch angles are constant in hover. The helicopter in hover is tilted around its roll axis with a negative angle of about -6 deg to compensate for the positive lateral force by the tail rotor when the nominal parameter values are used. The roll tilt is slightly greater for the case with -20% nominal mass values and it is slightly lower for the case with 20% nominal mass values. This is because less thrust is generated by the main rotor to balance the helicopter with a lower mass. Therefore, more roll tilt is required to cancel out the tail rotor thrust. Also, since the desired forward speed is not constant in the designed trajectory, the roll and pitch angles are constantly changing along the path to maintain the control point on the desired trajectory all the time, until the helicopter reaches at hover at 150 s after which they settle to their corresponding constant angles at hover as shown in Figure 6.5. Also, the position of the helicopter's CG is shown

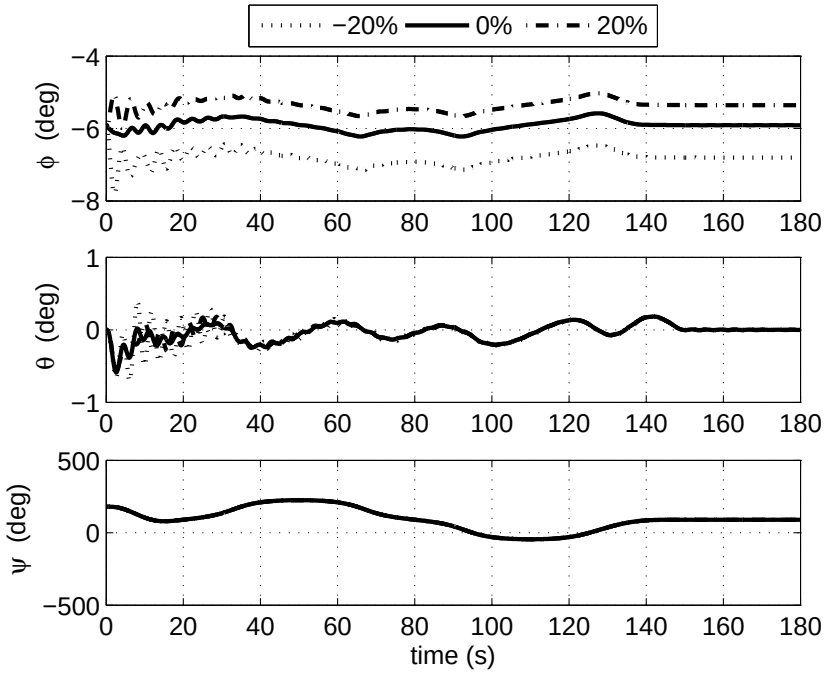

Figure 6.5: The attitude of the helicopter: roll, pitch and yaw Euler angles (figure-8 trajectory).

in Figure 6.6.

The simulated and desired trajectories closely match despite the 20% variations in the mass and moments of inertia parameters, showing that the SMC based on the square control-affine model of the helicopter is effective in the trajectory tracking of a complex three-dimensional figure-8 maneuver and is robust to these bounded uncertainties.

6.2.2 Circular Trajectory Tracking with Wind Disturbances

The trajectory tracking performance of the SMC subject to a wind disturbance is simulated in this section. The test trajectory is a forward turn maneuver shown in Figure 6.7, in which the helicopter is initially at rest at the position of $(x_{cp}, y_{cp}, z_{cp}) = (0, 0, -100)$ m, a point outside the desired circular trajectory, and hovers for 30 s. Then, it transitions to the main trajectory at 80 s through

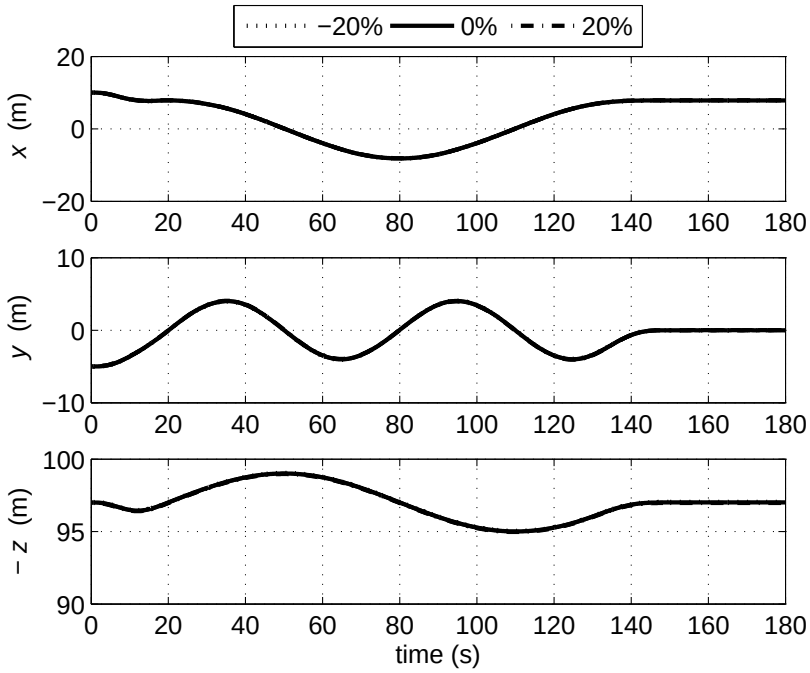

Figure 6.6: The position components of the helicopter CG (figure-8 trajectory).

a 5^{th}-order polynomial path. Next, the forward turn maneuver is started and continues to 200 s. Finally, the trajectory ends at the position (80, 0, -100) m through another 5^{th}-order polynomial path starting at 200 sec and ending at 250 s and stays in hover until the end of the simulation time at 300 s. The desired altitude of the helicopter's control point is 100 m throughout this simulation.

To verify controller robustness to external disturbances, a constant 4 m/s wind from the north-east is considered between 110-160 s as shown in Figure 6.7. The wind is only applied to the model of the plant and the controller is unaware of the wind. To do this, the components of the wind velocity vector are set to the corresponding values of the wind velocity only in the helicopter plant model in Eq. (3.38). Similar to the previous simulation, the control gains are listed in Table 6.1.

The path of the helicopter's control point is shown in Figure 6.7 and helicopter icons are depicted at times 0, 80, 110, 140, 170, 200 and 300 s. The icons of the

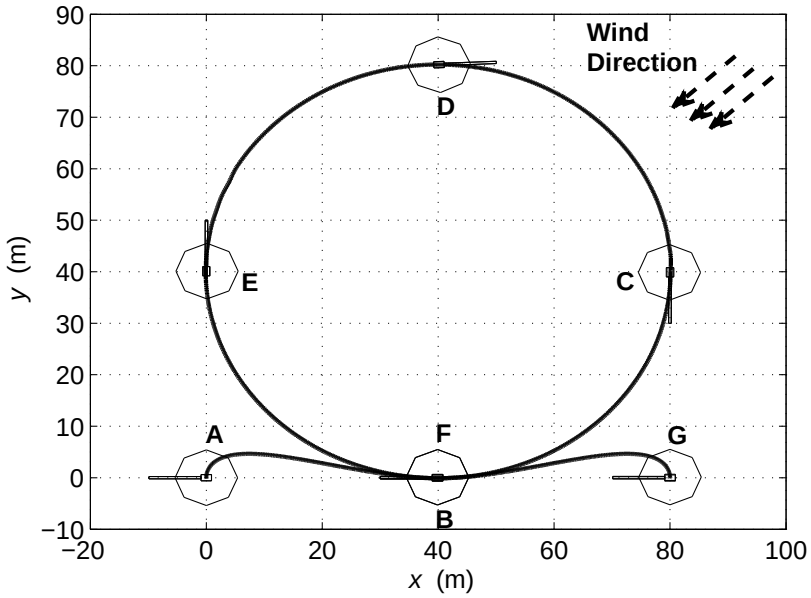

Figure 6.7: The trajectory of the CG and control point (circular trajectory).

times 80 and 200 s corresponding to the start point B and end point F on the circular path, overlap each other indicating that the controller has successfully accomplished the desired forward turn trajectory.

The control point position and yaw angle of the helicopter for the circular trajectory are shown in Figure 6.8 indicating that the control outputs coincide with the desired trajectories with negligible errors. Also, the tracking errors are shown in Figure 6.9. The tracking results show that the controller successfully tracks the desired circular trajectory with a mean absolute error of 0.17 m in the position of the control point and 0.4 deg in the yaw angle in the presence of wind disturbances. The errors could potentially be improved by further tuning of the control gains.

The Euler angles of the helicopter are shown in Figure 6.10, which again shows that after the initial transient responses, the roll and pitch angles settle and reach

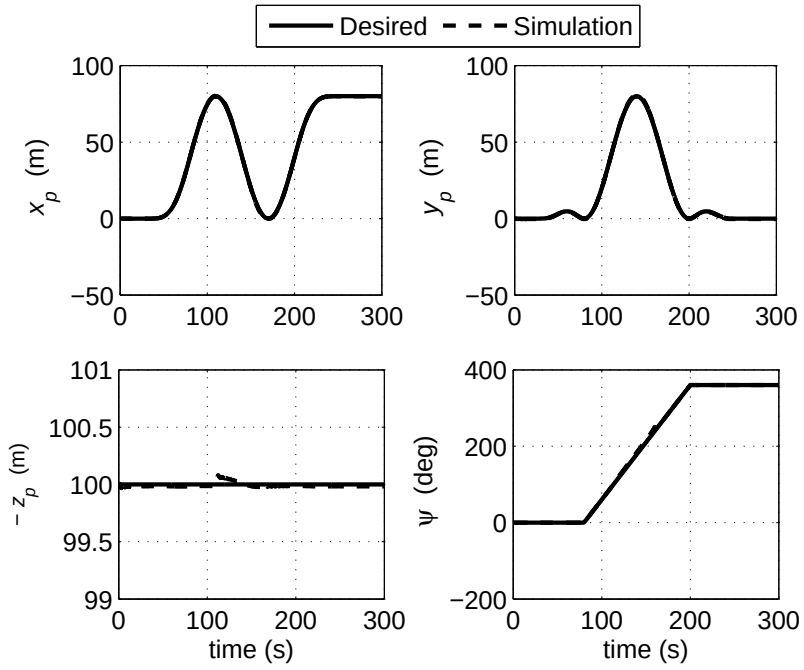

Figure 6.8: The position components of the control point and yaw angle subject to a wind disturbance of 4 m/s from 110-160 s (circular trajectory).

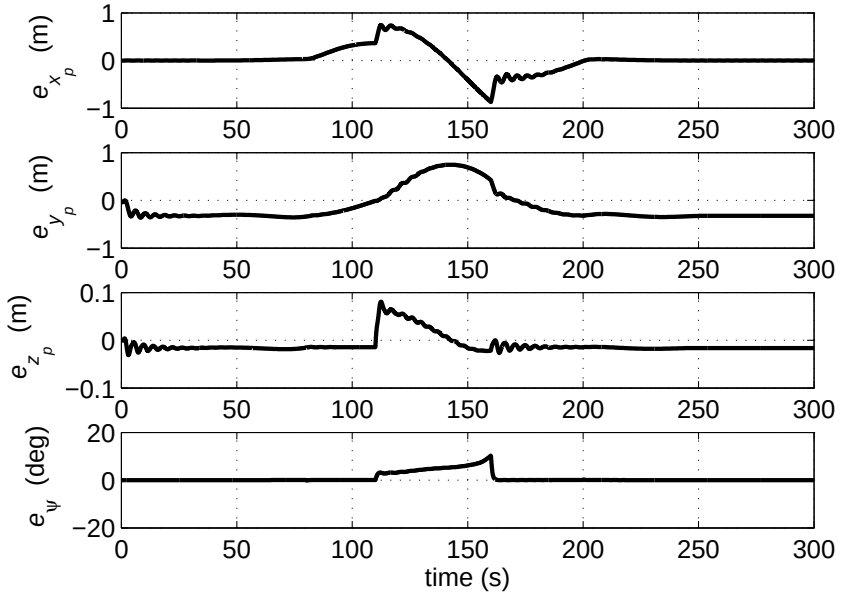

Figure 6.9: The error components of the control point position subject to a wind disturbance of 4 m/s from 110-160 s (circular trajectory).

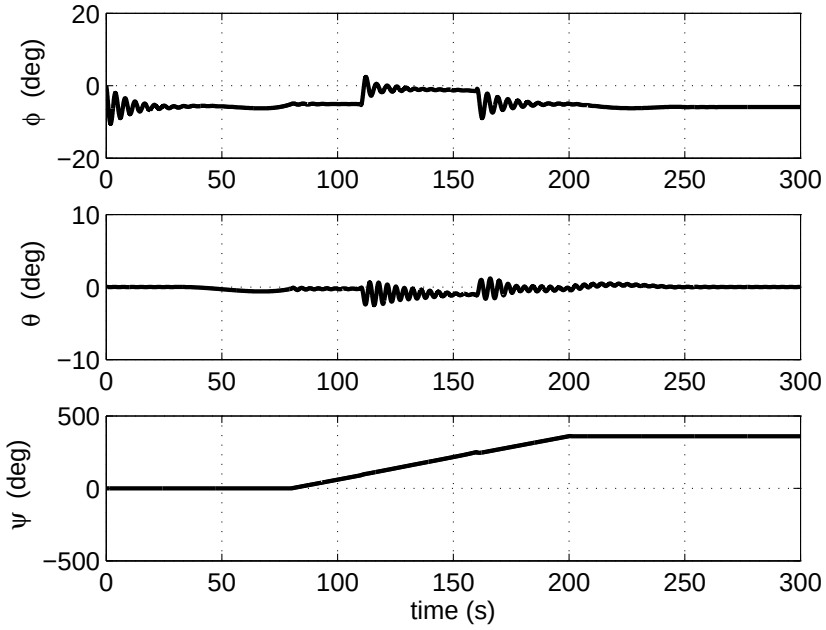

Figure 6.10: The attitude of the helicopter: roll, pitch and yaw Euler angles subject to a wind disturbance of 4 m/s from 110-160 s (circular trajectory).

constant angles in hover. Once the wind starts at 110 s at point C on the path, the roll angle starts to tilt back to about 0 deg from the hover roll angle at -6 deg to compensate the fuselage drag caused by the wind component along the negative y-axis in the body coordinates. This continues until the wind vanishes at 160 s. In addition, tilting back around the roll axis results in an increase in the thrust component along the z-axis. Therefore, the magnitude of the collective pitch is decreased by the controller as shown in Figure 6.11 to compensate for the excessive thrust and maintain the altitude of the helicopter's control point at 100 m. The controller adjusts the pedal input accordingly to maintain the helicopter's longitudinal axis tangent to the circular path and it also constantly adjusts the longitudinal and lateral cyclic inputs so as to reject the wind and maintain the helicopter on the desired circular trajectory.

The simulated and desired trajectories closely match despite the 4 m/s wind

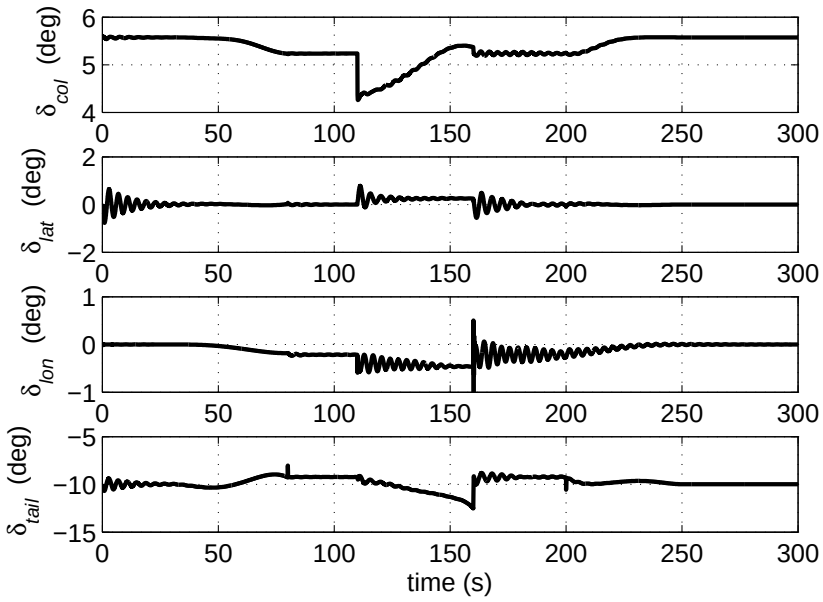

Figure 6.11: The control inputs: collective, longitudinal/latitude cyclic and pedal subject to a wind disturbance of 4 m/s from 110-160 s (circular trajectory).

disturbances, indicating that the SMC controller based on the square control-affine model of the helicopter is also effective in the trajectory tracking of a forward turn maneuver and robust to the wind disturbances.

6.3 Summary

A robust sliding mode control (SMC) based on the nonlinear square control-affine model of the helicopter dynamics obtained in Chapter 3 is designed and tested using simulations. Two simulations are performed to test the controller tracking: one, a three-dimensional complex figure-8 maneuver with ±20% parameter variations in the mass and moments of inertia; two, a forward turn maneuver in the presence of 4 m/s wind disturbances. When the controller tracking is tested on a complex three-dimensional figure-8 trajectory in simulation, good tracking with a mean absolute error of 0.18 m in the position of the control point and 0.08 deg in the yaw angle is achieved despite ±20% parameter variations. The simulation

results also show that the SMC designed based on the square control-affine model of the helicopter is effective in tracking complex trajectories in the presence of wind disturbances with a mean absolute error of 0.17 m in the position of the control point and 0.4 deg in yaw angle.

Chapter 7

Hardware-In-The-Loop Testbed Design for Control Implementation and Initial Controller Gain Tuning[1]

Unmanned aerial systems are a very active research area due to their broad range of applications [57, 58, 59, 60, 61]. Researchers are working on different types and sizes of Unmanned Aerial Vehicle (UAV) platforms, from Micro-Air-Vehicles (MAV) including Quadrotors and micro fixed-wing aircrafts, to Ultra-High-Endurance (UHE) vehicles [62, 63, 64, 65, 66, 67, 68]. During the process from conceptual design to fabrication and deployment, a number of technical and theoretical challenges must be solved. UAV control is a challenging multidisciplinary problem that combines control with dynamics and aerodynamics. Particularly challenging are Vertical Take-off and Landing (VTOL) platforms among which unmanned helicopters are one of the most demanding.

Due to their inherent instability, nonlinearity, non-minimum phase behavior, and aerodynamic complexity, unmanned helicopters offer tremendous challenges during the control design and implementation phases [69, 70, 71, 72, 73]. In-flight tuning of control parameters of small unmanned helicopters is difficult due to

[1] A version of this chapter has been published in [30].

their high manoeuvrability and inherent instability properties, and catastrophic damage in the event of a crash. Although computer simulation is extremely useful to test controller performance, an intermediate step between simulation and real flight test allows for implementation issues on the real hardware to be tested.

7.1 Introduction

From simple testbed configurations to complete and costly hardware-in-the-loop (HIL) simulation testbeds, a variety of systems have been reported in the literature. A three Degree of Freedom (3-DOF) testbed is described in [74] and [75] and consists of an arm with a platform on one end and two propellers mounted to the platform to emulate a helicopter. The platform itself has 1-DOF motion about pitch axis and the whole arm is balanced with a counterweight at the other end. Thus the arm is free to move in both elevation and azimuthal directions. In addition, the main arm is equipped with a motorized lead screw, allowing the motion of a mass attached to it. In this way, controllable and quantifiable disturbances can be generated. This setup is useful to study nonlinearities, uncertainties and unmodeled dynamics. However, due to the constraints imposed by this system, it does not represent the response of an actual helicopter. For example, the emulated helicopter cannot perform a free translational motion and its Center of Gravity (CG) is constrained to the surface of a sphere.

To test the landing phase in difficult terrains for helicopters, a 5-DOF HIL testbed is described in [76]. The system is composed of a 5-DOF test platform, a computer that controls the motion of the testbed and an avionics box. The testbed itself can perform linear absolute motion along x, y and z axes and two angular motion, pan and tilt, relative to the platform in which the helicopter's avionics is attached. The testbed in conjunction with the avionics box are used to emulate the helicopter's motion based on the dynamic model, which provides

high repeatability during emulated flight trajectory tracking in a controlled environment. This is an effective solution to the problem of landing on difficult terrains, but it is inadequate for those cases in which unmodeled dynamics or unexpected disturbance of the helicopter are present since the actual helicopter is not included.

Another approach that involves a 5-DOF testbed is presented in [77]. It is composed of a central shaft with an arm attached to it, allowing for azimuthal and elevation motion. At the end of the arm there is a platform allowing rotation in the three Euler directions. The helicopter cannot perform a free translational motion but constrained motion is allowed by the testbed. A fuzzy logic based algorithm is used to control the helicopter on the testbed. Although the testbed works well with the fuzzy logic control as a non model-based algorithm, it is difficult to use this testbed for model-based control. This is due to the constraints imposed by the testbed on the translational motion of the helicopter which modifies the real unconstrained helicopter response. For example, to increase the altitude of the helicopter on the testbed, its Center of Gravity (CG) must move towards the center of the testbed, and CG is constrained to the surface of a sphere and cannot move freely in space.

A 6-DOF indoor stand is presented in [78] for control studies. The testbed is composed of a linkage mechanism that allows for the free motion of the helicopter in a $2 \times 2 \times 2\text{m}^3$ cube. The symmetrical geometry of the mechanism makes it equivalent to a concentrated mass, and the design of the stand allows for the free 6-DOF motion of the helicopter. However, the mechanism attached to the helicopter constantly alters the 3D location of its CG during the operation, and the added dynamics of the testbed might not be negligible.

Another approach is presented in [79] to test the performance of MAVs in near-Earth environments such as forests or in an urban environment. The design

concept is a 6-DOF gantry attached to a non-flying mockup of a MAV. The mockup emulates the motion of the MAV using a high-fidelity mathematical model and a control system that moves the gantry accordingly. The test rig is equipped for emulating adverse weather conditions such as fog, rain and dust. Although, the concept provides a suitable solution for testing MAVs in the Near-Earth environments, it might not be suitable for the cases dealing with unmodeled dynamics, since the actual vehicle is not included.

In this work, to facilitate tuning of control gains as well as testing both model-based and non-model-based controllers against external disturbances for small unmanned helicopters, a low-cost HIL testbed is designed, built, and experimentally tested. By implementing a 6-DOF nonlinear mathematical model of the helicopter, the developed HIL simulation generates the actual motion of the vehicle and calculates the states. Then, an onboard computer determines the control signals to the actual helicopter mounted on the testbed. A 2-DOF testbed setup configurable for independently testing the longitudinal, lateral, and heading control is presented. In the designed testbed, the added dynamics due to the testbed itself is negligible. Using this testbed, the robustness of the controller can be tested against external disturbances by manually or mechanically disturbing the helicopter during the operation, and its performance can be tuned. This can be difficult to do in a real flight test. A damping system is designed to exert no damping force at hover, which allows for the hover control testing without any interference from the damping system. If the helicopter deviates from its nominal hover position, the damping increases and smoothly slows down the motion. This minimizes the structural stress on the fuselage and rotor mechanism for large deviations. The designed HIL testbed allows for testing the helicopter in hover and for any smooth trajectories, such as the forward flight, figure-8, etc.

7.2 HARDWARE-IN-THE-LOOP (HIL) SIMULATION

Figure 7.1: Front and side views of the HIL testbed.

Controller gain tuning is often part of a control design, and requires the system to be in operation during the tuning process. For small unmanned helicopters, in-flight gain tuning is potentially risky and expensive due to the high manoeuvrability and internal instability properties of these vehicles which may result in a crash during the tuning process. In order to facilitate safe tuning of control gains and to test the controller against external disturbances in a controlled environment, a hardware-in-the-loop (HIL) testbed design for small unmanned helicopters has been developed and is shown in Figure 7.1.

Schematics of the testbed from the front and side views are shown in Figure 7.2. This testbed is a 2-DOF system composed of a long pole to raise the helicopter off the floor to eliminate the ground effect, and a headpiece. The pole is anchored to the ground, and the headpiece is connected to the pole through a set of thrust roller bearings, which allow for the rotation of the head with respect to the pole around the vertical Z-axis. The headpiece itself is composed

of: a U-shape aluminum plate, two arms, a damping cylinder, a counter balance weight, and one stopper on each side. The helicopter is mounted on Arm 1 which is connected to Arm 2 through two ball bearings on the U-shape plate. This allows for the rotation of the helicopter around the horizontal X-axis. To allow independent testing of the longitudinal/lateral motion, a mechanical device restricts the rotation of the headpiece around the vertical axis. Two adjustable hard stoppers restrict the rotation around the X-axis to ±30deg. In the event of controller malfunction, a nonlinear passive damping system, shown from the front view in Figure 7.2, prevents the helicopter from hitting the hard stops at a large angular speed.

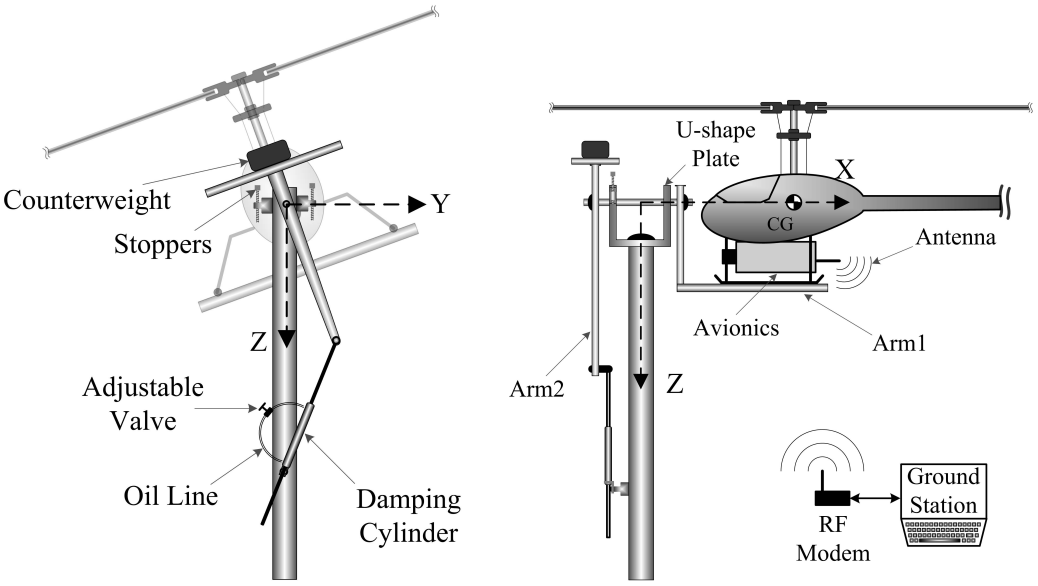

Figure 7.2: HIL Testbed schematics, front and side views.

The damping system is composed of a double acting cylinder, fully filled with a light oil NUTO A10. An oil line with an adjustable needle valve connects the cylinder's inlet to its outlet and makes a closed path of oil. Since the cylinder is double acting and its rod extends from both ends of the barrel, it allows for the continuous flow of oil between the chambers and does not require an oil reservoir.

When testing the helicopter around hover on the testbed, the cylinder is vertical and creates a negligible damping due to the vertical mechanism geometry. As the helicopter deviates from hover, the cylinder angle relative to the vertical pole increases and the damping increases in a nonlinear manner. Once the control gains are properly tuned for hover, the damping cylinder is removed and the controller is tested against external disturbances.

The counter weight is chosen to precisely balance the arms to mimic hover condition, and the mechanism shown in Figure 7.2 is designed such that the CG of the helicopter is aligned with the horizontal X-axis which is the axis of rotation in roll and pitch tests.

The goal of the designed HIL simulation testbed is to safely test and tune the longitudinal, lateral and heading controller of the helicopter in real-time on the ground. In addition, it allows for testing the robustness of the controller against external disturbances. Using this testbed, the helicopter can be disturbed during operation and the performance of the controller can be tuned. Furthermore, the testbed is designed such that the added dynamics due to the testbed itself are negligible. The testbed can also be used for testing the avionics of small helicopters on the ground. The disadvantage of this HIL system is that all degrees of freedom cannot be tested simultaneously and they must be tested one at a time. Simultaneous testing of all DOFs of the helicopter requires a more complex setup, in which typically the added dynamics due to the testbed itself are not negligible.

The block diagram of the HIL simulation is shown in Figure 7.3. The controller block represents the onboard embedded control system which calculates and outputs control signals to the actual servos of the helicopter. The helicopter block in the diagram represents the physical helicopter to be tested. The IMU

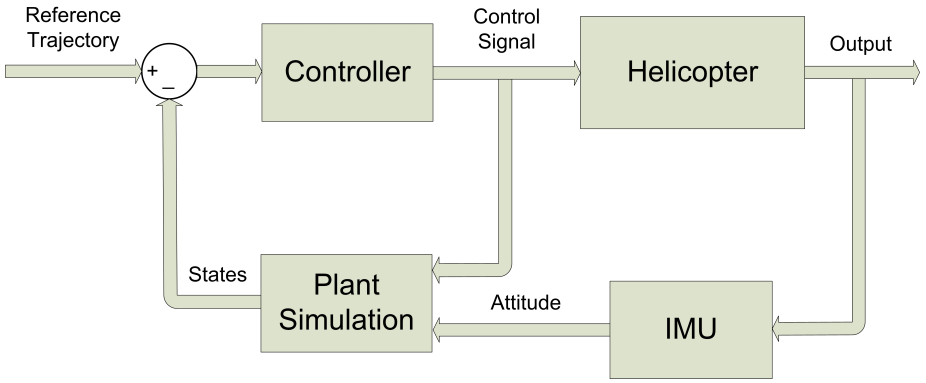

Figure 7.3: Block diagram of the HIL simulation.

block represents the Inertial Measurement Unit, which determines the actual attitude of the helicopter including the Euler angles and their rates at each sampling time. However, as the helicopter is fixed on the testbed, its position and velocity are determined using the plant simulation model. The plant simulation generates the actual motion of the helicopter using its 6-DOF nonlinear mathematical model. Using the control signals calculated by the controller, and the current IMU outputs as inputs, the position and velocity of the simulated helicopter are determined at each sampling time by integrating the 6-DOF equations of motion. The calculated states of the helicopter are then used as the feedback signal to the controller for the next sampling time computations. This HIL is implemented in real-time at a sample rate of 50 Hz using the xPC Target which is a real-time software environment from Mathworks.

This HIL testbed allows for testing the helicopter not only in hover but also for smooth trajectories, such as the cruise flight, figure-8, etc. For instance, lateral control of the helicopter in a figure-8 trajectory can be implemented on the testbed by allowing the physical rotation of the vehicle only around the roll axis (the x-axis shown in Figure 7.2) and then calculating the actual motion of the rest of the DOFs in the plant simulation using its 6-DOF nonlinear mathematical model. Since, the physical motion of these DOFs are mechanically restricted on

the testbed, and the controller is controlling all 6-DOFs of the helicopter, the generated control signal for them are not physically realized on the actual helicopter. Rather, some of these signals are applied to the simulated helicopter model in the plant simulation, while the control signal corresponding to the moving DOF is physically applied to the actual helicopter.

7.3 Testbed Modeling

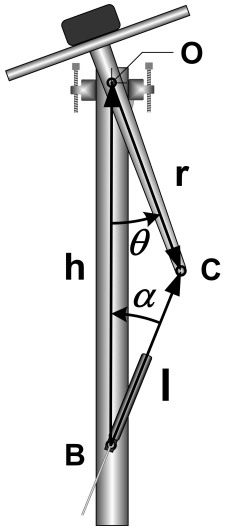

Figure 7.4: Testbed mechanism.

Using the Newton-Euler equations of motion (Eq. (3.2)), the attitude dynamic model of the helicopter and the testbed can be written as:

$$\frac{d\boldsymbol{\omega}}{dt} = (\boldsymbol{I} + \boldsymbol{I_{tb}})^{-1}(\mathbf{M} + \mathbf{M_{tb}}) - (\boldsymbol{I} + \boldsymbol{I_{tb}})^{-1}(\boldsymbol{\omega} \times (\boldsymbol{I} + \boldsymbol{I_{tb}})\boldsymbol{\omega}) \tag{7.1}$$

where, the angular velocity of the helicopter in the body coordinates is denoted by $\boldsymbol{\omega} = [p\ q\ r]^T$, and $\boldsymbol{I}$ and $\boldsymbol{I_{tb}}$ are the moment of inertia tensors of the helicopter and the testbed, respectively. The moment of inertia due to the components on the testbed that are moving with the helicopter is almost ten times smaller that

of the helicopter in pitch and five times smaller in roll, thus are neglected. **M** is the total moment vector applied to the helicopter from the main and tail rotor blades. The parasitic moment vector applied from the testbed to the helicopter is denoted by $\mathbf{M_{tb}}$. This is due to the damping effect of the cylinder, and its magnitude can be written as:

$$M_{tb} = -rb\dot{\ell}\cos(\frac{\pi}{2} - \theta - \alpha) = -rb\dot{\ell}\sin(\theta + \alpha) \tag{7.2}$$

where, b is the damping coefficient of the cylinder. $\dot{\ell}$ is the rate at which the cylinder elongates and is calculated by taking time derivative of the loop closure equation in the complex plane for the planar mechanism "OBC". The following vector relation holds for the mechanism shown in Figure 7.4:

$$\mathbf{l} - \mathbf{r} = \mathbf{h} \tag{7.3}$$

The loop closure equation can be written in the complex plane as:

$$\ell\ e^{j(\frac{\pi}{2}-\alpha)} - r\ e^{-j(\frac{\pi}{2}-\theta)} = jh \tag{7.4}$$

where $j = \sqrt{-1}$. Using Euler's formula results in:

$$\ell(\sin(\alpha) + j\cos(\alpha)) - r(\sin(\theta) - j\cos(\theta)) = jh \tag{7.5}$$

Rearranging Eq. (7.5) results in:

$$\ell\sin(\alpha) - r\sin(\theta) = 0 \tag{7.6}$$

$$\ell\cos(\alpha) + r\cos(\theta) = h \tag{7.7}$$

Since the testbed is designed to test the helicopter around hover, where the angles θ and α are small. Assuming small angles for θ and α in Eqs. (7.6) and (7.7) results in:

$$\ell\alpha - r\theta = 0 \tag{7.8}$$

$$\ell + r = h \tag{7.9}$$

Then, differentiating from Eqs. (7.6) and (7.7) with respect to time and assuming small angles results in:

$$\dot{\ell}\alpha + \ell\dot{\alpha} - r\dot{\theta} = 0 \tag{7.10}$$

$$\dot{\ell} - \ell\alpha\dot{\alpha} - r\theta\dot{\theta} = 0 \tag{7.11}$$

Rearranging Eqs. (7.8) to (7.11) results in:

$$\alpha = \frac{r\theta}{h - r} \tag{7.12}$$

$$\dot{\ell} = r\dot{\theta}\frac{(\alpha + \theta)}{1 + \alpha^2} \tag{7.13}$$

Since, α is small around hover, Eq. (7.13) can be simplified to:

$$\dot{\ell} = r\dot{\theta}(\alpha + \theta) \tag{7.14}$$

Substituting Eqs. (7.12) and (7.14) into (7.2) results in a parasitic testbed moment of:

$$M_{tb} = -\frac{h^2 r^2}{(h - r)^2} b\theta^2\dot{\theta} \tag{7.15}$$

Equation (7.15) shows that the damping moment, M_{tb}, generated by the cylinder

around hover is negligible when θ is small. However, if the helicopter on the testbed becomes unstable, it starts deviating from hover and the damping moment given in Eq. (7.15) increases in a nonlinear manner. This is used to prevent the helicopter from abrupt motion or hitting the hard end stops.

7.3.1 Tuning the Control Gains

In order to tune the control gains in hover for longitudinal, lateral and heading motion using the testbed, the following steps are taken:

1. One of the longitudinal or lateral motion is chosen and the helicopter is placed on the testbed accordingly. For example, the testbed setup for the longitudinal control is sown in Figure 7.5

2. It is assumed that the positions of the CP corresponding to the other motion and the heading of the helicopter are all equal to the desired ones. This is to facilitate the process of finding the appropriate control gains corresponding to a motion. For example, to obtain the gains of the longitudinal motion, the lateral and vertical positions of the control point and the heading angle of the helicopter are assumed to have the corresponding values in hover.

3. At hover, tune the controller gains to stabilize the helicopter to get initial gains. Some trial and errors might be required to find the appropriate gains.

4. With the control gains set at initial values for hover, remove the damping cylinder and repeat the test to fine tune the controller. Then the helicopter is intentionally disturbed from the hover position and the gains are further tuned such that the appropriate response rejection of the helicopter to external disturbances is achieved. The applied disturbance that can be rejected depends on the size of the helicopter and the range of the aerodynamic moments that the blades can generate.

5. Once the control gains for the longitudinal motion are properly tuned, they are updated in the control program, and the controller is tuned for the lateral motion. To do this, the helicopter is placed as shown in Figure 7.6, and the steps 1 to 4 above are repeated to obtain the gains for the lateral motion.

6. Once the control gains of the longitudinal and lateral motion are tuned, the helicopter is placed on the testbed as shown in Figure 7.7, and the procedure is again repeated to tune the controller for the heading motion.

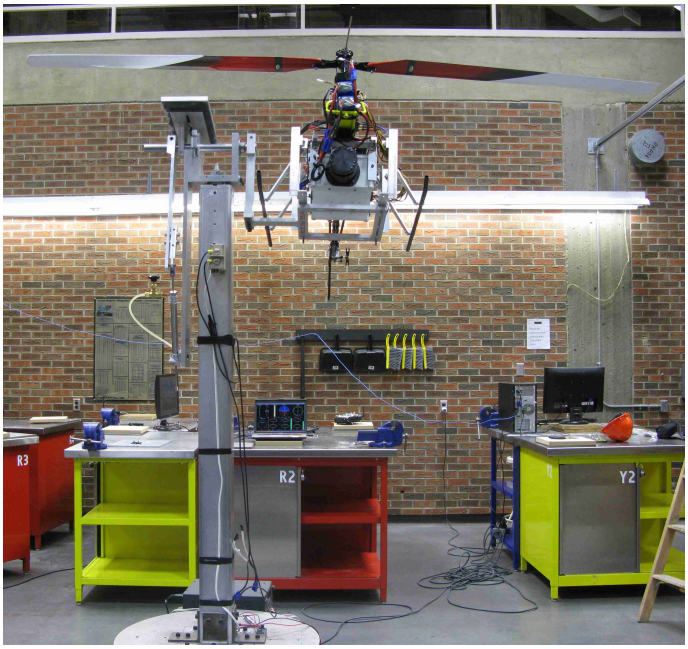

Figure 7.5: HIL testbed setup for the longitudinal control in hover.

7.4 Summary

A HIL testbed for testing small unmanned helicopters on the ground has been described. The testbed provides a safe and low-cost platform to test a control

Figure 7.6: HIL testbed setup for the roll control in hover.

Figure 7.7: HIL testbed setup for the yaw control.

algorithm in real-time and to tune the control gains. It also allows testing in a controlled environment of the robustness of the controller to external disturbances. To use the testbed, 6-DOF mathematical model of the helicopter is needed to determine the actual motion of the helicopter in the HIL system which is described. The experimental results of the control implementation using the HIL testbed will be presented in Chapter 8.

Chapter 8

Experimental Results[1]

In this chapter, the test results of the SMC implementation on the Evolution-Ex helicopter using the HIL testbed (described in Chapter 7) and real flight experiments are presented.

The SMC designed based on the square affine-in-control helicopter dynamics (described in Chapter 3) is used. First, the HIL testbed is used for the initial controller gain tuning and testing the robustness of the controller against external disturbances in a controlled environment. Next, the real flight control results for the heading-hold and hover maneuvers are presented.

8.1 HIL Test Results

A 2-DOF HIL testbed configurable for independently testing the longitudinal, lateral, and heading control (described in Chapter 7) is used to tune the SMC control gains in this section.

Following the tuning process described in section 7.3.1, the control gains for the longitudinal, lateral and heading motion are obtained and listed in Table 8.1. The HIL test results are presented in the following sections.

[1] A version of this chapter has been published in [34].

Table 8.1: Control gains obtained from the HIL experiments.

Gain	Description	Longitudinal	Lateral	Heading
λ	*Convergence rate*	2.5	2.5	2.5
F	*Bound on f*	10	15	1
Δ	*Bound on b*	0.5	0.5	0.5
η	*Surface reach time*	1	1	1
Φ	*Boundary layer THK*	0.8	0.6	1

8.1.1 HIL Longitudinal Control Experiment

The longitudinal control of the helicopter is tested by placing it on the testbed as shown in Figure 7.5. Only the longitudinal motion of the helicopter is tested in this experiment, so the physical rotation around the vertical axis of the testbed is mechanically restricted. Although the helicopter is physically restricted to rotate only around the pitch axis in this experiment, the controller is controlling all 6-DOFs of the helicopter. The actual motion of the helicopter is calculated using the 6-DOF nonlinear model of the helicopter at every sampling time.

The CG of the helicopter shown in Figure 7.5 is aligned with the axis of rotation. Depending on the size of the blades and the maximum rolling and pitching moments generated, the needle valve on the damping cylinder shown in Figure 7.2 is adjusted to prevent sudden movements that could damage the vehicle during tuning. Then once the desired gains are set, the damping effects are reduced by adjusting the needle valve and then by removing the cylinder to test the controller subject to the imposed external disturbances without damping.

The Control Point (CP) is chosen to be 3 m above the CG on the main hub axis of the Evolution-EX helicopter. In the following, the controller is tested for hover, forward flight, and figure-8 trajectory tracking and the corresponding results are presented.

8.1.1.1 Hover-Longitudinal-HIL Test

To emulate hover, a constant collective pitch of $\delta_{col} = 5.6$ deg for Evolution-EX at hover, is used throughout this experiment. This is due to the fact that the vertical motion of the helicopter is mechanically restricted on the testbed, and the generated control signal for the heave motion is not physically applied to the actual helicopter, but is applied to the simulated helicopter model in the plant simulation as shown in the block diagram of Figure 7.3. In this experiment, the control signal corresponding to the pitch motion is physically applied to the actual helicopter.

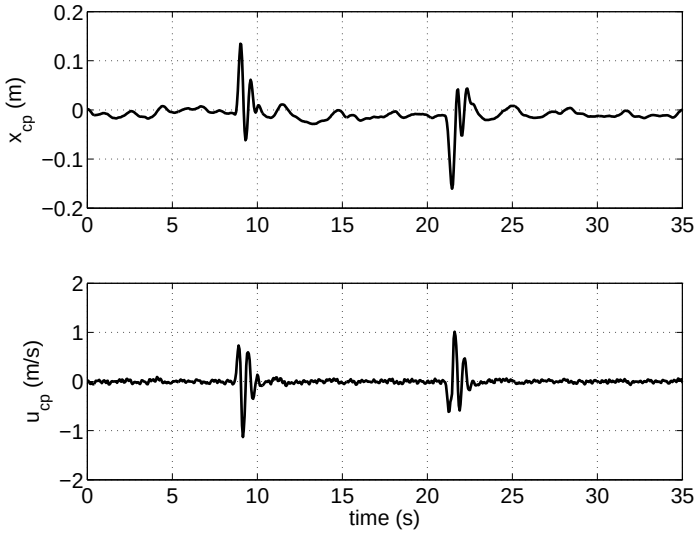

Figure 8.1: Position and velocity of the control point in the longitudinal control - the two overshoots at 8.5 and 21 s are due to the intentional external disturbances.

The closed-loop response of the control point position and velocity along the longitudinal axis is shown in Figure 8.1, and the pitch angle, pitch rate, and the longitudinal cyclic command are shown in Figure 8.2. During the experiment the helicopter was intentionally disturbed two separate times at 8.5 and 21 s, by manually exerting a moment of approximately 2.5 Nm to the fuselage for about 1 s to tilt it away from the level position. As shown in Figures 8.1 and 8.2, the

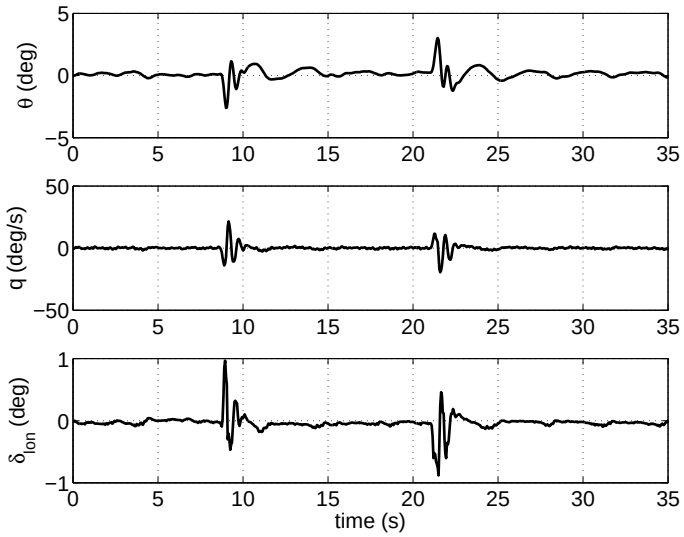

Figure 8.2: Closed-loop pitch response and longitudinal cyclic input in the presence of intentional external disturbances.

controller responds by actuating the longitudinal cyclic pitch of the main rotor blades to reject the disturbances and maintain the zero position and velocity of the control point along the longitudinal axis with a mean absolute error of 1.5 cm and 5.1 cm/s, respectively. Also, the steady state pitch angle and pitch rate are close to zero, which show that the controller stabilizes the longitudinal motion of the helicopter in the presence of the external disturbances.

8.1.1.2 Forward Flight-Longitudinal-HIL Test

The desired forward trajectory shown in Figure 8.3 is composed of two successive acceleration/deceleration cycles. The trajectory initially starts from the zero position of the CP at hover, and after 10 s accelerates to reach the speed of 5 m/s through a 4^{th}-order polynomial. It continues the cruise flight at this speed for 15 s, then decelerates again through another 4^{th}-order polynomial until it comes to a stop at 150 m from the starting point. This cycle is repeated in the backward flight until it reaches the starting point.

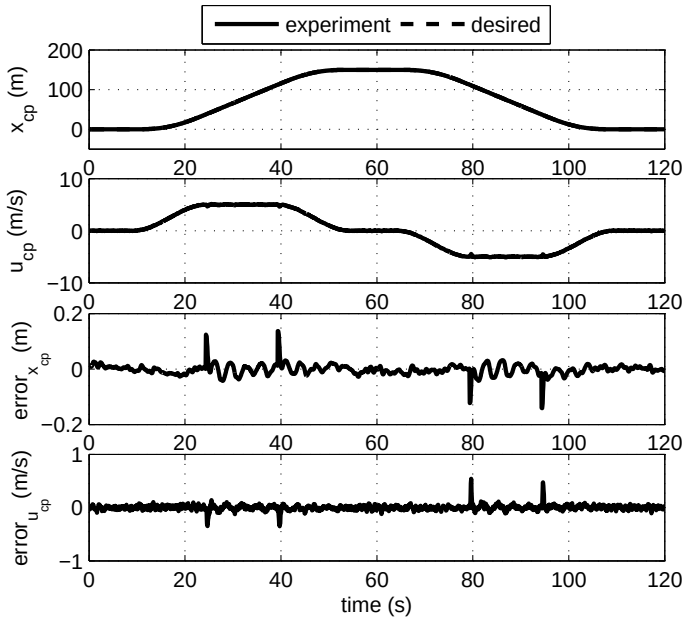

Figure 8.3: Position and velocity of the control point and error in the forward flight trajectory tracking control.

The trajectory tracking results are shown in Figure 8.3. In addition, the error in both position and velocity are also plotted in Figure 8.3 - Note the y-axis scale of the position and velocity errors in this figure. The results show that the controller successfully tracks the desired trajectory with a mean absolute error of 1.8 cm in position, and 3.9 cm/s in velocity. The spikes in the position and velocity errors at the times 25, 40, 80 and 95 s, shown in Figure 8.3, are due to the discontinuity in the transitions between the curve segments contained in the desired trajectory. In fact, the desired trajectory function of the control point position, x_{cp}, is of differentiability class C^2, so its second derivative (acceleration) is not differentiable at the transition points. This acts as disturbances on the helicopter, and the controller reacts accordingly at the times 25, 40, 80 and 95 s to reject them as shown in Figure 8.4. The pitch angle and pitch rate results are shown in Figure 8.4 and are close to zero which indicate that the controller stabilizes the longitudinal motion of the helicopter in the forward flight.

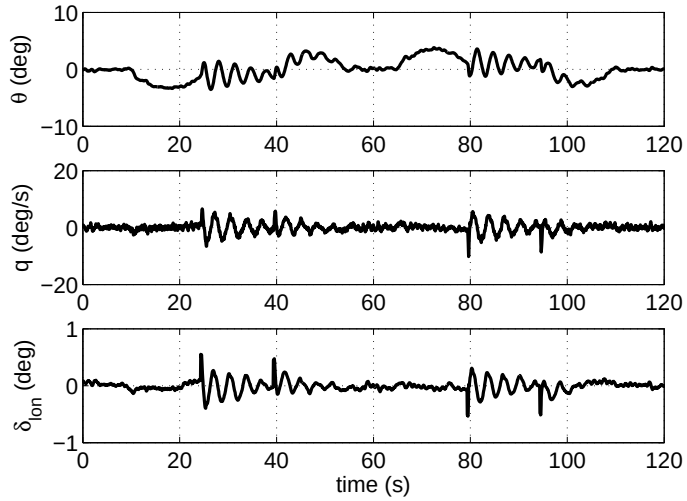

Figure 8.4: Closed-loop pitch response and longitudinal cyclic input in the forward flight trajectory tracking control.

8.1.1.3 Figure-8 Trajectory-Longitudinal-HIL Test

The trajectory shown in Figure 8.5 is composed of a 5th-order polynomial section followed by a figure-8 section. The trajectory starts in hover at $x_{cp} = 10$ m and stays in hover for 10 s. Then, the CP moves on a 6^{th}-order polynomial section, and after 20 s it enters a figure-8 section defined by a smooth function. Finally, after ending the figure-8 section at t=130 s, it transitions to a 7^{th}-order polynomial and comes to a stop at t=160 s and $x_{cp} = 8$ m. The yaw angle is considered constant at zero in this trajectory.

Similar to the forward flight trajectory tracking, controlling the helicopter on the figure-8 trajectory also requires controlling the other DOFs, and since the helicopter is physically allowed to rotate only around the pitch axis in this experiment, only the longitudinal cyclic pitch command is physically applied to the actual helicopter.

A comparison between the desired and experiment results in Figure 8.6 shows

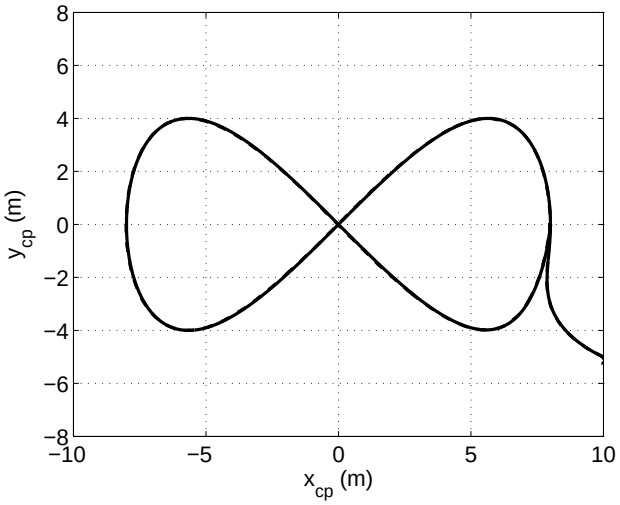

Figure 8.5: Figure-8 desired trajectory.

that the controller successfully tracks the desired trajectory with a mean absolute error of 1.7 cm in position, and 2.1 cm/s in velocity. Also, the pitch angle and pitch rate results in Figure 8.7 show that the controller stabilizes the longitudinal motion of the helicopter in figure-8 trajectory tracking. Since higher order polynomials are used to define the desired trajectory in this test, no spikes appeared in the position and velocity errors in Figure 8.6.

8.1.2 HIL Lateral Control Experiment

The lateral control of the helicopter is tested by securing it on the testbed as shown in Figure 7.6. In this position, the CG of the helicopter is aligned with the axis of rotation as in the side view of Figure 7.6. Similar to the previous test, once the main rotor reached the nominal speed of about 1100 rpm and the collective pitch of 5.6 deg at hover, the controller is switched on for lateral control of the helicopter.

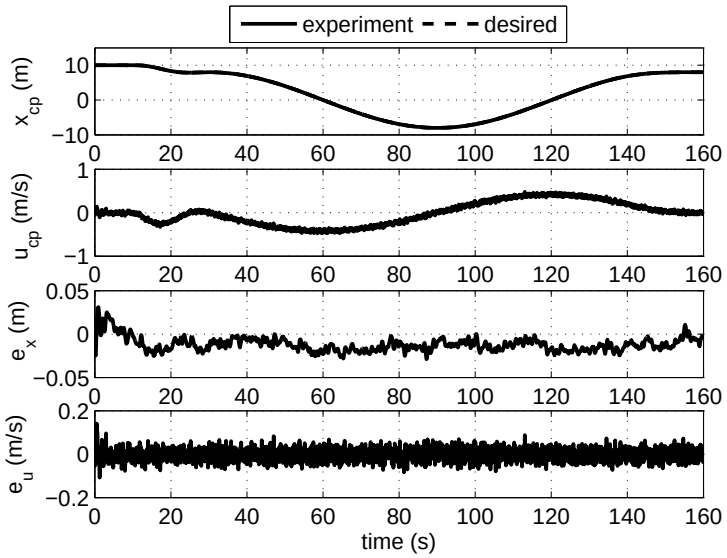

Figure 8.6: Position and velocity of the control point and error in the figure-8 trajectory tracking control.

8.1.2.1 Hover-Lateral-HIL Test

The closed-loop response of the control point position and velocity along the lateral axis is shown in Figure 8.8, while the roll angle, roll rate, and the lateral cyclic command are shown in Figure 8.9. During the experiment the helicopter is intentionally disturbed three times at 7, 13 and 19 s, by applying a moment of approximately 2.5 Nm to the fuselage for approximately 1 s to cause it to tilt away from its desired position in hover. This test demonstrates that the controller adjusts the lateral cyclic pitch of the main rotor blades to reject the disturbances and maintain the zero position and velocity of the control point along the lateral axis with a mean absolute error of 1.9 cm and 9.4 cm/s, respectively. The results in Figure 8.9 show that the desired steady state roll angle is not zero but is -6 deg. This is due to the fact that in hover, the helicopter must have a slight bank angle to compensate for the tail rotor thrust, and the desired steady state roll rate is zero. This shows that the controller stabilizes the lateral motion of the helicopter

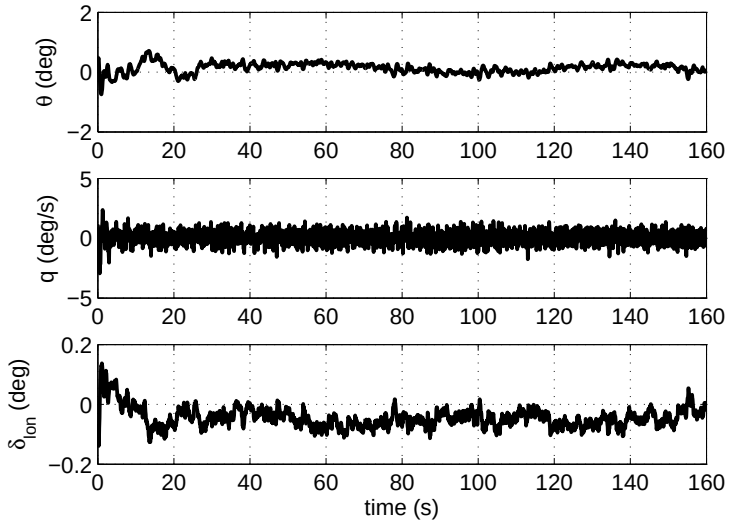

Figure 8.7: Closed-loop pitch response and longitudinal cyclic input in the figure-8 trajectory tracking control.

in the presence of intentional external disturbances.

8.1.2.2 Sideways Flight-Lateral-HIL Test

Similar to the forward test in section 8.1.1.2, the desired sideways trajectory shown in Figure 8.10, is composed of two successive acceleration/deceleration cycles. The trajectory tracking results in Figures 8.10 and 8.11 show that the controller tracks the desired trajectory with a mean absolute error of 2.3 cm in position, and 5.9 cm/s in velocity, when stabilizing the lateral motion of the helicopter in sideways trajectory tracking. Similar to the forward test in section 8.1.1.2, the spikes in the position and velocity errors at the times 35, 50, 90 and 105 s, shown in Figure 8.10, are due to the discontinuity in the transitions between the curve segments contained in the desired trajectory.

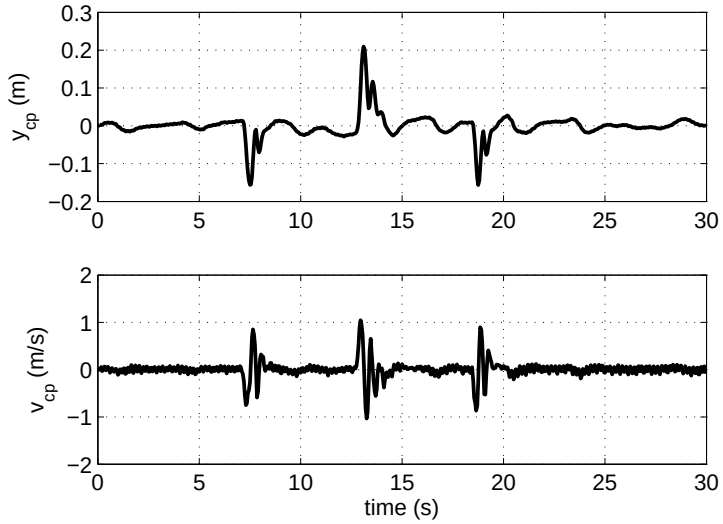

Figure 8.8: Position and velocity of the control point in the lateral control - the three overshoots at 7, 13 and 19 s are due to the external disturbances.

8.1.2.3 Figure-8 Trajectory-Lateral-HIL Test

The figure-8 trajectory is shown in Figure 8.5. As previously described, this trajectory is composed of a 5th-order polynomial and a figure-8 section. It starts at $y = -5$ m in hover and stays in hover for 10 s. Then, the CP moves on a 5th-order polynomial section for 20 s before entering a figure-8 section. Finally, it comes to a stop at $t = 160$ s and $y_{cp} = 0$ m after completing the figure-8 section.

The lateral motion results of Figures 8.12 and 8.13 show that the controller successfully tracks the desired trajectory with a mean absolute error of 0.7 cm in position and 8.8 cm/s in velocity, and stabilizes the lateral motion of the helicopter in the figure-8 trajectory tracking.

8.1.3 HIL Heading Control Experiment

To test the heading control, the helicopter is mounted on the HIL testbed shown in Figure 7.7, with the arm set removed and a flat aluminum plate attached on

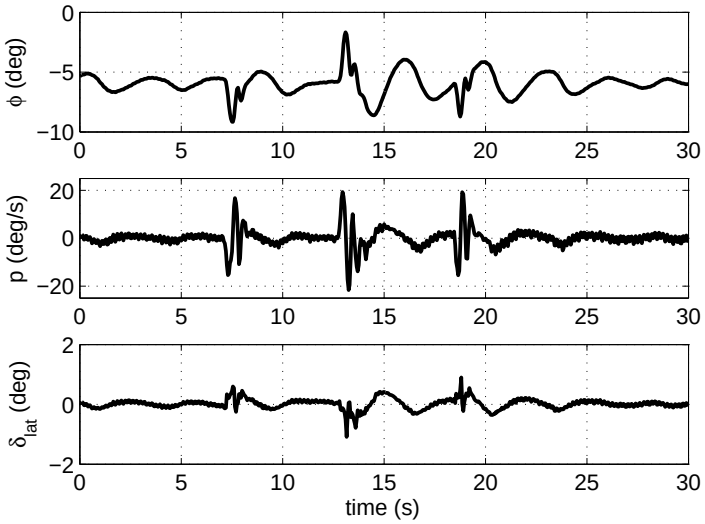

Figure 8.9: Closed-loop roll response and lateral cyclic input in the presence of external disturbances.

top of the U-shape plate. The helicopter is then mounted on the flat plate such that its CG is aligned with the vertical axis of the pole as shown in the schematic in Figure 8.14. Similar to the previous tests, a constant collective pitch at hover of $\delta_{col} = 5.6$ deg is maintained after the main blades reached the nominal spinning speed of 1100 rpm. Then, the controller is activated to control the yaw motion of the helicopter to the desired trajectory.

Both a step and a figure-8 yaw trajectories are tested with the results shown in Figures 8.15 and 8.16, respectively. Figure 8.15 shows the yaw angle, yaw rate, and tail command in the yaw control of a fast step trajectory. The results demonstrate that the controller maintains the desired yaw angle, ψ, and yaw rate, r, with a mean absolute error of 4.8 deg and 7.7 deg/s, respectively.

In Figure 8.16, during the figure-8 trajectory experiment the helicopter is subject to a large disturbance for the period of 60-80 s. This is done by manually deviating the fuselage away from the desired trajectory. The results in

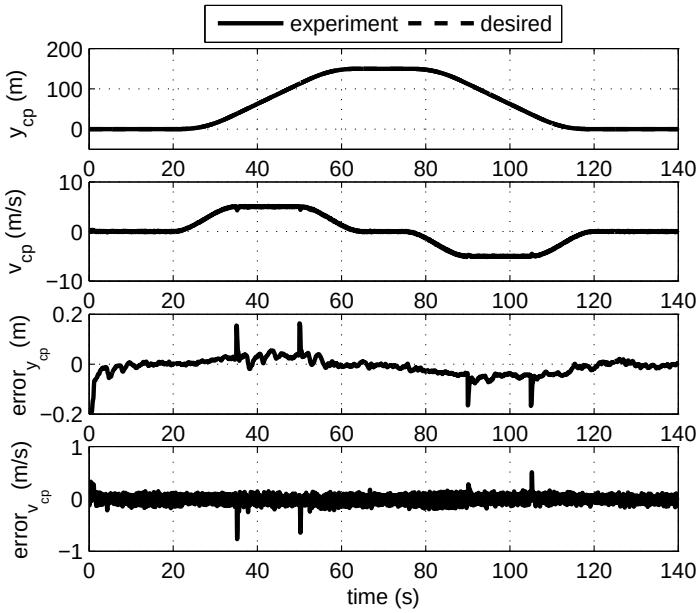

Figure 8.10: Position and velocity of the control point and error in the sideways flight trajectory tracking control.

Figure 8.16 show that the controller actuates the pitch of the tail rotor blades to reject the disturbance and maintain the desired yaw angle and yaw rate with a mean absolute error of 2.3 deg and 1.6 deg/s, respectively.

8.2 Flight Test Results

Now that the control gains are initially tuned by the HIL testbed, the SMC is tested in real flight on the Evolution-EX helicopter in this section. The flight tests include heading-hold and hover maneuvers and the flight test results are presented in the following sections.

8.2.1 Heading-Hold Control

It is very challenging to control the yaw motion of small-scale helicopters as it has a faster response than other modes including the roll and pitch dynamics. Therefore, model helicopters are normally equipped with a control augmentation system including a gyro sensor and a control unit to facilitate their yaw control

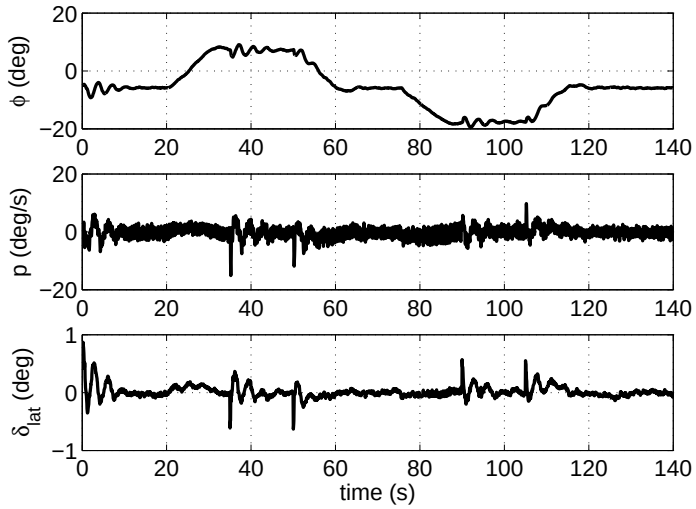

Figure 8.11: Closed-loop roll response and longitudinal cyclic input in the sideways flight trajectory tracking control.

by a pilot.

In the heading-hold maneuver, the yaw motion of the helicopter is controlled by the SMC, while the longitudinal, lateral and heave motion is stabilized by a pilot. To do this, the helicopter's gyro system is disengaged and the yaw motion is controlled using the SMC. First, the helicopter is brought to hover by a pilot and then switched to automatic control. Once switched to automatic control, the gyro system is disengaged and the heading control is taken over by the SMC to stabilize the yaw motion and hold the yaw angle of the helicopter fixed at its value at the time of switching. The heading-hold results are shown in Figure 8.17

The yaw control results in Figure 8.17 show that the SMC is effective in stabilizing the yaw motion and maintaining the heading of the helicopter at the zero reference angle with a mean absolute error of 9.8 deg in the yaw angle and 5.8 deg/s in the yaw rate in the presence of wind disturbances. Small deviations in the yaw angle of the helicopter observed during 15-20 s is due to a side wind disturbance which increases the angle of attack of the tail rotor blades and

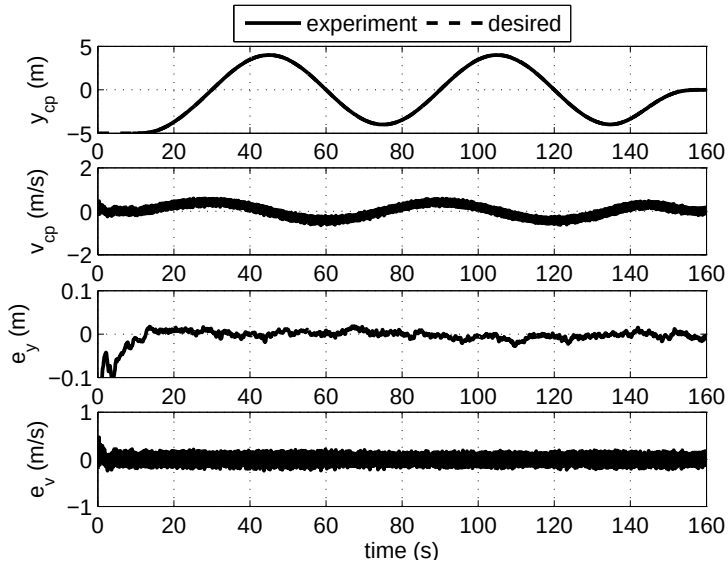

Figure 8.12: Position and velocity of the control point in the figure-8 trajectory tracking control.

causes the tail rotor thrust to increase and temporarily deviate the heading of the helicopter from zero. As shown in Figure 8.17, the controller rejects the wind disturbance by decreasing the pedal input and causes the yaw angle and yaw rate to settle back to zero.

8.2.2 Hover Control

The hover control of the helicopter in real flight using the SMC is presented in this section. In this test, the longitudinal, lateral and heave motion of the helicopter are controlled by the SMC and only the heading is controlled by the pilot. Similar to the heading-hold control, first, the helicopter is brought to hover by a pilot and then switched to automatic control. Once the pilot switches to automatic control, the SMC starts stabilizing the helicopter in hover. The control results are shown in Figures 8.18 to 8.21.

As shown in Figure 8.18, the controller maintains the control point position of the helicopter at the reference position at $(x_{cp}, y_{cp}, z_{cp}) = (20, 16, -15)$ m. The velocity components of the control point are shown in Figure 8.19, which shows

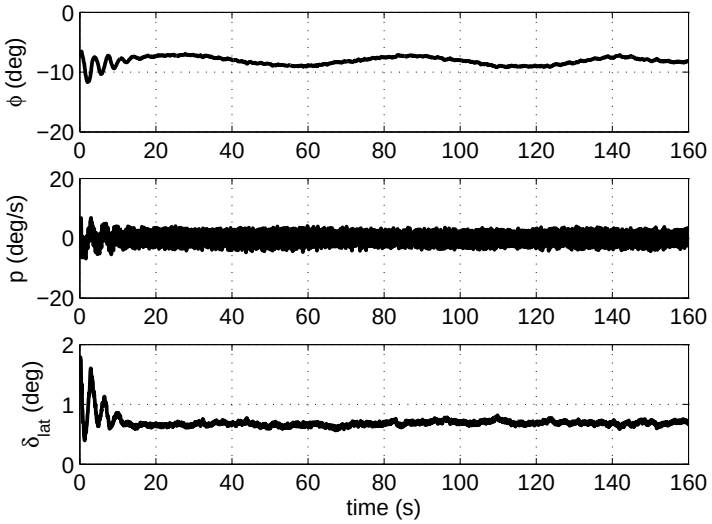

Figure 8.13: Closed-loop roll response and longitudinal cyclic input in the figure-8 trajectory tracking control.

that the controller maintains the control point velocities around zero.

The attitude response of the helicopter is shown in Figure 8.20, which shows that the roll dynamics is stabilized. The pitch response shows some oscillations which can be improved by further tuning of the pitch control gains in future works. Also, the control inputs are shown in Figure 8.21. Since, the heave motion could not be tuned using the HIL testbed, a saturation block is used for the collective input in the controller to avoid abrupt heave motion, which results in the flat peaks on the collective command graph. The saturation block could be removed in the future works after the heave gains are sufficiently tuned to result in a better heave stabilization.

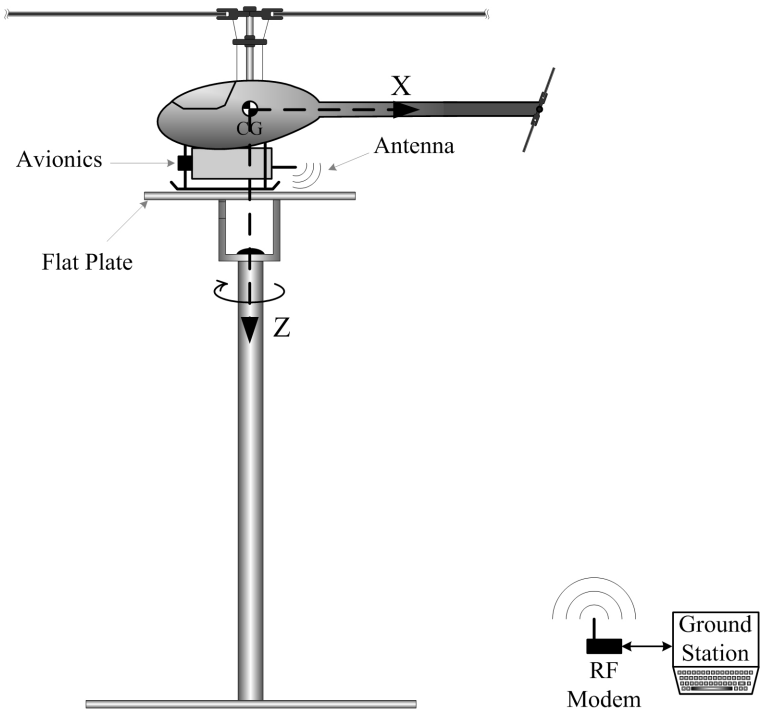

Figure 8.14: HIL Testbed schematic for the heading experiment.

8.3 Summary

The experimental results of the sliding mode control implementation on the Evolution-Ex helicopter using the HIL testbed and real flight tests have been presented in this Chapter. The HIL testbed experiments included hover, forward, sideways and figure-8 trajectories for the longitudinal and lateral control, and step and figure-8 trajectories for the heading control. The experimental results using the HIL testbed showed that the controller achieved a ± 2.5 cm accuracy on the longitudinal and lateral position trajectory tracking, and a ± 5 deg accuracy on the heading trajectory tracking in the presence of external disturbances. The real flight tests for the heading-hold and hover maneuvers have also been presented. The heading-hold control results from the real flight tests showed that the SMC achieved a ± 9.8 deg accuracy on the yaw control of the helicopter in the presence of wind disturbances. The results from the HIL testbed and real-flight

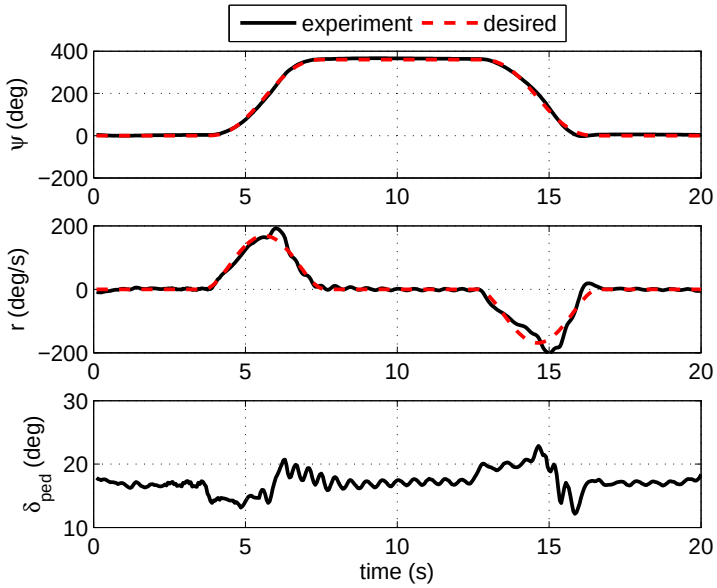

Figure 8.15: Closed-loop yaw response to the step trajectory.

tests showed that the SMC designed based on the square control-affine model of the helicopter dynamics is implementable on the helicopter and capable of stabilizing the vehicle in the presence of external disturbances.

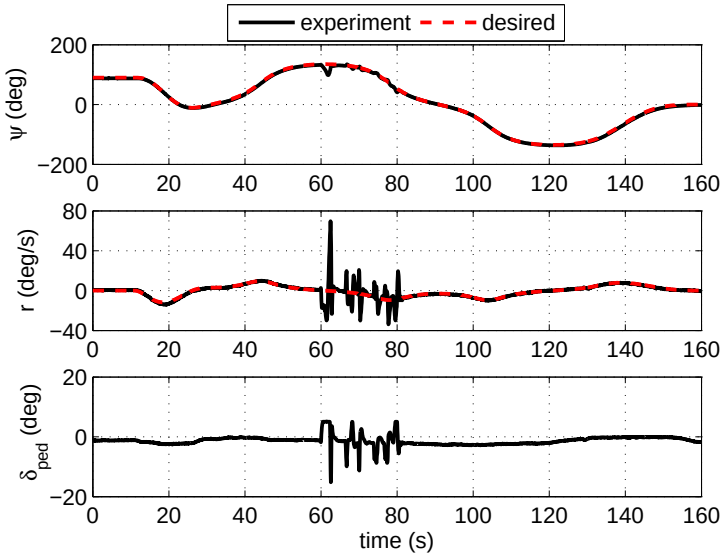

Figure 8.16: Closed-loop yaw response to the figure-8 trajectory - the overshoot at about 60 s is due to the external disturbance applied to the helicopter fuselage at 60 s.

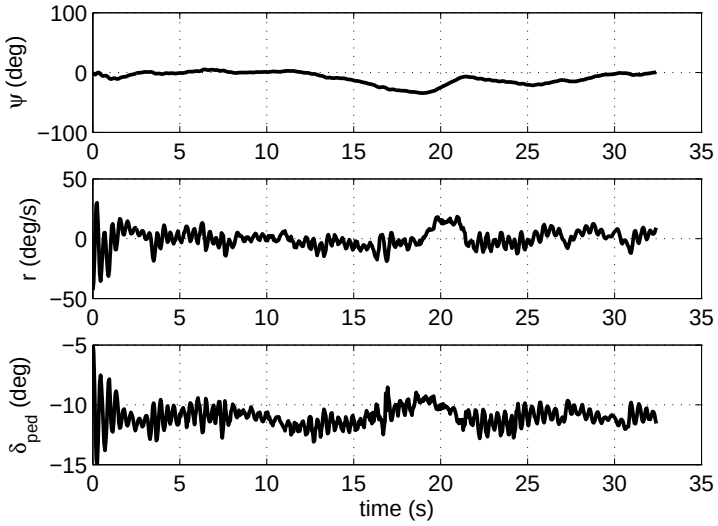

Figure 8.17: Heading-hold control in real flight. The reference yaw angle is zero.

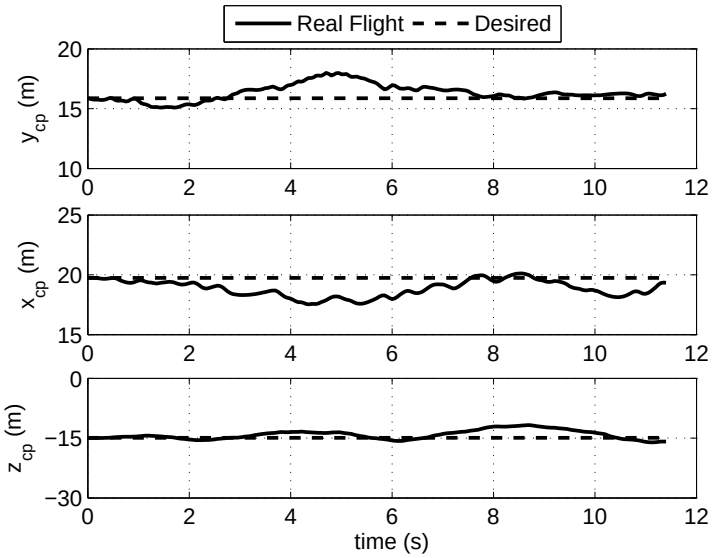

Figure 8.18: Position trajectory of the control point.

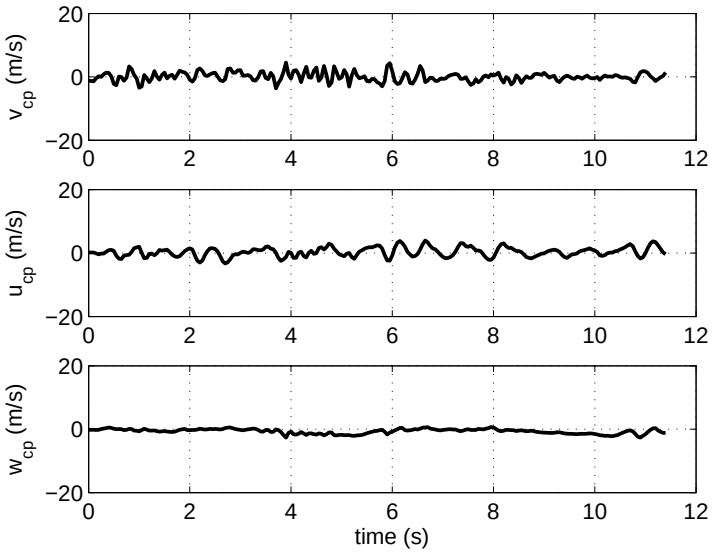

Figure 8.19: Velocity trajectory of the control point.

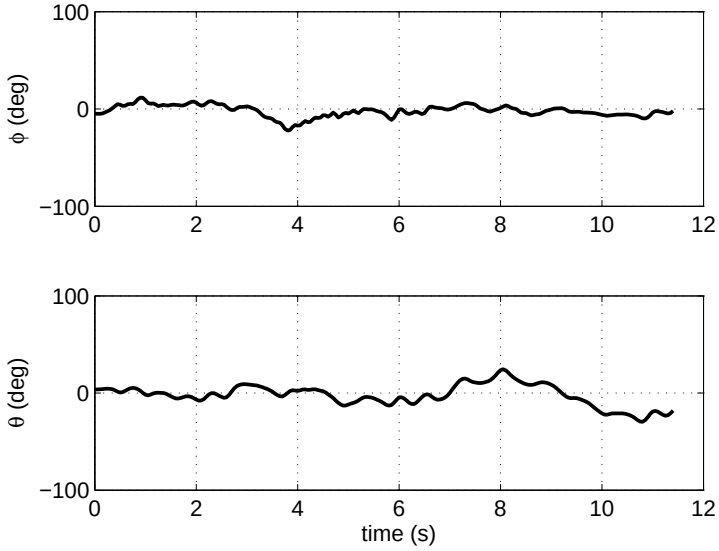

Figure 8.20: Attitude response (roll and pitch angles).

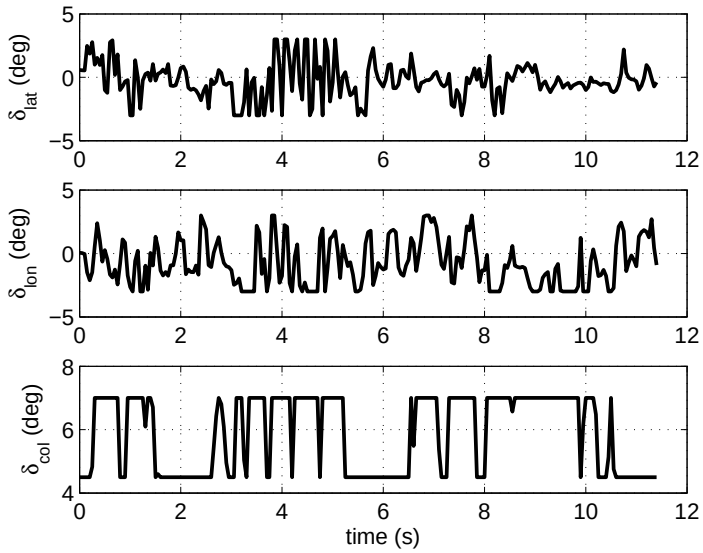

Figure 8.21: Lateral and longitudinal cyclic and collective control inputs.

Chapter 9

Conclusions & Future Work

Model-Based Control design for small-scale unmanned helicopters involves considerable challenges due to their nonlinear and underactuated dynamics with strong cross-couplings between the DOFs and a complex rotor dynamics. A new non-iterative formulation has been derived in this thesis to represent the 6-DOF nonlinear model of the helicopter in a square and control-affine input-output form, which allows for the application of a wide range of nonlinear model-based MIMO control approaches that are unsuitable for the underactuated and non-control affine systems such as the sliding mode control, for small-scale helicopters.

9.1 Conclusions

An experimental platform composed of an Evolution-EX small-scale helicopter airframe, custom avionics, ground station and autopilot software has been described in Chapter 2. A ground station that allows for monitoring the status of the helicopter as well as efficient control gain tuning during flight is also developed. An autopilot software using xPC Target for the real-time implementation of the control algorithm is designed and has a module-based structure to facilitate rapid controller modifications and efficient code debugging.

A new control-oriented model using a square and affine-in-control formula-

tion has been developed in Chapter 3 for the 6-DOF nonlinear dynamics of a small-scale helicopter. The new formulation is non-iterative and derived using a combination of first-principles and system identification. Then, the control point approach is used to obtain a square input-output formulation. Hybrid model and first-principles approach are the two methods used to model the rotational dynamics of the helicopter. The first-principles approach that includes blade element and momentum theories has fewer unknown parameters compared to the hybrid model approach resulting in a simpler parameter identification process. However, validation data from flight tests in Chapter 5 indicate that the hybrid model approach more accurately represent the rotational dynamics of the helicopter than the first-principles approach as the first-principles approach does not account for the effect of the rotor flapping. The influence of the gyroscopic effect of the rotor on the roll and pitch dynamic responses of the helicopter is studied in Chapter 3.

In Chapter 4, the inverse kinematics of the main rotor actuating mechanisms including a 4-point swashplate mechanism and the Bell-Hiller mixer as well as the tail rotor kinematics are derived. The kinematic models of the main and tail rotor are validated in experiments and compared with the linear approximations. The experimental results indicate that the kinematic models obtained from the linear approximations accurately represent the actual kinematics of the system within the operation range of the servos.

A time-domain system identification strategy that combines ground and flight test data has been developed in Chapter 5 to identify the unknown parameters of the nonlinear helicopter model. The lift and drag coefficients of the main and tail rotors are identified using an aerodynamic force measurement testbed custom designed to measure the aerodynamic forces and moments applied to the fuselage of small-scale unmanned helicopters at hover using a combination of eight load

cells. A good match between the predicted model of the main and tail rotor thrust and drag torque, and the experimental data in hover with VAF indices of above 90% is obtained. Flight tests are conducted to identify the unknown parameters of the coupled fuselage-rotor (f-r) dynamic model and empennage drag. These parameters are obtained in a sequential identification process using the nonlinear least squares method. The identified model is cross validated using flight test data with the overall response of the identified nonlinear model of the helicopter matching the real flight data with VAF indices of above 90% for the roll, pitch, yaw and longitudinal and lateral velocity dynamics and a VAF index of above 80% for the heave dynamic. The dynamic responses of the roll and pitch motion are also compared in the frequency-domain and a good match between the model and the flight data in the frequency-domain is achieved.

A robust SMC has been designed in Chapter 6 using the new 6-DOF nonlinear square control-affine model of the helicopter. Simulations are performed to test the controller performance including a three-dimensional complex figure-8 maneuver subject to $\pm$ 20% parameter variations in the mass and moments of inertia, and a forward turn maneuver in the presence of a 4 m/s wind disturbance. The simulation results indicate that the SMC is effective in tracking complex trajectories and is robust to parameter uncertainties (with an error of 0.18 m in the position and 0.08 deg in the yaw angle) and wind disturbances (with an error of 0.17 m in the position and 0.4 deg in the yaw angle).

A HIL testbed design for small unmanned helicopters which provides a safe and low-cost platform to implement control algorithms and tune the control gains in a controlled environment has been developed in Chapter 7. The testbed provides an intermediate step between simulation and real flight test to allow for implementation issues on the real hardware to be tested. It also allows for testing the robustness of the controller to external disturbances in a controlled environment

in the HIL system. A damping system with a negligible parasitic effect on the dynamics of the helicopter around hover is incorporated to minimize the structural stress on the fuselage in case of controller failure or a subsystem malfunction. The HIL system uses the 6-DOF mathematical model of the helicopter, validated in Chapter 5, to determine the actual motion of the helicopter in real-time.

In Chapter 8, the experimental results of the SMC implementation on the Evolution-Ex helicopter using the HIL testbed and real flight tests have been presented. The HIL experiments included hover, forward, sideways and figure-8 trajectories for the longitudinal and lateral control, and step and figure-8 trajectories for the heading control. The experimental results showed that the controller tuned using the HIL testbed achieved a ± 2.5 cm accuracy on the longitudinal and lateral position trajectory tracking, and a ± 5 deg accuracy on the heading trajectory tracking in the presence of external disturbances. Experimental results from the real flight tests are also presented for heading-hold and hover maneuvers. The heading-hold control results in real flight showed that the SMC achieved a ± 9.8 deg accuracy on the yaw control of the helicopter in the presence of wind disturbances. The results from the HIL testbed and real-flight tests indicated that the SMC design based on the square control-affine model of the helicopter dynamics is capable of stabilizing the vehicle in the presence of external disturbances.

The HIL and real flight test results also showed the viability of the entire design procedure including helicopter dynamic model, actuator kinematic model, system identification and SMC design, and the real-time implementation including HIL testbed design, helicopter hardware, avionics, real-time system, communications and ground station.

9.2 Future Work

The square control-affine formulation of the helicopter dynamics is derived for small-scale helicopters with stabilizer bar. Possible future work is to extend this to a helicopter without a stabilizer bar.

Bibliography

[1] R. D. Garcia and K. P. Valavanis. The implementation of an autonomous helicopter testbed. *Journal of Intelligent and Robotic Systems: Theory and Applications*, 54(1):423 – 454, 2009.

[2] A. Coates, P. Abbeel, and A. Y. Ng. Apprenticeship learning for helicopter control. *Communications of the ACM*, 52(7):97 – 105, 2009.

[3] J. E. Corban, A. J. Calise, and J. V. R. Prasad. Implementation of adaptive nonlinear control for flight test on an unmanned helicopter. In *IEEE Conference on Decision and Control*, volume vol.4, pages 3641 – 6, Piscataway, NJ, USA, 1998.

[4] H. J. Kim and D. H. Shim. A flight control system for aerial robots: Algorithms and experiments. *Control Engineering Practice*, 11(12):1389 – 1400, 2003.

[5] E. N. Johnson and S. K. Kannan. Adaptive trajectory control for autonomous helicopters. *Journal of Guidance, Control, and Dynamics*, 28(3):524 – 538, 2005.

[6] L. Marconi and R. Naldi. Robust full degree-of-freedom tracking control of a helicopter. *Automatica*, 43(11):1909 – 1920, 2007.

[7] J. Gadewadikar, F. L. Lewis, K. Subbarao, and B. M. Chen. Structured H_∞ command and control-loop design for unmanned helicopters. *Journal of Guidance, Control, and Dynamics*, 31(4):1093 – 1102, 2008.

[8] S. Saripalli, J. F. Montgomery, and G. S. Sukhatme. Vision-based autonomous landing of an unmanned aerial vehicle. In *IEEE International Conference on Robotics and Automation*, volume 3, pages 2799 – 2804, Washington, DC, United States, 2002.

[9] B. Godbolt, and A. F. Lynch. Model-Based Helicopter UAV Control: Experimental Results. *Journal of Intelligent and Robotic Systems: Theory and Applications*, 73:19 – 31, 2014.

[10] T. J. Koo and S. Sastry. Output tracking control design of a helicopter model based on approximate linearization. *Proceedings of the IEEE Conference on Decision and Control*, 4:3635 – 3640, 1998.

[11] R. Mahony, T. Hamel, and A. Dzul. Hover control via Lyapunov control for an autonomous model helicopter. In *IEEE Conference on Decision & Control*, volume 4, pages 3490 – 3495, Phoenix, AZ, USA, 1999.

[12] I. A. Raptis, K. P. Valavanis, and W. A. Moreno. System identification and discrete nonlinear control of miniature helicopters using backstepping. *Journal of Intelligent and Robotic Systems: Theory and Applications*, 55(2-3):223 – 243, 2009.

[13] B. Godbolt. *Experimental nonlinear control of a helicopter unmanned aerial vehicle (UAV).* PhD thesis, University of Alberta, Edmonton, 2013.

[14] M. La Civita, G. Papageorgiou, W. C. Messner, and T. Kanade. Integrated modeling and robust control for full-envelope flight of robotic helicopters. In *IEEE ICRA*, volume vol.1, pages 552 – 7, Piscataway, NJ, USA, 2003.

[15] M. La Civita, G. Papageorgiou, W. C. Messner, and T. Kanade. Design and flight testing of an H_∞ controller for a robotic helicopter. *Journal of Guidance, Control, and Dynamics*, 29(2):485 – 494, 2006.

[16] H. J. Kim, D. H. Shim, and S. Sastry. Nonlinear model predictive tracking control for rotorcraft-based unmanned aerial vehicles. In *American Control Conference*, volume 5, pages 3576 – 3581, Anchorage, AK, United States, 2002.

[17] A. Bogdanov and E. Wan. State-dependent Riccati equation control for small autonomous helicopters. *Journal of Guidance, Control, and Dynamics*, 30(1):47 – 60, 2007.

[18] J. J. E. Slotine and L. Weiping. *Applied Nonlinear Control*. Prentice-Hall, Inc., Englewood Cliffs, NJ, 1991.

[19] H. Ifassiouen, M. Guisser, and H. Medromi. Robust nonlinear control of a miniature autonomous helicopter using sliding mode control structure. *World Academy of Scinece, Engineering and Technology*, 1(2):100 – 106, 2007.

[20] J. K. Pieper. Application of SLMC: TRC control of a helicopter in hover. In *ACC1995*, volume 2, pages 1191 – 1195, Seattle, WA, USA, 1995.

[21] W. Wang, K. Nonami, and Y. Ohira. Model reference sliding mode control of small helicopter X.R.B based on vision. *International Journal of Advanced Robotic Systems*, 5(3):235 – 242, 2008.

[22] J. Fu, W. Chen, and Q. Wu. Chattering-free sliding mode control with unidirectional auxiliary surfaces for miniature helicopters. *International Journal of Intelligent Computing and Cybernetics*, 5(3):421 – 438, 2012.

[23] T. Floquet, S. K. Spurgeon, and C. Edwards. An output feedback sliding mode control strategy for MIMO systems of arbitrary relative degree. *International Journal of Robust and Nonlinear Control*, 21(2):119 – 133, 2011.

[24] D. J. McGeoch, E. W. McGookin, and S. S. Houston. MIMO sliding mode attitude command flight control system for a helicopter. In *AIAA2005*, volume 6, pages 4718 – 4732, San Francisco, CA, United States, 2005.

[25] F. Fahimi. Full formation control for autonomous helicopter groups. *Robotica*, 26(2):143 – 156, 2008.

[26] Y. Xu. Multi-timescale nonlinear robust control for a miniature helicopter. *IEEE Transactions on Aerospace and Electronic Systems*, 46(2):656 – 671, 2010.

[27] J. Downs, R. Prentice, S. Dalzell, A. Besachio, C. M. Ivler, Mark B. Tischler, and Mohammadreza Hossein Mansur. Control system development and flight test experience with the MQ-8b fire scout vertical take-off unmanned aerial vehicle (VTUAV). In *AHS Annual Forum*, volume 3, pages 1933 – 1959, Virginia Beach, VA, United States, 2007.

[28] Ioannis. A. Raptis and K. P. Valavanis. *Linear and Nonlinear Control of Small-Scale Unmanned Helicopters*. Springer, NY, 2011.

[29] S. P. Khaligh, F. Fahimi, and M. Saffarian. Comprehensive aerodynamic modeling of a small autonomous helicopter rotor at all flight regimes. In *AIAA Modeling and Simulation Technologies Conference*, pages 1 – 10, Chicago, Illinois, United States, 2009.

[30] S. P. Khaligh, A. Martinez, F. Fahimi, and C. R. Koch. A HIL testbed for small unmanned helicopter's initial controller gain tuning. In *Interna-*

tional Conference on Unmanned Aircraft Systems (ICUAS), pages 383 – 391, Atlanta, GA, May 2013.

[31] S. P. Khaligh, F. Fahimi, and C. R. Koch. Control oriented modeling for nonlinear trajectory tracking control of small unmanned helicopters. *submitted to the Journal of the American Helicopter Society*, 2014.

[32] S. P. Khaligh, F. Fahimi, and C. R. Koch. A fast inverse kinematic solution for the actuating mechanism of a small-scale unmanned helicopter. *submitted to the Multibody System Dynamics*, 2014.

[33] S. P. Khaligh, F. Fahimi, and C. R. Koch. A system identification strategy for nonlinear model of small unmanned helicopters. *submitted to the Journal of the American Helicopter Society*, 2014.

[34] S. P. Khaligh, A. Martinez, F. Fahimi, and C. R. Koch. A HIL testbed for initial controller gain tuning of a small unmanned helicopter. *Journal of Intelligent and Robotic Systems*, pages 1 – 20, 2014.

[35] A. Martinez. *System identification, model validation and LQR/LQG control of a small-scale helicopter*. MSc thesis, University of Alberta, Edmonton, to appear 2014.

[36] P. F. Lorber, R. C. Stauter, R. J. Haas, T. J. Anderson, M. S. Torok, and F. W. Kohlhepp. Techniques for comprehensive measurement of model helicopter rotor aerodynamics. In *AHS 50th Annual Forum*, pages 797 – 814, Washington, DC, May 1994.

[37] D. L. Kunz and D. H. Hodges. Analytical modeling of helicopter static and dynamic induced velocity in GRASP. *Mathematical and Computer Modelling*, 11:286 – 292, 1988.

[38] G. D. Padfield. *Helicopter Flight Dynamics*. Blackwell Publishing Ltd, Enfant Promenade, DC, 2007.

[39] A. R. S. Bramwell, G. Done, and D. Balmford. *Bramwell's helicopter dynamics*. American Institute of Aeronautics and Astronautics Butterworth-Heinemann, Reston, VA, 2001.

[40] M. La Civita. *Integrated modeling and robust control for full-envelope flight of robotic helicopters*. PhD thesis, Carnegie Mellon University, Ann Arbor, 2003.

[41] B. Mettler, M. B. Tischler, and T. Kanade. System identification modeling of a small-scale unmanned rotorcraft for flight control design. *Journal of the American Helicopter Society*, 47(1):50 – 63, 2002.

[42] O. Rand. A phenomenological modification for glauert's classical induced velocity equation. *Journal of the American Helicopter Society*, 51(3):279 – 282, 2006.

[43] F. Fahimi and M. Saffarian. The control point concept for nonlinear trajectory-tracking control of autonomous helicopters with fly-bar. *International Journal of Control*, 84(2):242 – 253, 2011.

[44] C. H. Lin and S. S. Jan. Autonomous hovering proportional-integral sliding mode controller design and its flight test validation for a small-scaled unmanned helicopter. *Journal of Aerospace Engineering*, 26(4):750 – 767, 2013.

[45] J. Pujol. The solution of nonlinear inverse problems and the Levenberg-Marquardt method. *Geophysics*, (4):1–16, 2007.

[46] S. K. Kim and D. M. Tilbury. Mathematical modeling and experimental identification of an unmanned helicopter robot with flybar dynamics. *Journal of Robotic Systems*, 21(3):95 – 116, 2004.

[47] H. Kim, H. R. Dharmayanda, T. Kang, A. Budiyono, G. Lee, and W. Adiprawita. Parameter identification and design of a robust attitude controller using H_∞ methodology for the raptor E620 small-scale helicopter. *International Journal of Control, Automation, and Systems*, 10(1):88 – 101, 2012.

[48] A. B. Budiyono, K. J. Yoon, and F. D. Daniel. Integrated identification modeling of rotorcraft-based unmanned aerial vehicle. In *17th Mediterranean Conference on Control and Automation*, pages 898 – 903, Makedonia, Thessaloniki, Greece, June 2009.

[49] T. Clarke. Time domain identification of helicopters - a new perspective. In *RTO SCI Symposium on System Identification for Integrated Aircraft Development and Flight Testing*, pages 898 – 903, Madrid, Spain, May 1998.

[50] G. Cai, B. M. Chen, T. H. Lee, and K. Lum. Comprehensive nonlinear modeling of a miniature unmanned helicopter. *Journal of the American Helicopter Society*, 57(1):1–13, 2012.

[51] M. Saffarian and F. Fahimi. A comprehensive kinematic analysis of a model helicopter's actuating mechanism. In *AIAA2008*, pages 1 – 15, Reno, NV, United States, 2008.

[52] M. R. Sabaapour and H. Zohoor. Analysis of a swashplate mechanism of the hingeless rotor hub with the flybar in a model helicopter, part i: Kinematics. *Journal of System Design and Dynamics*, 4(4):616–631, 2010.

[53] C. W. Wampler. Solving the kinematics of planar mechanisms. *Journal of Mechanical Design, Transactions of the ASME*, 121(3):387 – 391, 1999.

[54] R. Horn. *Matrix Analysis*. Cambridge University Press, Cambridge Cambridgeshire, NY, 1985. Section 2.3.

[55] T. F. Coleman and Y. Li. An interior trust region approach for nonlinear minimization subject to bounds. *SIAM Journal on Optimization*, 6(2):418 – 45, May 1996.

[56] V. Verdult, M. Lovera, and M. Verhaegen. Identification of linear parameter-varying state-space models with application to helicopter rotor dynamics. *International Journal of Control*, 77(13):1149 – 1159, 2004.

[57] L. Merino, F. Caballero, J. R. M. Dios, I. Maza, and A. Ollero. An unmanned aircraft system for automatic forest fire monitoring and measurement. *J Intell Robot Syst*, 65:533–548, 2012.

[58] D.W. Casbeer, R.W. Beard, T.W. McLain, Sai-Ming Li, and R.K. Mehra. Forest fire monitoring with multiple small UAVs. In *ACC*, pages 3530 – 3535 vol. 5, June 2005.

[59] Z. Li, Y. Liu, R. A. Walker, R. F. Hayward, and J. Zhang. Towards automatic power line detection for a UAV surveillance system using pulse coupled neural filter and an improved hough transform. *Machine Vision and Applications*, 21(5):677–686, September 2009.

[60] C. A. Marinho, C. de Souza, T. Motomura, and A. G. da Silva. In-service flare inspection by unmanned aerial vehicles (UAVs). In *18th World Conference on Nondestructive Testing*, Durban, South Africa, April 2012.

[61] R. Haarbrink and H. Eisenbeiss. Accurate DSM production from unmanned helicopter systems. *Int. Arch. Photogramm. Remote Sens. Spat. Inf. Sci*, 37:1259–1264, 2008.

[62] J. Gundlach. *Designing Unmanned Aircaft Systems: A comprehensive Approach*. American Institute of Aeronautics and Astronautics, Inc, 1801 Alexander Bell Drive, Reston, Virginia 20191-4344, USA, first edition, 2012.

[63] Y. M. Zhang, A. Chamseddine, C. A. Rabbath, B. W. Gordon, C. Y. Su, S. Rakheja, C. Fulford, J. Apkarian, and P. Gosselin. Development of advanced FDD and FTC, techniques with application to an unmanned quadrotor helicopter testbed. *J. Franklin Inst.*, 2013.

[64] W. E. Green and P. Y. Oh. Autonomous hovering of a fixed-wing micro air vehicle. In *ICRA*, pages 2164 –2169, May 2006.

[65] H. Oh, D. Won, S. Huh, D. Shim, M. Tahk, and A. Tsourdos. Indoor UAV control using multi-camera visual feedback. *J Intell Robot Syst*, 61:57–84, 2011.

[66] L. R. G. Carrillo, E. R., A. Sanchez, A. Dzul, and R. Lozano. Stabilization and trajectory tracking of a quad-rotor using vision. *J Intell Robot Syst*, 61:103–118, 2011.

[67] I. M. Bataller, J. Pestana, M. O. Mendez, P. Campoy, and L. Mejias. MAVwork: A framework for unified interfacing between micro aerial vehicles and visual controllers. In *Frontiers of Intelligent Autonomous Systems*, volume 466 of *Studies in Computational Intelligence*, pages 165–179. Springer Berlin Heidelberg, 2013.

[68] A. Chamseddine, Y. Zhang, C. A. Rabbath, C. Join, and D. Theilliol. Flatness-based trajectory planning/replanning for a quadrotor unmanned

aerial vehicle. *IEEE Transactions on Aerospace and Electronic Systems*, 48(4):2832 –2848, October 2012.

[69] H. Chao, Y. Cao, and Y. Chen. Autopilots for small unmanned aerial vehicles: A survey. *International Journal of Control, Automation and Systems*, 8:36–44, 2010.

[70] C. Guowei, W. Biao, B. M. Chen, and T. H. Lee. Design and implementation of a flight control system for an unmanned rotorcraft using RPT control approach. In *30th Chinese Control Conference (CCC)*, pages 6492 –6497, July 2011.

[71] C. L. Castillo, W. Moreno, and K. P. Valavanis. Unmanned helicopter waypoint trajectory tracking using model predictive control. In *Mediterranean Conference on Control Automation*, pages 1 –8, June 2007.

[72] R. D. Garcia and K. P. Valavanis. The implementation of an autonomous helicopter testbed. *J Intell Robotics Syst*, 54(1):423–454, Mar. 2009.

[73] H. J. Kim and D. H. Shim. A flight control system for aerial robots: algorithms and experiments. *Control Engineering Practice*, 11(12):1389 – 1400, 2003.

[74] A. T. Kutay, A. J. Calise, M. Idan, and N. Hovakimyan. Experimental results on adaptive output feedback control using a laboratory model helicopter. *IEEE Control Systems Technology*, 13(2):196–202, March 2005.

[75] B. Andrievsky, D. Peaucelle, and A. L. Fradkov. Adaptive control of 3-DOF motion for LAAS helicopters benchmark: Design and experiments. In *ACC*, pages 3312–3317, July 2007.

[76] J. F. Montgomery, A. E. Johnson, S. I. Romeliotis, and L. H. Matthies. The jet propulsion laboratory autonomous helicopter testbed: A platform for planetary exploration technology research and development. *Journal of Field Robotics*, 23(3):245–267, 2006.

[77] N. I. Vitzilaios and N. C. Tsourveloudis. An experimental test bed for small unmanned helicopters. *J Intell Robot Syst*, 54:769–794, 2009.

[78] M. F. Weilenmann and H. P. Geering. Test bench for rotorcraft hover control. *Journal of Guidance, Control and Dynamics*, 17(4):729 – 736, 1994.

[79] V. Narli and P. y. Oh. A Hardware-In-The-Loop test rig for designing Near-Earth aerial robotics. In *Proceedings of the 2006 IEEE International Conference on Robotics and Automation*, Orlando, Florida, United States, 2006.

[80] A. Tewari. *Modern Control Design with MATLAB and Simulink*. John Wiley, 2002.

[81] B. Mettler, V. Gavrilets, E. Feron, and T. Kanade. Dynamic compensation for high-bandwidth control of small-scale helicopter. In *American Helicopter Society Specialist Meeting*, pages 1 – 8, Alexandria, VA, 2002.

Appendix A

Kalman Observer Design to Eliminate GPS Latency

As mentioned in Chapter 2, GPS data is often processed at a lower rate than the other IMU data causing the position determination to be delayed. This phenomenon is called GPS latency as shown in Figure A.1.

The sampling frequency chosen for the controller to stabilize the helicopter is 40 Hz. The GPS refresh rate is 4Hz which is ten times slower than the sampling frequency of the system. In other words, the GPS latency in this system is 0.225 s.

The GPS latency generates discontinuity in the position data as it holds the current position for the next ten sampling intervals as shown in Figure A.1. During this time, the controller is unaware of any changes in the position of the helicopter's CG. This can make the closed loop system unstable, therefore must be avoided.

The IMU used in this work provides acceleration data in the body coordinates as well as the position data from the GPS. By knowing the initial position and velocity, the position can be simply calculated by two times integrating from the acceleration. However, noise and inaccuracies in the acceleration measurements result in an integration drift causing the position error to drastically grow in time.

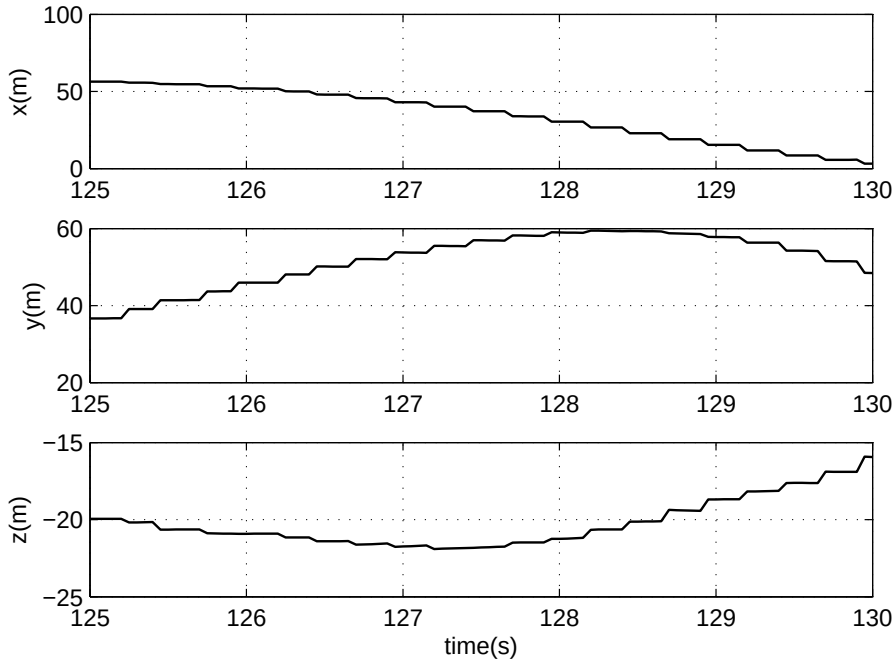

Figure A.1: GPS latency from the flight data.

To eliminate the integration drift and the GPS latency, a 9^{th}-order Kalman filter observer is designed. Kalman filter is an optimal observer that minimizes the covariance of the estimation error. The Kalman filter designed for this purpose receives both the GPS and acceleration data from the IMU and calculates the estimated position, velocity and acceleration at each sampling time.

Defining the state and input vectors as $\mathbf{x}_k = [x\ y\ z\ u\ v\ w\ a_x\ a_y\ a_z]^T$, and $\mathbf{u}_k = [x\ y\ z\ a_x\ a_y\ a_z]^T$, respectively, the Kalman filter can be represented as:

$$\begin{aligned} \dot{\mathbf{x}}_k &= \mathbf{A}\mathbf{x}_k + \mathbf{B}\mathbf{u}_k + \mathbf{F}\mathbf{v}_k \\ \mathbf{y}_k &= \mathbf{C}\mathbf{x}_k + \mathbf{D}\mathbf{u}_k + \mathbf{z}_k \end{aligned} \tag{A.1}$$

where $\mathbf{v}_k$ is the process noise vector and may arise due to the modeling errors such as neglecting nonlinear or high-frequency dynamics and $\mathbf{z}_k$ is the measurement noise vector, which are both assumed to be white noises with the power spectral

density matrices, V and Z, chosen as:

$$V = 2e^8 \begin{bmatrix} 1_{3\times3} & 0_{3\times3} \\ 0_{3\times3} & 5 \times 1_{3\times3} \end{bmatrix}, \quad Z = 250 \times 1_{3\times3} \tag{A.2}$$

Kalman filter minimizes the covariance of the estimation error $\mathbf{e}_k = \mathbf{x}_k - \mathbf{x}_0$, where $\mathbf{x}_0$ is the predicted state vector. The state equation of the Kalman filter can be written as:

$$\begin{aligned} \dot{\mathbf{x}}_0 &= \mathbf{A}\mathbf{x}_0 + \mathbf{B}\mathbf{u}_k + \mathbf{L}\Big(\mathbf{y}_k - \mathbf{C}\mathbf{x}_0 - \mathbf{D}\mathbf{u}_k\Big) \\ \mathbf{y}_k &= \mathbf{C}\mathbf{x}_0 \end{aligned} \tag{A.3}$$

where $\mathbf{L}$ is the optimal gain matrix of the Kalman filter, which can be found by solving the algebraic Riccati equation [80]. This equation can be easily solved in MATLAB$^{\text{TM}}$as:

$$\mathbf{L} = lqe(\mathbf{A}, \mathbf{F}, \mathbf{C}, \mathbf{V}, \mathbf{Z})$$

Once the optimal gain matrix $\mathbf{L}$ is calculated offline it can be used in Eq. (A.3) to predict the state vector $\mathbf{x}_0$ in real-time. The measured position data from GPS for a 200 s experiment is compared with the Kalman observer outputs as shown in Figure A.2, indicating that the Kalman observer accurately predicts the position of the vehicle. Also, the results are zoomed in Figure A.3 for the period of 125-130 s for a better clarity, which shows that the GPS latency is eliminated in the predicted positions by the Kalman observer and the observer results in a continuous and smooth prediction of the position data.

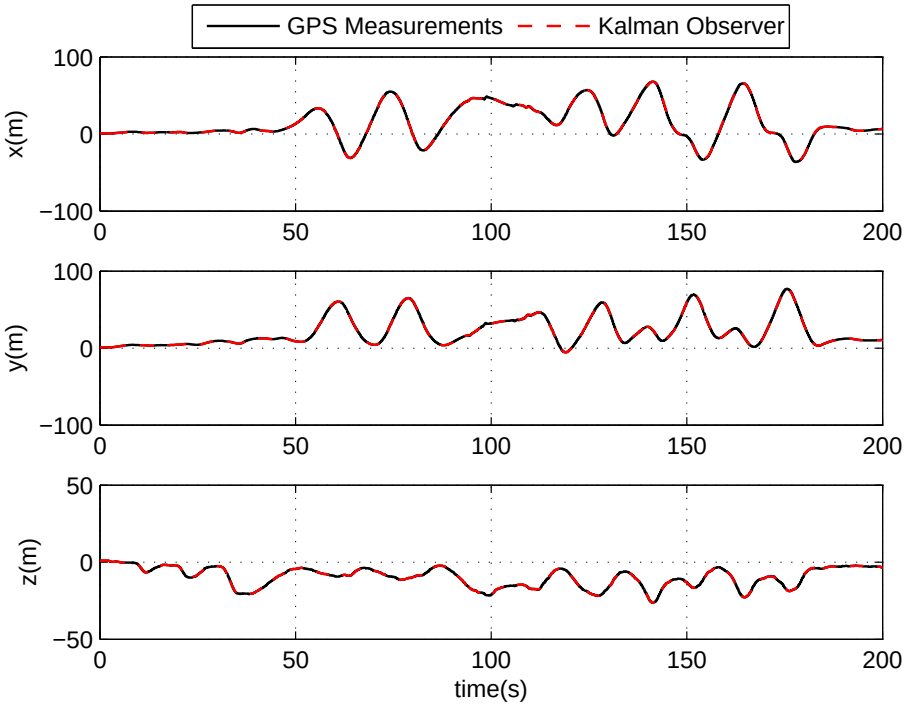

Figure A.2: Measured and predicted position data from GPS.

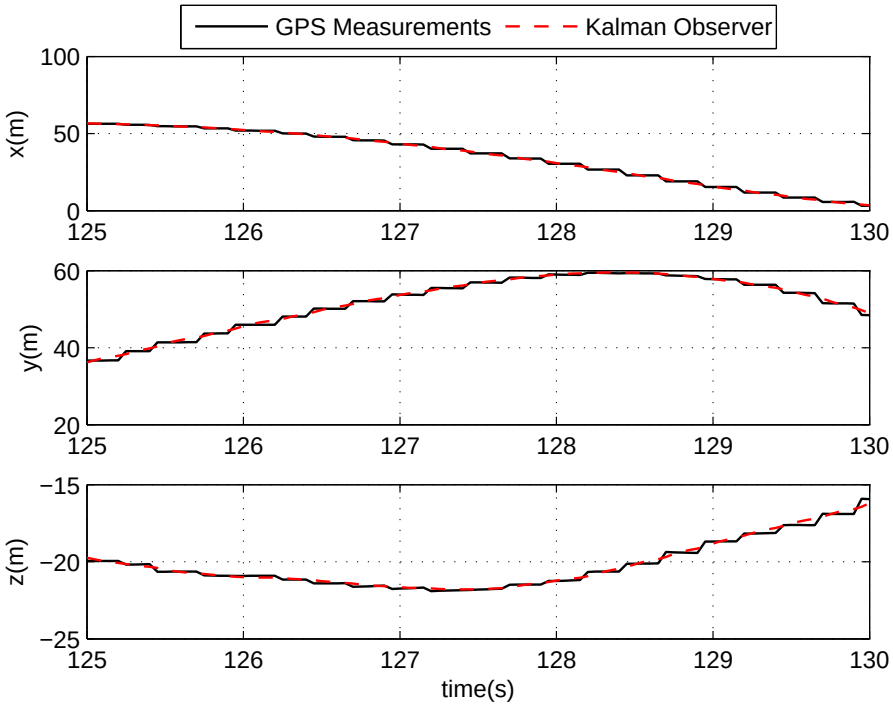

Figure A.3: Zoomed measured and predicted position data from 125 to 130 s.